Wayne State University Dissertations

1-1-2010

Quantification Of Vascular Parametric Indices Using Dynamic Contrast-Enhanced Magnetic Resonance Imaging

Areen Khaled Al.bashir
Wayne State University

Follow this and additional works at: http://digitalcommons.wayne.edu/oa_dissertations

Part of the Biomedical Engineering and Bioengineering Commons

Recommended Citation

QUANTIFICATION OF VASCULAR PARAMETRIC INDICES USING DYNAMIC CONTRAST-ENHANCED MAGNETIC RESONANCE IMAGING

by

AREEN K. AL-BASHIR

DISSERTATION

Submitted to the Graduate School

of Wayne State University,

Detroit, Michigan

in partial fulfillment of the requirements

for the degree of

DOCTOR OF PHILOSOPHY

2010

MAJOR: BIOMEDICAL ENGINEERING

Approved by:

_____
Advisor   Date

_____

_____

_____

DEDICATION

I dedicate this work to my parents

ACKNOWLEDGMENTS

I owe my gratitude to God for giving me the strength to be able to explore and search for knowledge as well as for blessing me with such great people who have directly or indirectly helped me throughout my graduate study and are responsible for my reaching this point.

I extend my sincerest gratitude to Dr. E Mark Haacke for his support and kindness as well as his belief in my abilities and work. He has been a constant source of thoughtful guidance in pursuing this project. Because of his input, advice and challenge, I have matured as a researcher and as a scholar.

I would like to thank Dr. Gilda Hillman and her lab for allowing me to work with them on this joint project and for her input on my manuscripts. I would also like to thank the following co-workers and friends Tilak Gattu, who first introduced me to DCE-MRI; Meng Li for developing the software I used in my research; Zahid Latif and Yashwanth Katkur for being so kind in teaching me how to run the MR scanner; Lisa Brownschidle and Rachel Martis-Laze for taking care of issues related to my study at Wayne State University; Emil Pacurar and Charbel Habib for giving me a hard time during many hours in the data room. There are many others in the lab whom I would like to thank for accommodating me and my eccentricities and who made the workplace pleasant for me. Honestly, I am working with a great group at the MRRF and MRI Institute, and I will always remember them. I would like also to thank the Wayne State Writing Center and Sara Tipton for reading my written material. Finally, I would like to thank my dissertation advisory committee members; Dr. Tao Li, Dr. John Cavanaugh and Dr. Weiping Ren for their comments and time in helping me complete my PhD.

In the end I would like to thank my family and friends, and most of all my parents and my friend Dalal; they have definitely encouraged me the longest! They will always be dear to my heart. Without their help and support, I may have not been able to tread this path so smoothly; to them my gratitude is boundless.

PREFACE

Dynamic contrast enhanced magnetic resonance imaging (DCE-MRI) has been routinely used to evaluate and quantify the effectiveness of new drugs on tumor vascular characteristics using gadolinium-DTPA as a contrast agent in MRI scans. It is a non-invasive tumor diagnostic method, with which the perfusion in tissue can be visualized and can also provide important functional information about tissue microvasculature. The most important requirement for DCE-MRI is the need to compare results from different institutions. This work will provide us with more reproducible DCE results by introducing a fixed T1(0) approach and by introducing new DCE parameters to quantify cancer treatment efficacy. This work also enhanced the ability of DCE-MRI as a non-invasive tool to decide the best treatment dose among a number of different doses of the antiangiogenic drug, sunitinb.

v

TABLE OF CONTENTS:

viii

LIST OF TABLES

Chapter Three

Chapter Five

Chapter Six

LIST OF FIGURES

Chapter Two

Chapter Three

Chapter Four

ABBREVIATION LIST

AUC - Area under the curve

AUCtp - Area under the curve to the peak

CIAUC - Cumulative IAUC

CT -Computed Tomography

DCE-MRI - Dynamic contrast-enhanced magnetic resonance imaging

FA - Flip Angle

FAP - Fraction of active pixels

FOV - Field of View

FWHM- Full width at half maximum

Gd-DTPA -Gadopentate Dimeglumine Penta Acetic Acid

Gem: Gemcitabine

HBSS - Hanks' balanced salt solution

H&E - Hematoxylin-eosin

IAUC - Initial area under the curve

IFNα - Interferon alfa

i.p.: Intraperitoneal

KCI-18 RCC - Karmanos Cancer Institute-18 Renal Cell Carcinoma cell line

KCI-18/IK - KCI-18 RCC cell line passaged in mouse kidney

KT - Kidney tumors

NK - Normal kidney

Nslope - Rate of Gd clearance

ORR - Objective response rate

PBS: phosphate-buffered saline

PDGFR-β - Platelet derived growth factor receptor- beta

PEAK - Peak concentration

PFS - Progression free survival

Pslope - Rate of uptake

RBC - Red blood cells

RCC - Renal cell carcinoma

rf - Radio Frequency

ROI - Region of interest

RTK - Receptor tyrosine kinases

SD – Standard Deviation

SNR -Signal to Noise Ratio

SU10 - Sunitinib 10mg/kg/day

SU20 - Sunitinib 20mg/kg/day

SU40 - Sunitinib 40mg/kg/day

TE -Echo Time

TR -Repeat Time

TTP - Time to peak

VEGF - Vascular endothelial growth factor

VEGFR-2 - Vascular endothelial growth factor receptor -2

VOI -Volume of Interest

Chapter One

Introduction

1.1 Background and Project Motivation

Magnetic resonance imaging (MRI) was introduced to the medical field in the late 1970s, and it is one of the most accurate, non-invasive and safe imaging modalities. It has been proven to be one of the most promising methods to image human anatomy, and it functions with reasonable resolution, which can reach the sub-millimeter level and give adequate structured, detailed images (Haacke et al., 1999). MRI uses the magnetic properties of hydrogen protons in tissues. The MRI signal depends on the density of hydrogen protons and their magnetic moment interactions with the external magnetic field and the radio-frequency excitation (Bradley; Faulkner, 1996). MRI has a number of advantages, such as high resolution 3D capability and therefore the flexibility to produce different cross-sectional images in any plane (Hedley and Yan, 1992). The most obvious and important advantages of MRI compared to other imaging modalities is the absence of ionization radiation. This will spare the patients any additional risk caused by such exposure and eventually allow regular and more frequent monitoring of lesions inside the human brain, for example, compared to computed tomography (CT) or positron emission tomography (PET) (Peters, 2000; Weiss et al., 2008). Clinical MRI has minimal risks for imaging normal organs and tissues in human. Thus, MRI has proven to be a secure method to explore the human body with highly detailed images.

MRI is a powerful means to non-invasively measure the vasculature and hemodynamic parameters in tissues, using intrinsic endogenous or exogenous contrast agents. Many MRI sequences have been developed to enhance image contrast, such as T1-weighted and T2-weighted imaging, and/or to quantify tissue hemodynamic properties if the scan is repeated with

time, such as diffusion and perfusion imaging. Perfusion imaging can be performed using two different techniques: Dynamic Contrast Enhanced (DCE) MRI and Dynamic Susceptibility Contrast (DSC) or so-called Perfusion Weighted Imaging (PWI). Both techniques (i.e., DCE and DSC) use a bolus of contrast agent, gadolinium diethylenetriamine penta-acetic acid (Gd-DTPA, Magnevist, Berlex Laboratories, Wayne, NJ), that travels through the major vessels, then passes through the capillaries and produces a transient signal enhancement (DCE) or signal loss due to susceptibility effects (DSC) (Cha, 2004; Ludemann et al., 2009).

DCE-MRI has been used in many studies as a valuable tool to evaluate and quantify the effectiveness of new drugs on the vasculature of tumors. It is a non-invasive tumor diagnostic method, where the perfusion in tissue can be visualized by the flow of contrast agent and provide important functional information about the tissue microvasculature, including tissue permeability and blood volume (Galbraith et al., 2002). Increasing evidence suggests that microcirculatory parameters derived from DCE-MRI can potentially be useful for tumor characterization and for monitoring cancer therapy outcomes. However, no study discusses the use of DCE-MRI for monitoring vascular changes induced by treatment in different sites of the organ or the tumor.

In general, three main methods to analyze data are used in DCE-MRI: histogram analysis, extracting K^{trans}, K_{ep} and v_e and parametric maps (Tofts and Kermode, 1991; Guo and Reddick, 2009). However, this quantification is difficult. DCE has many parameters that make it a very complex technique, such as measuring the contrast agent concentration in the plasma or the so-called Arterial Input Function (AIF) and choosing the pharmacokinetic model (Galbraith et al., 2002; Cutajar et al., 2009). Therefore, in this proposal, we will present new approaches to overcome these limitations in DCE-MRI and enhance the quantification of tissue hemodynamic parameters.

The second chapter will briefly discuss cell cycle and tumor biology in order to understand the hemodynamic differences between normal and tumor tissue. The third chapter will explain the theory behind DCE-MRI, experiment requirements, DCE-MRI limitations and sources of error. The fourth chapter is our published manuscript that uses DCE-MRI to select the best treatment dose of the antiangiogenic drug sunitinib that affects the KCI-18 kidney tumors with less impact on other healthy tissues (Neoplasia, 11, 910-920, 2009). Chapter five will include our accepted manuscript that report the use of DCE-MRI to monitor the vascular changes induced by pre-treatment with sunitinib to schedule the initiation of chemotherapy (Translational Oncology Journal, in press 2010)

Chapter six will include our paper which we will submit to the Journal of Magnetic Resonance Imaging. In this chapter we introduce new hemodynamic parameters that serve as a measure to help study the treatment effect throughout the kidneys. And finally, chapter seven will include our conclusion and future directions.

1.2 Project Aims:

The ability to assess blood perfusion and other tissue hemodynamic changes in tumors is critical for the diagnosis and selection of proper treatment procedures. DCE-MRI has been routinely used for tumor diagnosis by adding functional vascular information in addition to anatomical detailed images. DCE-MRI is now a well-established diagnostic tool; however it has some limitations. Numerous studies are investigating ways to enhance the ability of DCE-MRI and to eliminate the sources of error. Therefore, in this project, we aim to first elucidate the ability of DCE-MRI as a tool to select a dose of antiangiogenic drug to regularize the vasculature of the tumor, and second, to develop new DCE parameters to clearly quantify the micro-vascular

behavior of tumors and normal tissue in order to assess the treatment effect on tumors as well as normal tissue.

After discussing DCE theory in the first two sections of chapter three, Section 3.3 introduces a new algorithm to quantify vascular changes using a fixed T1(0) instead of calculating the original T1(0) for a region of interest. We hypothesized that using a fixed value for T1(0) would eliminate most of the effects of the noise from the calculations of T1(t). Further, it would increase the accuracy of the DCE-MRI method and would make it possible to utilize data even when the multiple flip angle (FA) data used to find T1(0) was faulty.

Chapter four describes the use of DCE-MRI not only to study the effect of the antiangiogenic drug, sunitinib, on the tumor and normal tissue but also as a tool to determine the dose which causes regularization of the tumor vasculature with minimal impact on normal healthy tissues. Chapter five uses DCE-MRI to monitor the vascular changes induced by pre-treatment with sunitinib in KCI-18 kidney tumors to schedule the initiation of chemotherapy.

In chapter six, we discuss a number of new DCE parameters that we developed as well as our hypothesis that DCE-MRI parametric maps have the potential to evaluate tissue physiology. The treatment effect on both normal and tumor tissues can be described by these parametric maps. We also introduced a new definition for full width at the half maximum (FWHM) from the initial area under the curve (IAUC) histogram that has the potential to describe further the effect of different treatment doses on tumor and normal tissues. We also hypothesized that the blood volume fraction (λ) can be derived from the ratio of the concentration of the contrast agent in the tissue to the concentration of the contrast agent of the blood vessel. This work will provide clinicians with a new tool to enhance the ability to make clinical decisions regarding tumor treatment.

Chapter Two

Introduction to Kidney Anatomy and Tumor Biology

2.1 Kidney Anatomy and Physiology:

Kidneys are located in the abdominal cavity, one on each side of the spine. The main function of the kidney is to maintain homeostasis or equilibrium between internal volume and electrolyte status and that of the environment's influences, diet and intake. It functions to maintain our intra and extracellular fluid status at a constant despite the wide variety of daily fluid and electrolyte intake.

The kidney has a bean-shaped structure. Figure 2.1 shows the kidney's main region. Kidneys are surrounded by tough fibrous tissue called the renal capsule. The outer, reddish region, next to the capsule, is the renal cortex, which surrounds a region called the renal medulla. The renal medulla consists of a series of renal pyramids, which contain straight tubular structures and blood vessels. The cortex and medulla make up the parenchyma of the kidney. The calyx collects urine from each pyramid. The urine flows in to the renal pelvis which located at the center of the kidney.

Figure 2.1: Kidney's main region: the renal cortex, the renal medulla, the calyx and the renal pelvis. The cortex and medulla make up the parenchyma of the kidney. Once the urine is formed, it is collected through the calyx and flows to the renal pelvis which located at the center of the kidney.
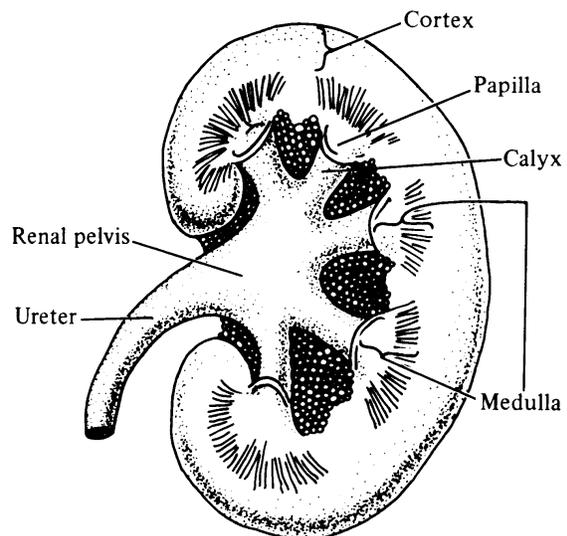
The basic structural and functional unit of the kidney is the nephron which is located between the kidney's parenchyma (Figure 2.2). Nephrons are responsible for blood filtration and waste extraction. Each nephron has a region called glomerulus which is a capillary tuft and where the first filtration step occurs. The glomerulus is surrounded by the Bowman capsule and both, the glomerulus and Bowman's capsule, are located in the cortex of the kidney (Figure 2.2).

Each Bowman's capsule is a tiny filter. Blood containing waste substances, proteins, sugars, etc., is forced to the kidneys by the pumping action of the heart. Under pressure, a solution is driven out of the capillaries of the glomerulus through the walls of the capsule into its hollow interior (Figure 2.2). The solution in the capsule is blood plasma minus the large molecules. These molecules are big to pass through the capillary wall. From the capsule the fluid passes along the tubule to the calyx till it reaches the renal pelvis.
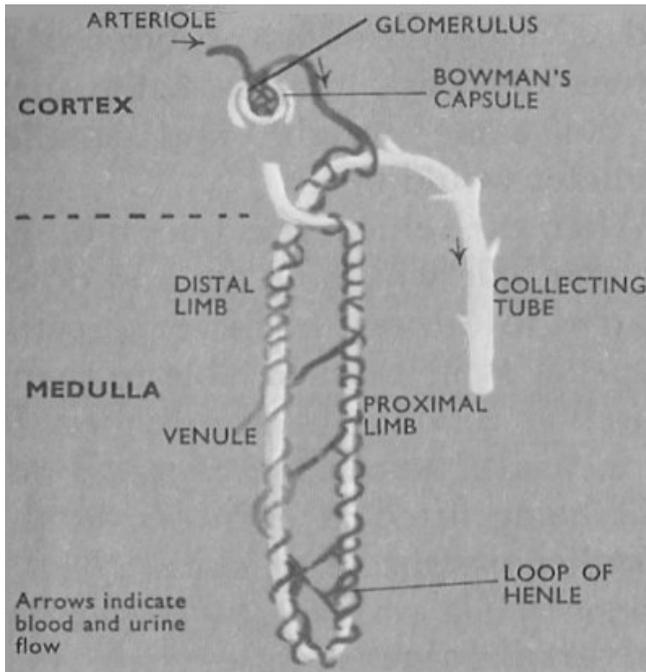
Figure 2.2: The nephron is located in the kidney's parenchyma. Each nephron is composed of an initial filtering component (the renal corpuscle) and a tubule specialized for reabsorption and secretion.

Renal Blood Flow (RBF)

Kidneys receive the highest blood flow per gram of organ weight in the body via the renal artery. Renal blood flow (RBF) is the fraction of the total cardiac output that flows through the kidneys. The kidney is constantly fed by roughly 20% of the cardiac output or a renal fraction of 0.2. Thus, a very substantial portion of the total cardiac output flows through the kidneys. During various stress conditions or disease, the renal fraction can vary considerably and be markedly affected.

2.2 Cell Cycle and Tumor Biology

The term proliferative cell cycle includes a series of steps that occur and lead to cell division and duplication. The cell cycle is a repeated process and has a series of regulatory checkpoints. Over the last 25 years, the major progress of many studies was to identify the different factors and molecules that regulate the cell cycle. Regulation of the cell cycle is very crucial to detect and repair any genetic changes and to prevent uncontrolled cell division (Berges and Isaacs, 1993) (Udvardy, 1996; Pardee, 2006).

A dis-regulation of the cell cycle may lead to tumor formation. The word tumor (medically: neoplasm) describes a disease that contains an abnormal growth of cells. It can be either benign or malignant. Benign tumors are limited in size, are non-invasive and do not metastasize. However, malignant tumors, which form cancer, show rapid growth, invade adjacent tissues and spread to other locations. Cancer cells result from genetic changes during cell division. Genetic changes vary from gaining or losing chromosomes to mutations affecting the DNA nucleotide. Mutations happen in either oncogenes (genes that when mutated help to

turn normal cells into cancer cells), or tumor suppressor genes that are able to transform the normal cells into cancer cells (McAllister, 1965; Pardee, 2006).

2.2.1 Angiogenesis

Angiogenesis is the process of formation of new blood vessels from pre-existing vessels. Under normal conditions, it is fundamental in any reproductive cycle such as restoring blood flow to tissues after injury to enhance wound healing. However, in tumor cells, where rapid proliferation is expected, the formation of new blood vessels is needed to provide the tumor with nutrients and oxygen and allow tumor expansion (Kirsch et al., 2000).

Angiogenesis happens by activating the endothelial cells that lead to the formation of new blood vessels. This process is regulated by angiogenesis stimulators and inhibitors which binding to the tyrosine kinase receptors on the surface of endothelial cells (Neeman et al., 2007). This stimulates the endothelial cell growth. The best-studied examples are the vascular endothelial growth factors (VEGF) family (A, B, C and D) which bind to three different cell specific VEGF receptors (VEGFR) with different affinity. Another example is the acidic and basic fibroblast growth factors (FGF1 and FGF2) and their receptors. The functional involvement of these growth factors and their receptors has been extensively studied (Kirsch et al., 2000; Ashkenazi and Herbst, 2008). When the angiogenesis stimulating growth factors are produced in excess of the inhibitors, then blood vessel growth takes place whereas when the inhibitors are produced in excess, then angiogenesis halts.

In the early stages of tumor growth, the tumor can sustain itself through the passive diffusion of nutrients and oxygen, but when the tumor volume exceeds the critical value of two cubic millimeters, oxygen and nutrients have difficulty diffusing to the center of the tumor;

hence, the tumor starts forming a new network of blood vessels to act as carriers for oxygen and nutrients in order to sustain its rapid growth (Folkman, 2006). However, these blood vessels that result from tumor angiogenesis are characterized as poorly differentiated and fragile compared to normal mature blood vessels. These vessels are leaky due to the defective basement membrane and lack of smooth muscle cell lining and are sometimes unable to match the rapid growth of cancer cells, which results in areas of hypoxia and necrosis (Folkman, 2006). These structural defects of tumor vessels cause increased interstitial tissue pressure, impaired blood supply, and decreased oxygen supply in tumors compromising the delivery and efficacy of cytotoxic drugs and radiotherapy (Jain, 2001).

2.2.2 Metastasis

The leakiness of tumor blood vessels could induce tumor metastasis. Metastasis is defined as the transfer process of the tumor cells from the original tumor site to another site or a different organ. The outcome of this process varies according to the host and the tumor properties. Tumor cells can spread by three major routes. The first route involves direct extension, in which a tumor growing in a body cavity releases cells or fragments that seed serosal and/or mucosal surfaces to develop new growth. The second and third routes are via the lymphatic and hematogenous compartments of the circulatory system. Both the thin walled venules and the lymphatic channels show little resistance to tumor cell penetration. However, in arteries the walls are more resistant because they contain more elastic and collagen fibers. After infiltration to the blood stream, tumor cells undergo several interactions with platelets and other blood cells until they reach the capillary beds (Fidler, 1978). Numerous studies (Zeidman and Buss, 1952; Zeidman, 1957; Fisher and Fisher, 1967; Hagmar et al., 1984; Barbour and Gotley,

2003) have demonstrated that the rate of tumor cells passing through capillary beds does not depend on their size; rather, it depends on their ability to deform during transcapillary transport. Once they reach the extravascular environment, they continue to proliferate.

2.3 Tumor Treatment:

Cancer can be treated with many methods such as surgery, antiangiogenic drugs, chemotherapy and radiotherapy. This section will briefly discuss treatment methods where DCE-MRI can be used to monitor the effects on cancer growth.

2.3.1 Surgery

Cancer surgery is used to remove cancerous growths from the human body. Depending on the type of cancer and if it is localized to an organ with no metastasis, surgical removal might be sufficient to cure cancer patients.

2.3.2 Antiangiogenesis drugs

Antiangiogenic drugs are designed to block the neovascularization process by preventing VEGF from binding with the receptors on the surface of the endothelial cells and thus inhibit formation of new blood vessels.

There are numerous angiogenesis inhibitors being tested in cancer patients. These angiogenesis inhibitors are categorized based on their mechanism of action. One category of angiogenesis inhibitors directly inhibits the growth of endothelial cells. Another category of the angiogenesis inhibitors are those that act on steps in the angiogenesis signaling cascade

(Cavallaro and Christofori, 2000; Zogakis and Libutti, 2001). For example, anti-VEGF antibodies block the VEGF receptors from binding with the VEGF growth factor.

2.3.3 Chemotherapy

Chemotherapy is a general term that involves using chemicals drugs that attack the genetic material inside the cell nucleus (DNA) and damage it. These chemicals invade the rapid dividing cells and, hence, stop the cell division and replication. Several classes of chemotherapeutic agents contain metal cations that are essential for their biological activities such as zinc and calcium (Tobias and Whitehouse, 1976; Levin, 1998).

2.3.4 Radiotherapy

Radiation therapy uses ionizing radiation beams to target the malignant tumor cells and stop its growth. The radiation beams are designed to react with the water inside the cell and ionize it, creating a free radical that can damage the DNA of the dividing cell and prevent it from growing or dividing. Tumor cells are unable to repair the DNA damage as they are not as differentiated as normal cells. Hence, this DNA damage causes the tumor cell to die or have slower proliferation (Mehta et al., 2000).

The radiation dose that is given to the patient will depend on the tumor location, type and stage as well as many other factors such as combining the treatment with chemotherapy or surgery and if the patient is treated with radiotherapy before or after the surgery.

2.3.5 Cancer Treatment Decisions

After cancer diagnosis, the ideal treatment is to remove the cancer completely by surgery. However, the choice of the treatment depends on many factors, such as the type of the cancer, rate of progression, stage and location. When the tumor has metastasized, it is not feasible to use surgery; chemotherapy or antiangiogenic drugs would be a better choice. Nevertheless, chemotherapy and antiangiogenic drugs have their limitations. Chemotherapy is limited by its toxicity to normal tissues, especially tissues with rapid growth. The problem with antiangiogenic drugs is, beside targeting the normal vessels, they target only one of many factors that cause angiogenesis in tumors while other factors continue stimulating the growth of new blood vessels (Loiselle and Rockhill, 2009).

Radiotherapy can be used to treat most types of solid cancer. Radiotherapy treatment dosage will depend on the radio-sensitivity of the cancer under treatment and the toxicity to normal tissues/organs surrounding the tumor.

Combined treatments are also considered; some studies (Wolff et al., 2002; Ma and Waxman, 2008; Loiselle and Rockhill, 2009) have reported better results by combining different chemotherapy drugs, chemotherapy with radiotherapy or antiangiogenic drugs, or surgery with any other modality.

Chapter Three

Theory of Dynamic Contrast-Enhanced Magnetic Resonance Imaging

3.1 Magnetic Relaxation:

The source of the MRI signal is the hydrogen nuclei contained in the body's water, which counts for almost 60% of the human body. Hydrogen nuclei behave as small bar magnets pointed in all directions with equal probability. However, when a subject is placed in an external magnetic field, each hydrogen nucleus tends to align and possesses a magnetic moment. This magnetization can be measured by an MRI scanner. The strength of the MR signal is proportional to many factors such as hydrogen nucleus (i.e., water proton) density inside the tissue scanned, strength of the magnet and the time required for magnetization that has been disturbed by a radiofrequency (rf) pulse to re-align together, which is called the longitudinal magnetization or spin lattice relaxation time T1. Magnetization is given by the following equation:

$$M_z(t) = M_0 * \left[1 - e^{-\frac{t}{T_1}} \right] \qquad [3.1]$$

where M_z represents magnetization parallel to the main magnet, M_0 is the original magnetization and T1 is the spin lattice relaxation time (Haacke et al., 1999).

In living tissue there are many proteins and other macromolecules mixed with water. These macromolecules can produce magnetic fields at the molecular level affecting proton orientations which can shorten T1 values compared to pure water and result in image contrast. Several paramagnetic ions, which have unpaired electrons, can be injected into the human body to generate a powerful magnet that affects the relaxation time in order to produce image contrast (LAUFFER, 1987; Caravan et al., 1999). Therefore, paramagnetic ions are used as MRI contrast

agents (CA) because they change the relaxation time of water protons and enhance the image contrast in T1-weighted images. Gadolinium is one example where it has seven unpaired electrons in its outer orbit. These electrons can affect the water protons and alter their orientations/directions, resulting in a shorter T1 value (Caravan et al., 1999). CA is typically administered as a bolus of fluid via a catheter injection into a peripheral vein such as the antecubital vein in humans and the tail vein in mice.

3.2 Theory of DCE-MRI:

DCE-MRI is based on running dynamic T1-weighted images through a volume of interest and repeating it with time. Every time the whole volume of interest is imaged is called a time point. The total number of time points is determined by the DCE protocol followed. T1-weighted images are collected by applying short echo time (TE) and short repetition time (TR). Images continue to be acquired before, during and after CA injection. Each time point is approximately seven to eight seconds. The changes in the signal intensity of these images will depend on the CA concentration which affects the T1 value of any tissue that has blood flow. In tumor tissue, where the blood vessels leak into the surrounding extravascular space, the T1 value will be shorter compared to the normal leak-free vessel tissues; hence, there will be higher signal intensity in the tumor tissue compared to the normal tissue.

Figures 3.1 and 3.2 show a DCE-MRI example for imaging a mouse with an established renal carcinoma in the right kidney. Signal enhancing took place after the CA was injected at time point 10 (Figure 3.1). More signal enhancement can be seen in the mouse's normal kidneys that have more blood flow compared to other surrounding tissues with less blood flow. For data analysis, the full kidney was selected as a region on interest (ROI) for the kidney tumor (KT)

(blue contour on left of T1 image) and the contralateral left normal kidney (NK) (red contour on

right of T1 image) as shown in Figure 3.2.
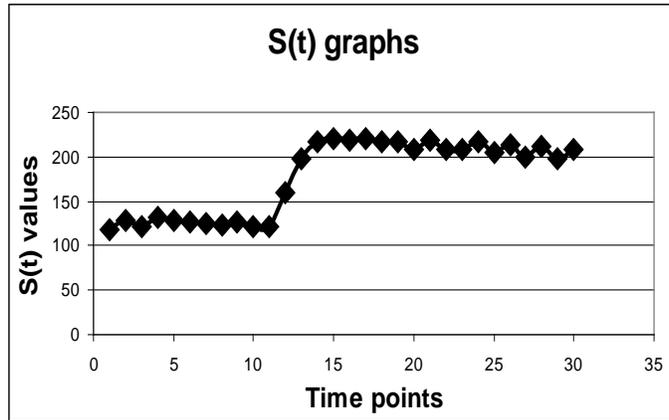
Figure 3.1: Signal enhancement after contrast agent injection. Contrast agent was injected at time point 10. DCE image are then acquired for 20 more time points.
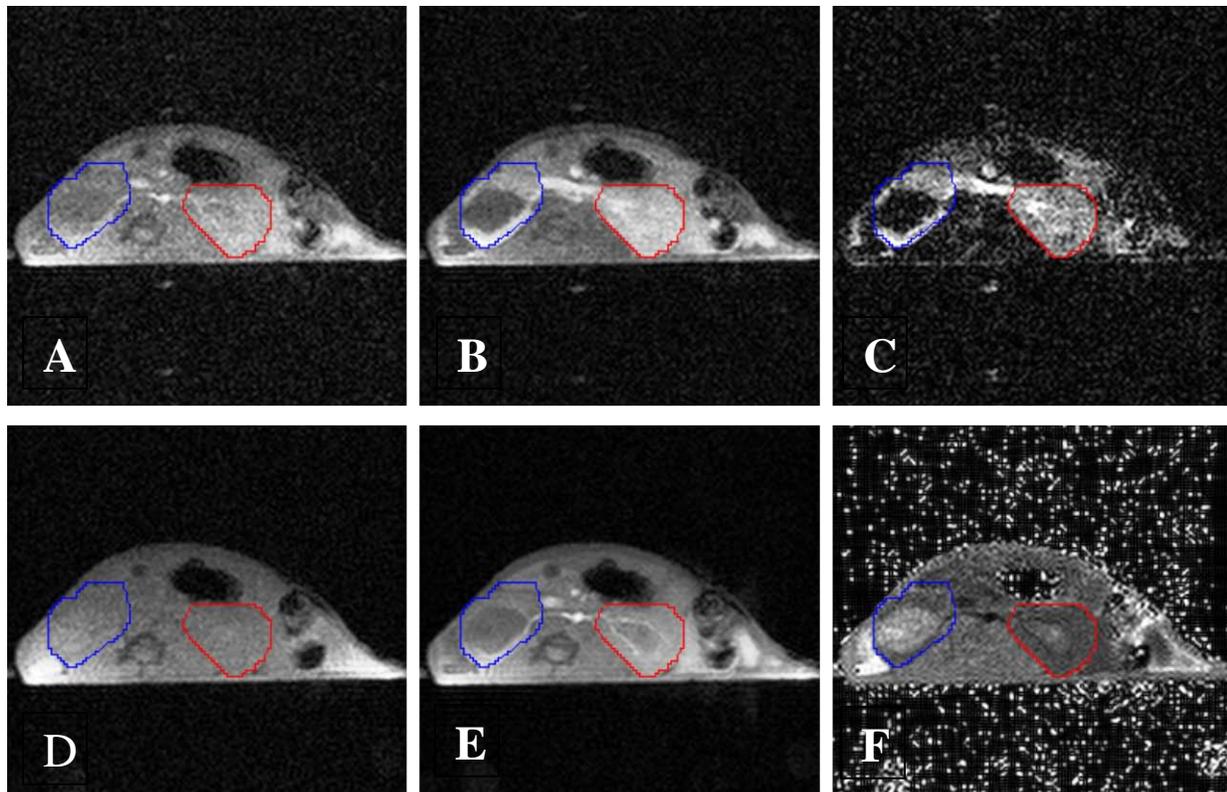
Figure 3.2: DCE-MRI example of mouse kidneys. A) Dynamic image pre-contrast, B) Dynamic image post-contrast, C) Subtracted Image, D) Flip Angle 5 Image, E) Flip Angle 30 Image and F) T1 image. Images A-F are used when processing a case wit DCE-MRI. Note the signal enhancement on the right kidneys with established tumor (blue contour) compared to the left normal kidneys (pink contour).

To perform DCE analysis we need to acquire T1-weighted images with high temporal resolution, extract the original T1 value for the tissue before CA injection (i.e. T1(0)) and define a method to extract tissue hemodynamic parameters. Dynamic DCE images are collected using a sequence called fast low angle short (FLASH). A FLASH sequence is a fast gradient echo imaging technique where the repetition times (TRs) for the data acquisition are very small compared to the T1 relaxation times of the tissues being imaged combined with a low flip angle rf pulse (Cron et al., 1999). Because of such short TR value, there will not be enough time for longitudinal magnetization to grow back to its equilibrium value M0, nor for the transverse magnetization to completely decay between each data acquisition step. Transverse magnetization might lead to coherent signal buildup; therefore, in a FLASH sequence it is purposefully destroyed or 'spoiled' before each subsequent acquisition step.

The changes in the DCE signal with time, S(t), for a given flip angle, can be obtained from the following FLASH equation:

$$S_\theta(t) = \frac{\rho_0 \sin\theta (1 - e^{-TR/T1(t)})}{(1 - e^{-TR/T1(t)}\cos\theta)} * e^{-TE/T2^*} \tag{3.2}$$

where ρ_0 is the spin density, θ is the flip angle, T2 is the transverse relaxation time, TR is the repetition time and TE is the echo time.

The changes in CA concentration with time can be calculated from the following equation:

$$C(t) = \frac{1}{a} * \left[\frac{1}{T1(t)} - \frac{1}{T1(0)} \right] \tag{3.3}$$

where "a" is the proportionality constant referred to as the longitudinal or T1 relaxtivity with units of $(mM)^{-1}s^{-1}$, and it is a property specific to the composition of the CA. T1(0) is the tissue T1 value prior to CA injection, and T1(t) represents T1 changes with time. C(t) calculation needs

both the T1(0) value and T1(t) function which will be explained in the following two sections

(Roberts et al., 2006; Haacke et al., 2007).

3.2.1 T1(0) calculations:

In order to calculate the initial T1(0) for a region of interest, two flip angle images are

collected with θ_1 and θ_2 respectively prior to CA injection. The signal from these two sequences

will equal

$$S_{\theta_1}(0) = \frac{\rho_0 \sin\theta_1 (1 - e^{-TR/T1(0)})}{(1 - e^{-TR/T1(0)} \cos\theta_1)} \qquad [3.4]$$

and $\quad S_{\theta_2}(0) = \frac{\rho_0 \sin\theta_2 (1 - e^{-TR/T1(0)})}{(1 - e^{-TR/T1(0)} \cos\theta_2)} \qquad [3.5]$

Given that TR, θ_1 and θ_2 are known, re-arranging the above equations in the form of

($y = mx + c$) we have

$$\frac{S_{\theta1}(O)}{Sin\,\theta_1} = \rho_0(1 - e^{-TR/T1(0)}) + \frac{S_{\theta1}(O)}{Tan\,\theta_1}e^{-TR/T1(0)}$$

$$\frac{S_{\theta2}(O)}{Sin\,\theta_2} = \rho_0(1 - e^{-TR/T1(0)}) + \frac{S_{\theta2}(O)}{Tan\,\theta_2}e^{-TR/T1(0)}$$

The slope m of the above equations is equivalent to $e^{-TR/T1(0)}$; plotting these two points

$((\frac{S_{\theta1}(t)}{Tan\,\theta_1}, \frac{S_{\theta1}(t)}{Sin\,\theta_1}), (\frac{S_{\theta2}(t)}{Tan\,\theta_2}, \frac{S_{\theta2}(t)}{Sin\,\theta_2}))$ and finding the slope of the line connecting them gives us

the value of T1(0) (see Figure 3.3).
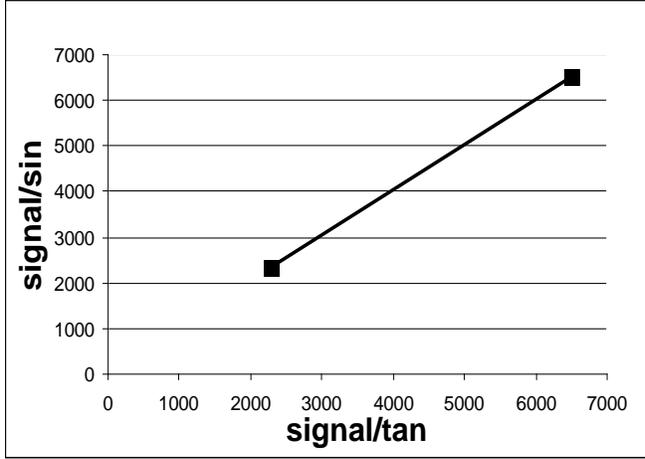
Figure 3.3: T1(0) calculations. Each point represents the ratio between the signal to flip angle used ($\frac{S_\theta(t)}{Tan\theta}, \frac{S_\theta(t)}{Sin\theta}$). The slope of the line connecting the two points (i.e., ($\frac{S_{\theta 1}(t)}{Tan\theta_1}, \frac{S_{\theta 1}(t)}{Sin\theta_1}$),($\frac{S_{\theta 2}(t)}{Tan\theta_2}, \frac{S_{\theta 2}(t)}{Sin\theta_2}$)) is equal to $e^{-TR/T1(0)}$. According to a given TR; T1(0) can be calculated. For more than two flip angles, linear regression will be used to find the slope.

For more than two flip angles, we calculate ($\frac{S_\theta(t)}{Sin\theta}, \frac{S_\theta(t)}{\tan\theta}$) for each angle and use linear

regression to find the slope and, accordingly, the T1(0) value, where for $y = mx + c$

$$m = \frac{n\sum(xy) - \sum x \sum y}{n\sum(x^2) - (\sum x)^2}$$

and

$$c = \frac{\sum y - m\sum x}{n}$$

However, there are multiple problems with this approach. First, the extraction of T1 is a noisy procedure. Second, the noise manifests itself as both a broadening of the histogram of data in the IAUC. Third, rf profiles in either 2D or 3D affect the resultant T1 calculation. Therefore, a new algorithm using a fixed T1(0) value has been proposed in our paper published in Magnetic Resonance in Medicine in 2007 (Section 3.3).

3.2.2 T1(t) calculations:

For a given TR, T1(t) can be calculated from rearranging equation # 3.2 as a ratio between the

signal at any time "t" to the initial signal before CA injection as in the following equation:

$$\frac{s(t)}{s(0)} = \frac{(1 - e^{-TR/T1(t)})}{(1 - e^{-TR/T1(t)}\cos\theta)} * \frac{(1 - e^{-TR/T1(0)}\cos\theta)}{(1 - e^{-TR/T1(0)})}$$

Simplifying the equation and assuming $y = \dfrac{s(t)}{s(0)}$ and $x = \dfrac{(1 - e^{-TR/T1(0)}\cos\theta)}{(1 - e^{-TR/T1(0)})}$

We get T1(t) = $\dfrac{-TR}{\ln\left[\dfrac{x - y}{x - y * \cos\theta}\right]}$ [3.6]

Figure 3.4-A shows the resulting T1(t) curve and its variation after CA injection. The C(t) value

can be found by substituting the T1(t) values and T1(0) in equation # 3.3 (see Figure 3.4-B).
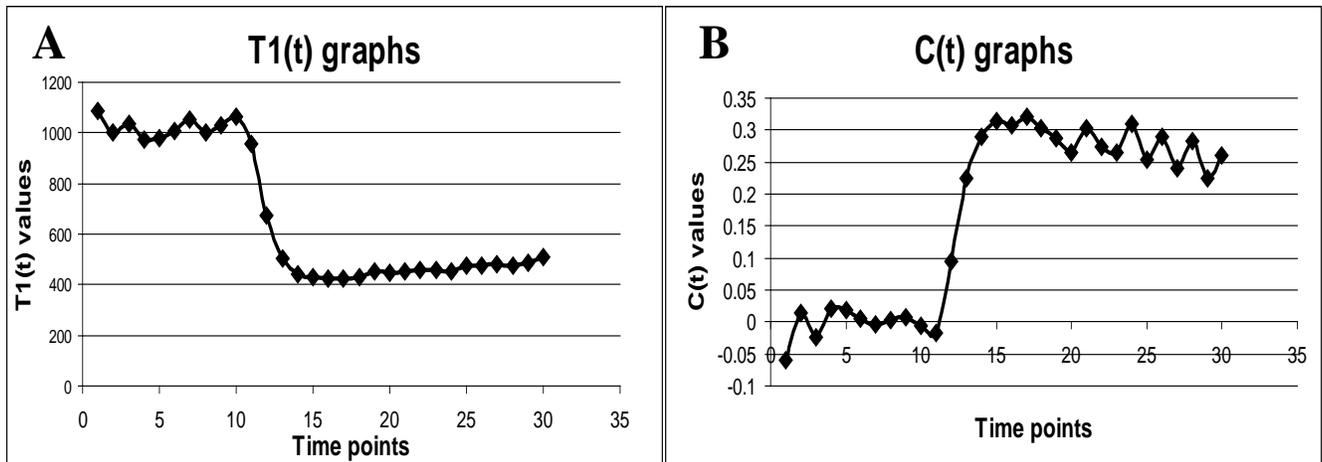
Figure 3.4: A) T1(t) curve, which represents the T1 value for the region of interest (ROI) with time. Notice after CA injection, the T1 value shortens. B) The C(t) curve, which represents the CA concentration in the selected ROI.

3.2.3 Model free DCE quantification

After calculating C(t) for each fixed T1(0), the initial area under the curve (IAUC) is calculated from the following equation:

$$IAUC = \sum_{t1}^{t2} C(t)\Delta t \qquad [3.7]$$

For each pixel, the next step in the process is to calculate the cumulative initial area under the curve (CIAUC), which represent the cumulative number of pixels counted within an ROI that corresponds to a given contrast uptake (xi) and normalize them to the total number of pixels (where xi = IAUC(i) for ($1 \leq i \leq$ N bins) in a given ROI) and n(xi) is the number of pixels with a value in that bin:

$$CIAUC(m) = \frac{\displaystyle\sum_{i=1}^{m} n(x_i)}{\displaystyle\sum_{i=1}^{N} n(x_i)} \qquad [3.8]$$

where N represents the last bin or maximum IAUC.

We define the R50 value as that value of xi where CIAUC(m) = 50% (the median value of the histogram) (Roberts et al., 2006). Although this value serves as the reference for the pre-drug treatment, when a fixed T1 is used we define instead the NR50, which is a normalized version of the R50 as defined below:

$$NR50 = (R50_{pre} - R50_{post}) / R50_{pre} \qquad [3.9]$$

where $R50_{pre}$ represents the R50 value before drug treatment and $R50_{post}$ represents the R50 value after drug treatment.

If the drug successfully reduces the vascular content, the CA uptake will be reduced. Therefore, the R50 will shift to the left (to a smaller value) and the NR50 will be a positive number between 0 and unity. If the tumor has not responded and/or the vascularity has increased,

the NR50 will be zero or negative. Figures 3.5 and 3.6 show the IAUC and CIAUC graphs respectively.
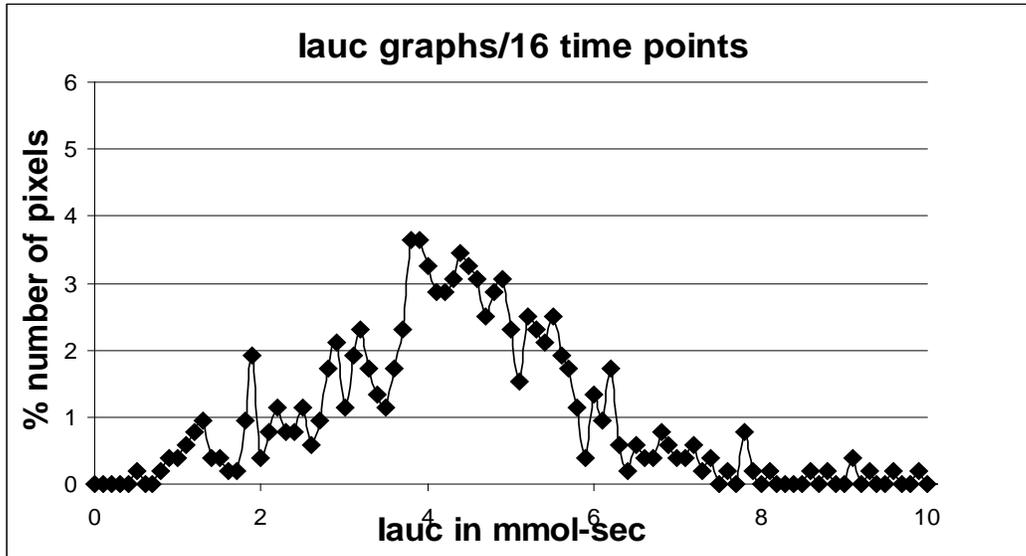
Figure 3.5: IAUC histogram, which represents the histogram of the number of pixels as a function of CA uptake in mmol-sec.
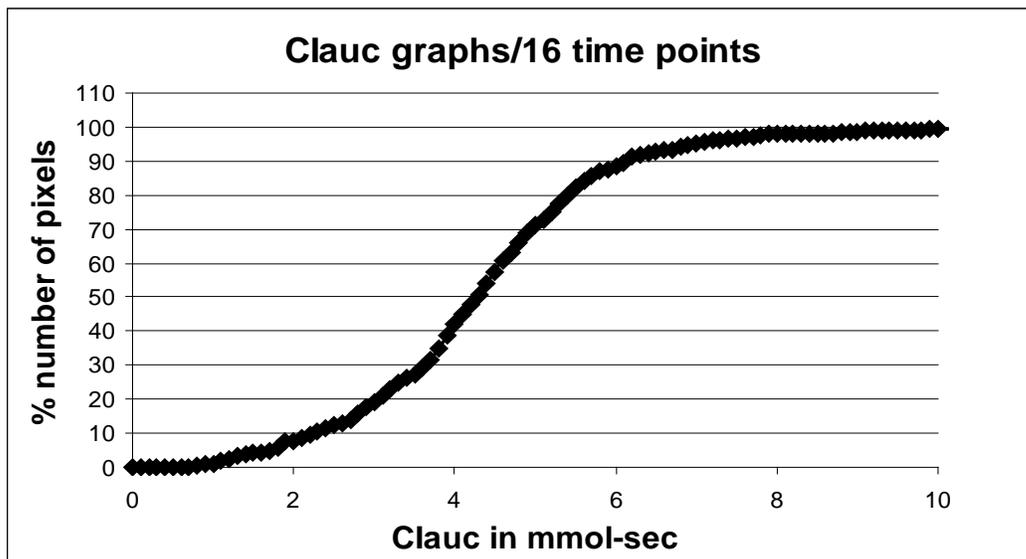
Figure 3.6: Cumulative distribution (CIAUC) of CA uptake.

3.3 New Algorithm for Quantifying Vascular Changes in Dynamic Contrast-Enhanced MRI Independent of Absolute T_1 Values (Haacke et al., 2007)

We introduce here a novel method to avoid the need to find absolute T1 values and dramatically improve the signal-to-noise ratio (SNR) in processed DCE-MRI data. We hypothesized that using a fixed value for T1(0) would eliminate most of the effects of the noise from the calculations of T1(t). Further, it would increase the accuracy of the DCE-MRI method and would make it possible to utilize data even when the multi flip angle (FA) data used to find T1(0) is faulty.

To avoid the effects of noise from the multiple FA images in calculating T1(0), we proposed to force all T1(0) values from the selected region of interest (ROI) to be equal to a fixed value close to that of the actual T1 value of the tissue. This approach should dramatically enhance the SNR of the calculations and make the method much more robust in a clinical setting.

3.3.1 Materials and Methods:

We test our hypothesis using simulated data. We started by creating a series of images with a range of T1 values (250 ms, 500 ms, 1000 ms and 1500 ms) at two different FA of 5º and 13º. Then a series of eight DCE images with known values of C(t) was generated.

$$C(t) = C_0 (1 - e^{-at}) e^{-bt} \qquad [3.10]$$

T1(t) is found for T1(0) starting values of 250 ms up to 2000 ms in increments of 250 ms. The values of TR = 3.8 ms and ρ_o (to mimic real human data) were inserted into Eq. [1]. Two noise values were added (Gaussian noise determined with the Box-Mueller method (16)) to the FA 5° and 13° images (SD=40 a.u., and SD =80 a.u. with mean =0). With these datasets the effects of noise were simulated for T1, IAUC, CIAUC, and R50.

The 50% mark (R50) of the CIAUC was used to represent a vascular measure for each of the two experimental conditions of pre (a=1/4, large values of *a* represent rapid uptake) and post (a=1/8, small values of *a* represent slow uptake) CA injection. The two R50 values pre drug treatment and post drug treatment were used to quantify the normalized change in contrast uptake (presumably due to vascular changes in the tissue). The normalized NR50 is calculated from NR50 = (R50$_{pre}$ – R50$_{post}$) / R50$_{pre}$, and this value is examined with a fixed T1(0) ranging from 250 to 2000 ms in 250 ms increments. If NR50 remains constant independent of T1(0), then the method can be considered a robust technique which can be used for all tissues in the body.

Estimating T1 from Simulated Data

The simulated data were then analyzed as discussed above to find T1(t) in the noisy data, extract C(t), find IAUC, and finally find the CIAUC. For the conventional approach, two FAs of 5° and 13° are used to obtain T1(0). Alternatively, we chose instead to fix T1(0) to one of 750 ms, 1000 ms, 1250 ms, 1500 ms, 1750 ms, or 2000 ms. All simulations are performed for a single input T1 representing a homogeneous tumor.

3.3.2 Results

The effect of noise on T1(0) is demonstrated in Figure 3.7 for various T1(0) values and SNR. Clearly, the noise plays a key role in broadening the T1(0) estimates because there is noise present in the multi-FA images (here we used 2 FAs, 5° and 13°) and noise present in the dynamic images. The larger the noise value, the broader the distributions become and the more skewed they become toward higher T1(0) values. Practically, such a large spread in T1(0) will further distort the CIAUC if the analysis method discards what look like noise points or points

which have a T1 that is too high. Therefore, the estimates for the calculated values are a conservative estimate as to how inaccurate they can become.
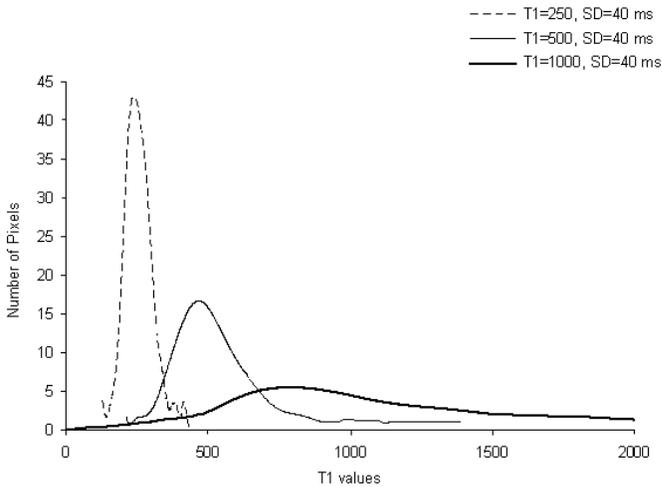
Figure 3.7: Histogram of $T1(0)$ calculated for a noise SD = 40 a.u. using $T1(0)$ equal 250 ms, 500 ms, and 1000 ms. Note the asymmetry of the T1 values about the mode with a large tail to the right toward higher T1. This skewness leads to an overestimate (bias) of the estimated mean value for T1.

Using a fixed T1(0), the spread in T1(t) is dramatically narrowed, leading to better estimates of the IAUC (Figure 3.8) and CIAUC (Figure 3.9). The behavior of the bad points is clearly observed with a spike at CIAUC at zero in Figure 3.9-b when T1act is 1000 ms and the noise level is SD = 80 a.u. The same figure also shows a normalized curve for the same values which clearly discards the counting of the bad points in the calculation of the CIAUC values. As expected, when T1(0) fixed is greater than the original T1(0), C(t) is reduced and the IAUC shifts to the left. We also observe that the IAUC narrows relative to the ideal values.
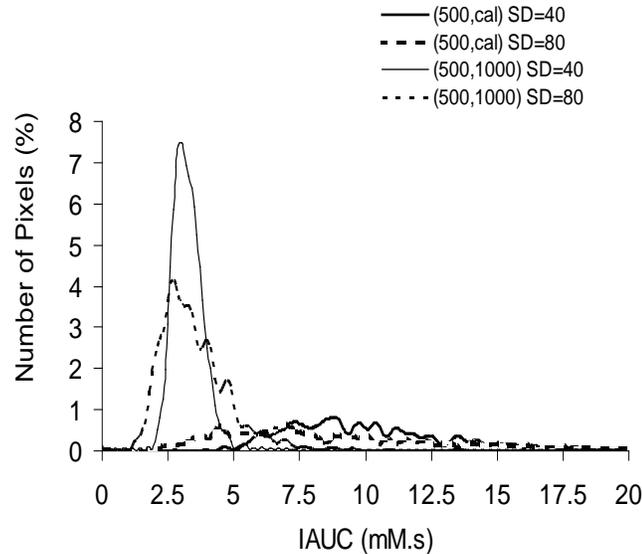
Figure 3.8. Histograms of the number of pixels as a function of contrast uptake in mMs. Simulated data were created with T1(0) fixed to 1000 ms and calculated for a T1(0)act of 500 ms, with SD=40 a.u., SD=80 a.u., $c_o = 2$ and the exponential constant value of a = 1/4. Note the shift to the left of the IAUC for T1(0) fixed to 1000 ms and the spread of the IAUC for growing noise levels. The spread of the IAUC is significant when the calculated approach was used. This demonstrates the robustness to noise of the T1(0) fixed method.
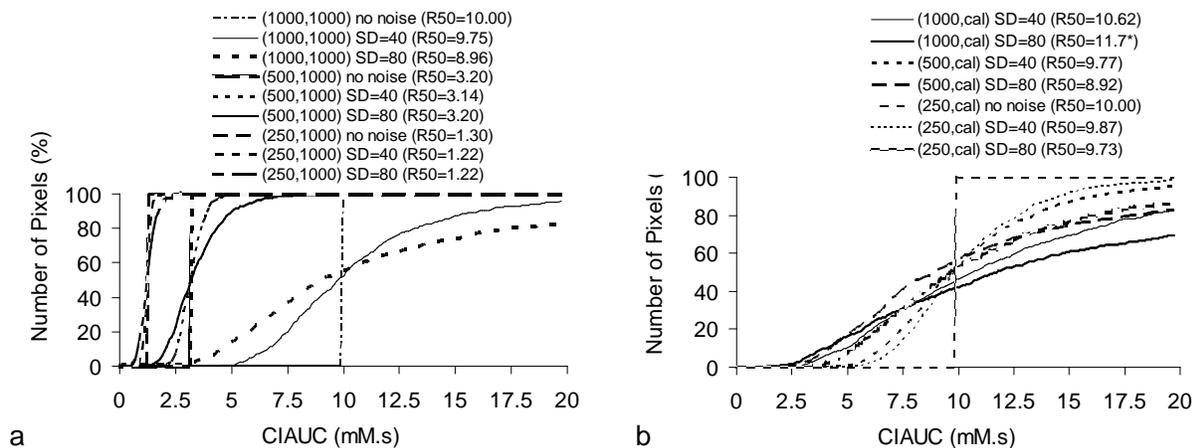
Figure 3.9. Cumulative distribution functions as a function of contrast uptake in mM.s. Simulated data were created with T1(0) fixed to 1000 ms (**a**), and calculated (**b**), with no noise and levels of noise SD=40 a.u., SD =80 a.u., $c_o = 2$, and the exponential constant value of a=1/4. T1act=250 ms, 500 ms and 1000 ms. Observe in (**a**) that the 50% CIAUC mark crosses for the T1(0) fixed, while it deviates from the 50% of the total number of pixels when being calculated from the FLASH equation (**b**). Only one no noise plot is shown since they all overlap each other (dotted line). Note that the CIAUC plots are broader for the calculated T1(0) case. The 50% CIAUC values are shown in the table to explain the above description. (*This value is calculated from the zero-removed dataset.)

26

Since the goal of the DCE experiments is to determine the percentage of vascular change, it would appear that the use of a fixed T1(0) method may be suitable to draw the correct conclusions despite the fact that the calculated C(t) will not be physiological. The only important element of this calculation is the correct prediction of the tissue response to vascular change from the drug treatment.

To test this hypothesis we used the two different models of CA uptake described above. Table 3.1 shows the ratio of the IAUC value at its peak over the full width at half magnitude (FWHM) for different values of tissue T1(0) and fixed T1(0). This measure shows that although the IAUC histogram may shift to the left, the FWHM narrows in proportion to the shift, making the ability to measure R50, and hence NR50, just as sensitive to the measure that would have taken place had the exact values of T1(0) been used. In fact, it can be seen that using a larger T1(0) often increases this ratio, which means that it remains a very sensitive means by which to judge the NR50 even for larger T1(0) values than the actual T1(0).

The NR50 variations for the different choices of fixed T1(0) in the pre/post-tumor treatment model described earlier are shown in Table 3.2. When the correct value of T1(0) is used, the NR50 in this model is 0.34. When a higher value is used this drops to 15% to 20% less than 0.34 or between 0.27 and 0.30. The key element here is that these values are close to 30% and do not vary wildly. The standard error of these measurements is consistently 3% (6%) for fixed T1(0) and 6% (12%) or more for the calculated data with an SD of 40 a.u. (80 a.u.) when evaluated with a fixed T1(0) of 1000 ms.

Table 3.1: The IAUC value at the peak of the histogram over the Full Width at Half Magnitude (FWHM) for varying values of tissue T1(0) (referred to here as $T1(0)_{act}$) and the forced fixed value of T1(0) (the value of T1(0) is given in ms).

	IAUC(peak value)/FWHM			
	a=1/4		a=1/8	
$T1(0)_{act}, T1(0)_{fixed}$	SD=40 a.u.	SD=80 a.u.	SD=40 a.u.	SD=80 a.u.
250, 250	2.28	1.17	2.25	0.90
250, 500	3.64	1.30	2.48	1.21
250, 750	4.17	1.17	2.33	1.06
250, 1000	4.77	1.46	2.36	1.64
250, 1250	3.92	1.27	2.13	1.20
250, 1500	4.00	1.32	3.11	1.13
250, 1750	3.76	1.44	2.94	1.30
250, 2000	3.93	1.45	3.15	1.37
500, 500	1.36	1.24	1.48	1.06
500, 750	2.57	1.12	1.94	1.14
500, 1000	3.03	1.52	2.39	1.37
500, 1250	3.10	1.13	2.46	1.31
500, 1500	3.11	1.17	2.39	1.31
500, 1750	3.20	1.24	3.25	1.05
500, 2000	2.91	1.33	3.45	1.39
1000, 1000	1.07	0.84	1.00	1.09
1000, 1250	1.01	0.81	1.42	1.35
1000, 1500	1.45	0.81	1.49	1.21
1000, 1750	1.78	0.86	1.90	1.04
1000, 2000	1.68	0.81	1.84	1.17
1500, 1250	0.94	0.82	0.93	0.82
1500, 1500	0.88	0.84	1.26	0.84
1500, 1750	0.87	0.72	1.26	0.83
1500, 2000	0.96	0.84	1.26	0.82

Table 3.2: The NR50 = [R50 (a=1/4) - R50 (a=1/8)] / R50 (a=1/4), for no noise, and noise levels of SD= 40 a.u. and SD= 80 a.u.. From Table 1, the SNR ranges from 5:1 to 37:1 depending on the T1 of the tissue. The table below exemplifies the fact that lower T1 values lead to higher SNR and vice versa.

$T1(0)_{act}$ (ms)		T1(0) (ms) fixed							
		250	500	750	1000	1250	1500	1750	2000	cal
No Noise	250	**0.34**	0.29	0.27	0.27	0.27	0.26	0.27	0.26	0.34
	500		**0.34**	0.30	0.28	0.27	0.26	0.26	0.26	0.34
	1000				**0.34**	0.31	0.29	0.28	0.28	0.34
	1500						**0.34**	0.32	0.30	0.34
SD=40 a.u.	250	**0.34**	0.29	0.28	0.27	0.27	0.26	0.26	0.26	0.35
	500		**0.34**	0.29	0.28	0.27	0.26	0.25	0.25	0.34
	1000				**0.34**	0.31	0.29	0.28	0.28	0.35
	1500						**0.34**	0.32	0.30	0.35
SD=80 a.u.	250	**0.34**	0.29	0.28	0.27	0.27	0.27	0.26	0.26	0.34
	500		**0.36**	0.31	0.30	0.29	0.28	0.28	0.27	0.30
	1000				**0.33**	0.31	0.29	0.28	0.27	0.31
	1500						**0.31**	0.30	0.29	0.16

3.3.3 Discussion and Conclusion

Robustness of the Fixed T1 Method

Current DCE analysis requires the calculation of T1(0) and subsequently T1(t). Noise in the experiments leads to very poor behavior of the extracted C(t) values and the IAUC. This sensitivity to T1(0) and the effect of the noise on the spread of T1(0) estimates can be effectively eliminated by forcing T1(0) to a fixed value, preferably greater than the actual T1(0) of the tissue under investigation. The results indicate that the IAUC became much more stable. The spread in

T1 and therefore in the IAUC in the noisy cases was so broad that T1 values ranged from almost zero to 3000 ms. This broad spread was dramatically reduced using the fixed T1(0) approach. Clearly, any programmatic issues dealing with noise and cutoff issues would bias the distribution and cause much worse shifts than what was shown in the simulated results. These problems do not occur when using the fixed T1(0) approach. (A stable IAUC can be very important if one is evaluating the histograms for shifts rather than the CIAUC. If this approach is taken, issues related to noise spikes and erroneous shifts in the CIAUC can be avoided.)

Through our simulations we observed that a single T1(0) can be used for the entire image. This is not necessary, though, as each tissue could in theory have its own T1(0) fixed in the ROI analysis. Performing this operation on both pre- and post- drug treatment cases should make it possible to obtain a reliable estimate for the relative changes shown by the R50 changes of the tissue. This also has the advantage that if data at different FAs are corrupt or not collected, the DCE acquisition still has value. Using the relative changes in R50 via NR50 may also reduce any inherent errors in calculating T1 that come from variations in T2* caused by the CA itself (17).

By using a fixed T1(0), we are forced to consider relative changes in R50 since we no longer have absolute T1(t) information. This is accomplished using the NR50. Ideally, the NR50 would prove to be identical between the two methods, and this is not far from the case, as shown in Table 3.2 The ideal changes expected in the two different models of C(t) uptake should have an NR50 equal to 0.34 (or a 34% shift to the left of the R50). In practice, with the fixed T1(0) approach they are closer to 0.27 to 0.30. We evaluated a number of practical cases and found that the error in tumor R50 variability can be as high as 0.17; thus, we chose 0.34 as a 2 SD model. Therefore, to err on the safe side, it would be wise to keep 0.34 as the $P = 0.025$ cutoff point

above which we could consider the effect of a vascular shift to be real. This choice is in agreement with a very recent publication (Roberts et al., 2006) and earlier works (Galbraith et al., 2002; Dale et al., 2003) suggesting that 30% is a adequate cutoff in a clinical environment. Our results show, however, that the actual white noise contribution is only 6–12% with SNR available on 1.5T systems today. Therefore, this 30% value is quite conservative and likely to be quite safe in drawing conclusions about actual changes in the NR50.

In the simulations, we used a specific set of T1 values as reasonable estimates of the clinical situation. Measuring the T1(0) value of the muscle, liver, and tumor in a series of 22 DCE-MRI experiments, we found that T1(0) for the muscle was 855 ms (SD = 180 ms), T1(0) for the liver was 680 ms (SD = 150 ms), and T1(0) for the tumor was 1400 ms (SD = 230 ms). Therefore, we chose to use the rather general values of 500 ms, 1000 ms, 1500 ms, and 2000 ms to cover the spectrum of values for tissue and tumors.

We also evaluated the effect of bin size in estimating the IAUC and the CIAUC as well as the R50 and NR50. For values of 0.01–0.05 mM.s, we obtained the same NR50 values to within 0.01, but large effects were observed when the bin size was 0.1 or higher.

Finally, tissue T1(0) heterogeneity will affect both the fixed and calculated approaches. To investigate this we simulated a variety of heterogeneous models with varying T1(0) from 250–1500 ms and found that the NR50 behaves in a similar fashion to the homogeneous case presented here.

3.4 DCE-MRI Requirements:

To conduct a successful DCE-MRI experiment several requirements should be met when designing an experimental protocol such as the following: high temporal and spatial resolution, volume coverage, image signal to noise ratio (SNR), access to arterial input function (AIF), and suitable contrast agent (CA) dosage.

3.4.1 High temporal and spatial resolution:

Vascular heterogeneity within the tumor can affect the temporal and spatial resolution required of DCE-MRI in several ways. High temporal resolution is very important to decrease the error in estimating DCE parameters. One impact is the need to sample the entire volume to take full advantage of this non-invasive method. If the study aims to characterize the tumor, failure to sample the entire tumor could result in sampling errors of the type associated with invasive assays, i.e. the region sampled is not representative of the entire tumor. Tumor simulations suggest to sample the AIF every 1 sec and tissue signal every 4 sec in order to keep the error in model parameters below 10%. This is due to the highly permeable and highly vasculature tumor (Henderson et al., 1998).

High spatial resolution is needed to overcome problems such as partial volume effect which might lead to masking important pathology details (Furman-Haran et al., 2001). It should be in the order of standard structural MRI data acquisitions.

3.4.2 Volume coverage and image SNR:

For tumor volume acquisition, it is very important to cover the whole tumor volume, especially when a comparison study is planned (Zhu et al., 2000). However, the imaging

protocol should optimize the above mentioned requirements (i.e., high temporal and spatial resolution and adequate volume coverage) with an acceptable signal-to-noise ratio (SNR). Image SNR can affect the quality of parametric maps that can be produced from the original DCE images.

3.4.3. Arterial Input Function (AIF):

Upon reviewing the literature, we encountered three main approaches to measure AIF: by inserting an arterial catheter into the subject and take blood samples to measure it, by assuming AIF is the same for all subjects (Tofts and Kermode, 1991), or by obtaining AIF from DCE data. Nevertheless, these approaches have many problems, such as being invasive, having poor temporal resolution, being relative ambiguous concerning the actual time, influencing of both inter and intra subject variations in AIF, and, finally, requiring the presence of a large vessel within the FOV as well as the need to devoid partial volume or flow effect (Parker et al., 1996; Cha, 2004). These problems make AIF very difficult to calculate.

3.4.4. Contrast agent dose and administration time:

In DCE-MRI a clinical protocol demonstrates that both the dose and bolus administration is needed. Many studies (Hulka et al., 1995; Henderson et al., 1998) demonstrate that shorter injection of the CA is desirable. Shorter injection time can help reduce the effects of noise modeling errors. However, we need to acquire high temporal resolution to cope with these values.

Higher CA dosing can enhance the signal intensity in T1-weighted images up to some limit. Some sequences suffer from high susceptibility sensitivity, which might lead to a drop in

signal intensity as a result from high CA concentration in the arteries in the region of interest (Tofts, 1996).

3.5 DCE-MRI Artifacts:

As we mentioned earlier the main source of error in DCE experiments is estimating the T1(0) value (Parkera et al., 2000). Usually two points are collected to calculate T1(0) which has more exponential components than liner components. This explains our use of the fixed T1(0) approach (Haacke et al., 2007). Another complication in DCE is to choose a model that describes the behavior of the CA uptake and clearance by the tumor. It is still not clear if complicated yet well-characterized models are more or less useful in understanding and assessing the treatment results compared to simple yet more noisy models. Other imaging artifacts also affect the DCE results such as patient motion, errors in CA relaxivity and water exchange rates. Further, CA increase the susceptibility effect and changed the T2* value; hence, this will result in inaccurate T1(t) measurements (Roberts, 1997).

Chapter Four

Dynamic Contrast-Enhanced Magnetic Resonance Imaging of Vascular Changes Induced by Sunitinib in Papillary Renal Cell Carcinoma Xenograft Tumors

Gilda G. Hillman*, Vinita Singh-Gupta*, Hao Zhang*, Areen K. Al-Bashir†,‡, Yashwanth Katkuri†,‡, Meng Li†,‡, Christopher K. Yunker*, Amit D. Patel*, Judith Abrams§ and E. Mark Haacke†,‡

*Department of Radiation Oncology, †Department of Radiology, ‡Department of Biomedical Engineering, §Integrated Biostatistics Unit, Wayne State University School of Medicine. Detroit, MI 48202, USA.

Corresponding Author:

Gilda G. Hillman, Ph.D.

Department of Radiation Oncology

15 Hudson-Webber Cancer Research Center

4100 John R. Road

Detroit, MI 48201, USA

Tel: (313) 576-8257

Lab: (313) 576-8242

Fax: (313) 576-8265

E-mail: hillmang@karmanos.org

4.1 Abstract

To investigate further the antiangiogenic potential of sunitinib for renal cell carcinoma (RCC) treatment, its effects on tumor vasculature were monitored by dynamic contrast-enhanced magnetic resonance imaging (DCE-MRI) using an orthotopic KCI-18 model of human RCC xenografts in nude mice. Tumor-bearing mice were treated with various doses of sunitinib, and vascular changes were assessed by DCE-MRI and histologic studies. Sunitinib induced dose dependent vascular changes, which were observed both in kidney tumors and in normal kidneys by DCE-MRI. A dosage of 10 mg/kg per day caused mild changes in Gd uptake and clearance kinetics in kidney tumors. A dosage of 40 mg/kg per day induced increased vascular tumor permeability with Gd retention, probably resulting from the destruction of tumor vasculature, and also caused vascular alterations of normal vessels. However, sunitinib at 20 mg/kg per day caused increased tumor perfusion and decreased vascular permeability associated with thinning and regularization of tumor vessels while mildly affecting normal vessels as confirmed by histologic diagnosis. Alterations in tumor vasculature resulted in a significant inhibition of KCI-18 RCC tumor growth at sunitinib dosages of 20 and 40 mg/kg per day. Sunitinib also exerted a direct cytotoxic effect in KCI-18 cells in vitro. KCI-18 cells and tumors expressed vascular endothelial growth factor receptor 2 and platelet-derived growth factor receptor β molecular targets of sunitinib that were modulated by the drug treatment. These data suggest that a sunitinib dosage of 20 mg/kg per day, which inhibits RCC tumor growth and regularizes tumor vessels with milder effects on normal vessels, could be used to improve blood flow for combination with chemotherapy. These studies emphasize the clinical potential of DCE-MRI in selecting the dose and schedule of antiangiogenic compounds.

4.2 Introduction

Renal cell carcinoma (RCC) incidence has increased in recent years with approximately 54,390 new cases each year in the United States. The disease is responsible for an estimated 13,010 deaths each year (Jemal et al., 2008). Nearly half of the patients present with localized disease that can be treated by surgical removal (Haas and Hillman, 1996). However, one third of the patients have metastatic disease at first presentation, and 20% to 30% of the patients treated for localized RCC subsequently develop metastatic disease that frequently involves the lungs (Haas and Hillman, 1996). The median survival of patients with metastatic RCC ranged from 8 to 11 months (Haas and Hillman, 1996; Flanigan et al., 2001). The treatment of metastatic RCC remains a significant challenge, but recent developments in antiangiogenic therapy have improved targeting these highly vascularized tumors.

The vascular endothelial growth factor (VEGF), produced by tumor cells and associated stromal cells, is a key growth factor in the angiogenic process, which promotes the proliferation, migration, and invasion of endothelial cells and plays a role in vascular permeability. Targeting the tumor vasculature with antiangiogenic therapy has been shown to suppress the growth of established tumors in mice, leading to several clinical trials with different angiogenesis inhibitors (Kerbel and Folkman, 2002). Numerous antiangiogenic compounds recently developed include anti-VEGF antibodies and inhibitors of receptor tyrosine kinases (RTKs). The drug sunitinib (SU11248 or Sutent) is a small-molecule RTK inhibitor that has demonstrated antitumor and antiangiogenic activities in mouse xenograft models. Sunitinib targets and inhibits signaling of several RTKs including platelet-derived growth factor receptor (PDGFR), VEGF receptor (VEGFR), c-kit protooncogene, and FMS-like tyrosine kinase 3 (Abrams et al., 2003; Murray et al., 2003; O'Farrell et al., 2003; Xu et al., 2005). Sunitinib exhibits direct antitumor activity by

inhibiting RTKs that are expressed by cancer cells and are involved in signaling for cancer cell proliferation. Sunitinib also exhibits antiangiogenic activity by inhibition of signaling through VEGFR-2 and PDGFR-β RTKs expressed on endothelial cells or stromal cells. Initial clinical trials with sunitinib for metastatic RCC showed significant responses in multiple metastatic sites and in primary tumors resulting in 40% partial response rate with a median time to progression of 8.7 months (Motzer et al., 2006). These studies justified approval of sunitinib by the FDA in January 2006 for RCC treatment. In a phase 3 multinational study of 750 patients with metastatic RCC, randomized to sunitinib or interferon α, the response rate to sunitinib was 31%, with median progression-free survival (PFS) of 11.7 months and a median survival of 28 months (Motzer et al., 2007). A recent update of this trial documented an objective response rate of 47% with 11 months of median PFS for sunitinib versus 12% objective response rate and 5 months of PFS for interferon α (Kollmannsberger et al., 2007). Although the results with sunitinib therapy are impressive, long-term control of the disease is still not achieved. In addition, several trials documented adverse effects of cardiotoxicity in some of the patients, probably as a result of alterations to normal vasculature (Jain, 2005; Chu et al., 2007; Schmidinger et al., 2008; Telli et al., 2008). Therefore, further investigations with sunitinib dose adjustments are warranted to decrease the impact on vital organs such as the heart and the kidney.

The goal of our study was to investigate the effect of lower and potentially less toxic doses of sunitinib on tumor vasculature to establish the conditions for combination therapies to determine whether a combined strategy could maintain and improve efficacy. Disruption of the tumor vasculature to deprive tumor cells from nutrients by sunitinib, given in conjunction with cytotoxic therapies, could be more effective in preventing progression of metastatic RCC. However, this approach could be a paradox given that complete destruction of tumor vasculature

could compromise the efficacy of chemotherapy or radiotherapy because both depend on blood flow to the tumor for delivering oxygen and drugs (Jain, 2001). To improve the blood flow in tumors, the concept of "normalization" of tumor vasculature is based on the regularization of tumor vessels by pruning or destroying immature and inefficient blood vessels through elimination of excess endothelial cells, and it has shown promise for combination therapies (Browder et al., 2000; Lee et al., 2000; Wildiers et al., 2003). The process of tumor angiogenesis involves proliferation of abnormal vessels that are enlarged, disorganized, and leaky due to the defective basement membrane. These structural defects of tumor vessels cause increased interstitial tissue pressure, impaired blood supply, and decreased oxygen supply in tumors compromising the delivery and efficacy of cytotoxic drugs and radiotherapy (Jain, 2001). The challenge is to develop imaging technologies that monitor early vascular changes and induction of tumor vasculature normalization by antiangiogenic drugs for scheduling cytotoxic therapy.

We selected to use dynamic contrast-enhanced magnetic resonance imaging (DCE-MRI) to investigate the effect of sunitinib therapy on RCC tumor vasculature using a preclinical papillary RCC murine model. DCE-MRI is a noninvasive approach, currently used in humans that can detect early changes in the tumor induced by antiangiogenic therapy as reported in human studies (Checkley et al., 2003; Hahn et al., 2008) and in preclinical animal models (Marzola et al., 2005). This method measures a combination of tumor perfusion and vessel permeability and allows the detection of changes in tumor vascularity, which occur at a much earlier stage in the treatment of tumors with antiangiogenic drugs than does shrinkage of tumor mass (Checkley et al., 2003; Hahn et al., 2008). Contrast agents typically consist of gadolinium (Gd)-based chelates with paramagnetic properties that are used to enhance signal from the tissue in clinical MRI. The contrast agent, injected intravenously, enters the extravascular extracellular

space through the capillary bed as a function of perfusion and permeability. The contrast agent that accumulates over time in the tumor can be then analyzed by MRI (Checkley et al., 2003; Hahn et al., 2008). Recent animal studies suggest that parametric images providing information on the morphology and function of the microvasculature of tumors can be obtained by Gd-DTPA–based DCE-MRI (Hillman et al., 2007).

DCE-MRI was performed using an orthotopic RCC model in athymic nude mice, which was established by subcapsular renal implantation of Karmanos Cancer Institute-18 (KCI-18) cells, a tumor cell line generated from a human papillary RCC specimen in our laboratory (Hillman et al., 2007). Vascular changes induced by various doses of sunitinib in tumor-bearing kidneys and normal contralateral kidneys were monitored by DCE-MRI and by histologic studies of tissue sections.

4.3 Materials and Methods

4.3.1 Orthotopic KCI-18/IK RCC Tumor Model

The human RCC cell line designated KCI-18 was established in our laboratory from a primary renal tumor specimen obtained from a patient with papillary RCC (nuclear grade 3/4) (Hillman et al., 2007). Cells were cultured in Dulbecco's modified Eagle medium with supplements (Hillman et al., 2007). After serial passages of KCI-18 cells in the kidney of nude mice, highly tumorigenic KCI-18/IK were generated (Hillman et al., 2007). KCI-18/IK cells were washed with Hank's balanced salt solution and subcapsularly injected at a concentration of 5×105 cells in 30 μl of Hank's balanced salt solution in the right kidney in 5- to 6-week-old female BALB/C nu/nu nude mice (Harlan, Indianapolis, IN) (Hillman et al., 2007). Mice were housed and handled under sterile conditions in facilities accredited by the American Association for the Accreditation of Laboratory Animal Care. The animal protocol was approved by the Animal Investigation Committee of Wayne State University.

4.3.2 Experimental Protocol

After injection of KCI-18/IK cells, a few mice were killed at early time points to assess tumor growth before initiating treatment. Small tumors were detectable by days 9 to 10 in the kidney. By days 10 to 12, mice bearing established kidney tumors (KTs) were treated with sunitinib (Pfizer, Inc,New York,NY). The drug was prepared in a carboxymethyl cellulose suspension vehicle, at dosages of 10, 20, or 40 mg/kg per day (SU10, SU20, or SU40, respectively) and given orally by gavage, once a day. Control mice were treated with vehicle only. Treatment was continued for 7 to 18 days. On the basis of initial experiments, early time points of 7-day sunitinib treatment were selected for DCE-MRI studies or for monitoring RTKs

expression to avoid incorrect analysis of advanced and large necrotic tumors in control mice. For DCE-MRI experiments, three mice per treatment group were imaged. To assess the therapeutic response of KTs to an optimal dosage of 40 mg/kg per day of sunitinib, 10 mice per experimental group were treated daily for 18 days. For sunitinib dose-response studies, eight mice per experimental group were treated daily with 10, 20 or 40 mg/kg per day of sunitinib. Mice were killed by day 28 after tumor cell injection, when the tumor burden in control animals was large (>1.5 cm × 1 cm in size compared with 0.7 cm × 0.25 cm for normal kidneys [NK]) to compare with tumor sizes in treated groups. Tumor-bearing kidneys were resected and weighed (Hillman et al., 2007).

4.3.3 Tissue Preparation for Histologic Diagnosis

At completion of experiments, mice were killed and KTs as well as the contralateral NKs were resected and processed for histologic diagnosis. All tissues were fixed in 10% buffered formalin, embedded in paraffin, and sectioned (Hillman et al., 2007). Sections were stained with hematoxylineosin (H&E) (Hillman et al., 2007). Tissue sections were also immunostained with anti-CD31 antibody (Ab; Thermo Scientific, Fremont, CA) using an avidin-biotin immunoperoxidase technique (Haacke et al., 2007; Hillman et al., 2007; Raffoul et al., 2007).

4.3.4 DCE-MRI Monitoring of Tumor Perfusion and Permeability and Tumor Size in KTs

Mice from control and sunitinib-treated groups were imaged by DCE-MRI. Mice were anesthetized by intraperitoneal injections of 0.35 ml of pentobarbital and 0.35 ml of ketamine at a concentration of 52.5 mg/kg then a catheter was inserted into their tail vein, which was attached to a syringe containing Gd-DTPA contrast agent (Magnevist, Berlex, Wayne, NJ). Mice

were positioned on a cradle heated by temperature controlled water and were given a second low dose of anesthetics of 15 mg/kg each in 0.1 ml to avoid motion problems while in the magnet. A 2-cm-diameter receive-only surface coil was placed over the tumor, and the cradle was placed inside an 11-cm inner-diameter transmit-only volume coil. DCE-MRI of mice was performed in the MR Research Facility at Wayne State University using a Bruker Biospec AVANCE animal scanner (Bruker, Karlsruhe, Germany) equipped with a 4.7-T horizontal bore magnet and actively shielded gradients. Anatomic imaging was done using a two-dimensional T2-weighted spin-echo scan (repetition time = 2000 milliseconds, echo time = 52.4 milliseconds) to get an overview of the kidney. Baseline imaging data of the kidneys were obtained using the short-repetition time DCE scan for 30 time points (7 seconds between time points). On time point 10, 100 μl of Gd-DTPA (0.125 mmol/kg) was injected into the tail vein catheter. This dose was selected based on preliminary Gd dose-searching experiments to obtain appropriate contrast for image analysis. Then, imaging data were acquired for 20 more time points. The imaging parameters for this multislice two-dimensional gradient echo scan were as follows: repetition time = 54.7 milliseconds, echo time = 2.9 milliseconds, flip angle = 30 degrees, field of view = 32 mm × 32 mm, slice thickness = 1.5 mm with 0.5-mm gap, matrix size = 128 × 128. Five slices were collected for each animal. Data were processed to determine changes in contrast agent uptake using the SPIN DCE software (Detroit, MI) (Haacke et al., 2007). For data analysis, the full kidney was selected as the region of interest (ROI) for the KT and the contralateral left NK. A threshold was selected to remove noise-only pixels in the image. Gd concentrations [C(t)] in the tissue were calculated for all pixels in the ROI and for each time point. Data from the C(t) curves were compiled for each pixel for 16 time points (112 seconds) after Gd injection to create the initial area under the curve (IAUC). The distribution of IAUC for the entire ROI is then

shown as a means to visualize the effects in every pixel in a single plot. The CIAUC is the cumulative initial area under the curve of the IAUC histogram. For quantitative analysis of vascular permeability, R50 (median) values are derived from CIAUC curves and correspond to the concentration of Gd at which 50% of the pixels have been included (Haacke et al., 2007). To evaluate the kinetics of uptake, washout, and leakage into the kidney tissue and tumor, the parametric color maps are used to show the initial rate of uptake, peak concentration and clearance of Gd in the tissue, and individual structures in each slice. The parameters measured in DCE-MRI for sunitinib-treated tumors were compared with those obtained for control tumors and NKs.

4.3.5 Statistical Analysis

Evaluation of the shape of the frequency distribution of tumor weights indicated that a log transformation was required to meet the assumptions of normal theory tests. Two-sample t-tests were used to assess the significance of differences in tumor weight between mice treated with SU40 and control mice. A linear model with indicator variables to parameterize dose was used to investigate the relationship of vehicle, SU dose, and tumor weight. The paired difference in weight between the NK and KT was calculated and compared between experimental groups. Adjustment for multiple comparisons between treatments was made using Holm's procedure to protect against inflated type I errors (Raffoul et al., 2007).

4.4 Results

4.4.1 DCE-MRI of KTs

To investigate the effect of sunitinib on tumor vasculature, mice bearing KTs were imaged by MRI before and after contrast Gd injection. We report the data of a representative experiment comparing three dosages of sunitinib, namely, 10, 20, and 40 mg/kg per day, to control mice treated with vehicle. These sunitinib dosages were selected based on previous animal studies demonstrating that 40 mg/kg per day of sunitinib, given daily, is a biologically active dosage.

For data analysis, the full kidney was selected as the ROI both for the right KT and the left NK (Figure 4.1-A, T1). Gd concentrations [C(t)] were calculated for all pixels in each ROI and for each time point, and the average C(t) over all pixels was plotted (Figure 4.1-B)(Haacke et al., 2007). C(t) values, obtained after Gd injection, were integrated during 16 time points (112 seconds) to create the IAUC112 histograms (Figure 4.1-C) and CIAUC (Figure 4.1-D). In control mice, Gd uptake was rapid in both the KT and NK. However, the kinetics of clearance of Gd in the KT were slow compared with faster clearance in the NK (C(t) in Figure 4.1-B). Indeed, the IAUC/CIAUC curves for the KT showed a pronounced shift to the right compared with NK, indicative of a greater retention of Gd (Figure 4.1, C and D). DCE-MRI of mice treated with SU40 revealed a pattern of Gd uptake that remained at a plateau with more retention of Gd in both kidneys compared with control mice. Retention of Gd was still greater in the KT treated with sunitinib than in the NK as observed by a shift to the right in IAUC/CIAUC curves relative to NK, but this shift was less pronounced than in control tumors (Figure 4.1, C and D). In mice treated with SU20, patterns of Gd uptake and clearance were identical in the KT and the NK (Figure 4.1-B). SU20 mice had IAUC and CIAUC overlapping with those of the NK, indicative

of improved tumor perfusion (Figure 4.1, C and D). Interestingly, the KT IAUC curve looked more regular and shifted to the left compared with KTs in control or SU40-treated mice, indicating decreased Gd retention. SU10 also seemed to change the kinetics of uptake and clearance in KTs, showing a shift to the left in IAUC curves compared with control or SU40-treated mice but less than with SU20-treated tumors (Figure 4.1, C and D). In the NK, SU10 caused milder changes in Gd uptake and clearance than SU20 or SU40 and resulted in an IAUC pattern comparable to that of NK in control mice (Figure 4.1, C and D). It should be noted that compared with tumors from control mice, sunitinib treatment at all tested dosages caused significant shifts to the left of IAUC curves of KTs, which were more pronounced with lower SU20 and SU10 doses than with a higher SU40 dose (as visualized relative to the black bar on top of each graph in Figure 4.1-C).

Vascular changes in NKs were observed with higher SU20 and SU40 dosages and were expressed by a shift to the right in IAUC curves compared with NKs of control mice. These data presented for one mouse per treatment group were consistently observed for two additional mice per group in the same experiment showing reproducibility of our findings.
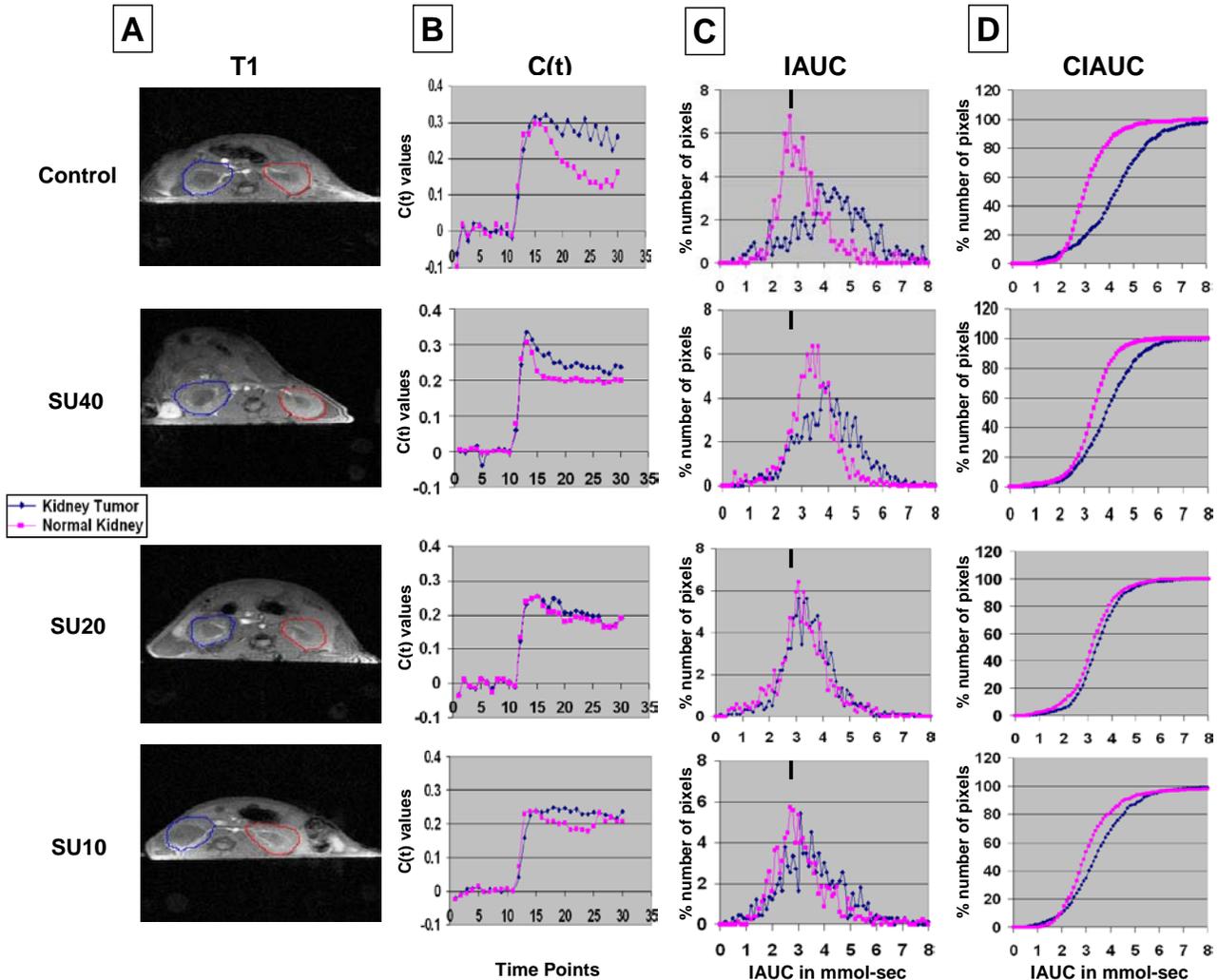
Figure 4.1. DCE-MRI of KCI-18 KTs. Mice bearing established tumors in the right kidneys were treated every day for 7 days with vehicle only (control) or with sunitinib at dosages of 40, 20, or 10 mg/kg per day (SU40, SU20, or SU10, respectively). Then, mice were imaged by DCE-MRI for 30 time points at 7-second intervals. (A) Baseline images were collected for the first during 10 time points before Gd contrast agent injection. At time point 10, Gd was injected in the tail vein, and images were collected for 20 more time points. For data analysis, the full kidney was selected as the ROI for the KT (blue contour on left of T1 image) and the contralateral left NK (red contour on right of T1 image). A threshold was selected to remove noise only pixels in the image. (B) The kinetics of Gd contrast uptake are represented in C(t) curves. (C) Data from the C(t) curves were compiled for 16 time points (112 seconds) after Gd injection to draw IAUC112. The small black bar indicates the peak position of NK in control mice and can be used as a reference for curve shifting in NKs and KTs treated with sunitinib. (D) The CIAUC graphs were derived from IAUC curves. In panels B, C, and D, blue lines are for KTs and pink lines are for NKs. Data from a representative mouse from each treatment group are presented.

To compare the patterns of Gd uptake in KTs versus NKs, R50 values for three mice per treatment group were derived from CIAUC curves for both KTs and NKs (Figure 4.2). The R50 (median) values correspond to the concentration of Gd at which 50% of the pixels have been included (Figure 4.2-A) (Haacke et al., 2007). A trend in lower R50 values was observed in SU10- and SU20-treated mice compared with control mice and SU40-treated mice for both R50 of KTs (Figure 4.2-B) and NKs (Figure 4.2-C). R50 values of KTs were then normalized to the R50 values of contralateral NKs for each mouse and shown as normalized R50 values (NR50) for three mice per group (Figure 4.2-D) (Haacke et al., 2007).We found that NR50 of KTs relative to NKs were consistently much smaller in SU20-treated mice in a range of 0.04 to 0.08 compared with a wide range of 0.12 to 0.43 in SU10-treated, SU40-treated, or control mice (Figure 4.2-D). When NR50 was calculated as R50 values of KTs from sunitinib-treated mice relative to KTs from control mice, NR50 of SU20-treated mice was consistently lower than that of SU40-treated mice (Figure 4.2-E). A trend to lower NR50 values was also observed with SU10-treatedmice (Figure 4.2-E). To assess the effect of sunitinib on contralateral NKs, R50 values of NKs from mice treated with sunitinib were normalized to NKs from control mice (Figure 4.2-F). TheseNR50 data of NKs showed lower values for SU10- and SU20-treated mice compared with SU40-treated mice (Figure 4.2-F).
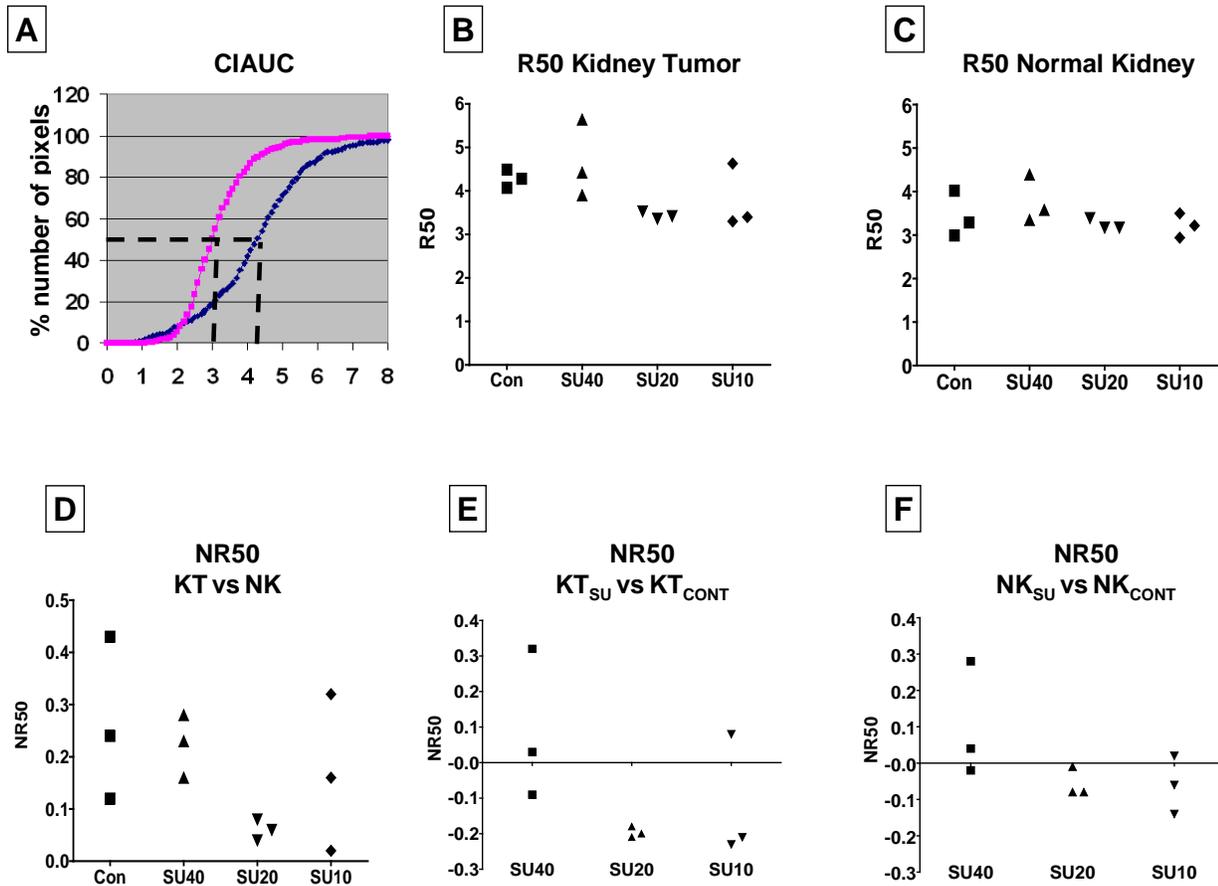
Figure 4.2. R50 quantitation of DCE-MRI data of KCI-18 KTs. (A) The R50 value is derived from CIAUC curves (as shown for control mouse) and corresponds to the Gd concentration at which 50% of the pixels have been included. (B) R50 of KTs from three mice per treatment group. (C) R50 of contralateral NK from the same three mice per treatment group shown in panel B. (D) NR50 of KT versus NK: NR50 represents normalization of R50 values of KTs relative to R50 values of contralateral NK calculated as [R50KT− R50NK] / R50NK for each mouse and shown for three mice per group. (E) NR50 of KTSU versus KTCONT: Normalization of R50 values of KTs from mice treated with sunitinib (KTSU) relative to the mean R50 values of KTs from control mice (KTCONT) calculated as [R50 KTSU− R50 KTmean cont] / R50 KTmean cont for each mouse and shown for three mice per treatment group. (F) NR50 of NKSU versus NKCONT: Normalization of R50 values of NKs of mice treated with sunitinib relative to the mean R50 values of NKs from control mice calculated as [R50 NKSU− R50 NKmean cont] / R50 NKmean cont for each mouse and shown for three mice per treatment group. Data are presented for three mice per treatment group from the same experiment shown in Figure 4.1.

4.4.2 DCE-MRI Analysis of Gd Kinetics of Uptake and Clearance Using Parametric Color Maps

The parametric color maps from control mice showed accumulation of Gd in the periphery of the tumor with no uptake in the core of the tumor (Figure 4.3). In the NK of control mice, Gd uptake was distributed in the entire kidney with a higher uptake in the medullary central area than in the peripheral cortex, probably reflecting normal secretion of contrast agent (Figure 4.3). The negative slope image (Nslope) represents the clearance kinetics of Gd and shows low levels in control mice. The kidneys of SU40-treated mice showed a strong accumulation of Gd in most of the KT with persisting high levels in the peak, slope, and washout slope images (Figure 4.3). This effect was also observed in the NK with increased levels of Gd in both cortex and medulla, indicating that this high dosage of sunitinib also alters the perfusion of NK tissue. Parametric color maps of SU20-treatedmice showed a significant accumulation of Gd in the KT including Gd uptake in the tumor (Figure 4.3). These levels were high in the peak, slope, and Nslope images. Similar findings were observed in NK treated with SU20 (Figure 4.3). In contrast, KTs from SU10-treated mice showed no uptake of Gd in the core of the tumor, but some was seen at its periphery similar to KTs from control mice (Figure 4.3). Low levels were observed in the peak, slope, and Nslope images. The NK of mice treated with SU10 showed more Gd in the medulla than in the cortex (Figure 4.3) as seen in NK of control mice. These findings were consistently observed in two additional mice per group.
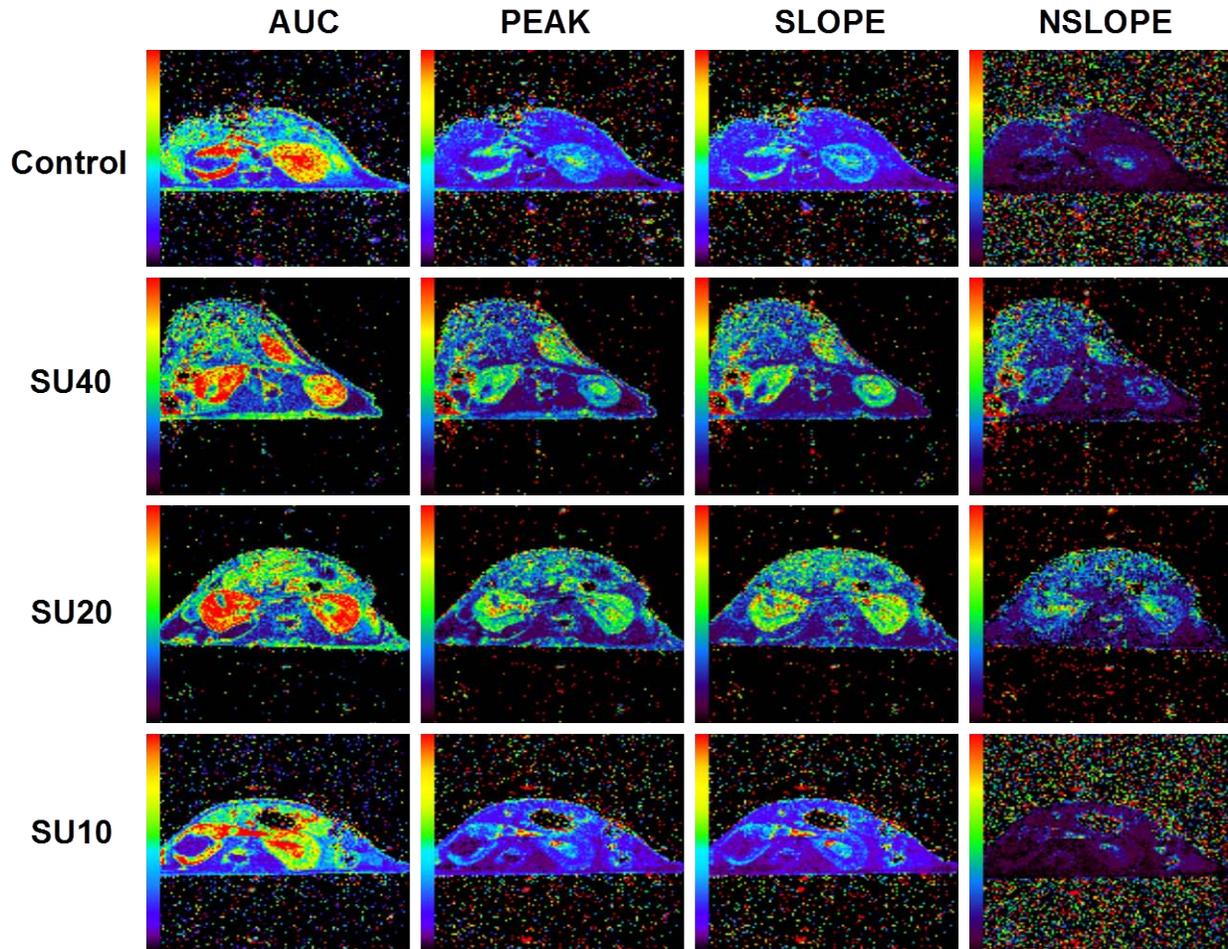
Figure 4.3. DCE-MRI of KTs: Parametric color maps. Parametric color maps were constructed based on uptake and concentration of Gd in the tissue, represented by the colors blue, green, yellow, and red with gradual increase of Gd from lowest values (blue) to highest values (red). Data are presented for the same representative mouse from each treatment group shown in Figure 4.1. The KT is on the left, and the contralateral NK is on the right of the MR images. The color coding in the kidneys are shown for IAUC, the peak, and the slope of C(t). The Nslope represents the clearance of Gd after reaching the peak in the tissue.

4.4.3 Therapeutic Response of KTs to Sunitinib

Previous studies using sunitinib in mouse tumor models have demonstrated that dosages of 40 or 80 mg/kg per day were optimal and biologically active, leading to tumor inhibition and inhibition of phosphorylation of RTKs on cancer cells and endothelial cells (Abrams et al., 2003). Therefore, for our initial studies, we selected to test an optimal dosage of 40 mg/kg per day of sunitinib to investigate the therapeutic response of KTs using our KCI-18 RCC model. After intrarenal injection of KCI-18 cells, by days 10 to 12, mice developed established KTs with a mean (SD) volume of 150 (7) mm^3 and mean (SD) weight of 186 (4) mg compared with NK volume of 125 (2) mm^3 and weight of 148 (12) mg. At that time point, mice were treated daily with 40 mg/kg per day of sunitinib. On day 28 after cell injection, the right KT and the left NK were weighed (Figure 4.4-A). On average, KTs in control animals were 822 mg heavier than the contralateral NK. After sunitinib treatment, KTs were significantly smaller compared with control mice (P =0001; Figure 4.4-A). On average, SU40-treated tumors were 75% smaller than tumors in control mice but were still significantly larger compared with the contralateral NKs, with a mean (SD) difference of 209 (105) mg (P < .0001; Figure 4.4-A, inset). The weight disparity between the tumor-bearing and the NK was significantly smaller in mice treated with SU40 compared with control animals (P = .0002). By gross observation, control mice showed very large and extremely vascularized tumors that invaded the entire kidney and grew into the abdominal cavity (Figure 4.4-A, inset). After sunitinib treatment, the shape of the kidney was preserved in KTs indicating that SU40 therapy controlled the growth and invasion of the tumor through kidney tissue, but the kidneys looked ischemic. DCE-MRI findings suggest that lower doses of sunitinib have a different effect on tumor perfusion; therefore, in additional separate experiments, a dose-response study of sunitinib was tested, and a representative experiment is

presented in Figure 4.4-B. The therapeutic efficacy of lower dosages of 10 or 20 mg/kg per day of sunitinib was evaluated and compared with that of 40 mg/kg per day. SU10 did not significantly control KT growth ($P = .43$); tumors were only 25% smaller than control tumors on average (Figure 4.4-B) and appeared more hemorrhagic by gross observation. Both SU20 and SU40 significantly inhibited KT growth; average growth inhibition was 57% and 66%, respectively, relative to control tumors ($P = .003$ and $P = .0007$, respectively; Figure 4.4-B). On average, tumors of SU20-treated mice were 43% smaller than tumors of SU10-treated mice, but the difference is only marginally significant ($P = .05$). Although the tumors of SU40- treated mice were not significantly smaller than those of SU20-treated mice ($P = .55$), the variation in tumor size from mouse to mouse was smaller in SU40-treated mice (Figure 4.4-B). The extent of tumor growth inhibition mediated by SU40 was comparable in these two series of independent experiments presented in Figure 4.4, A and B, confirming reproducibility of our findings.

A

B
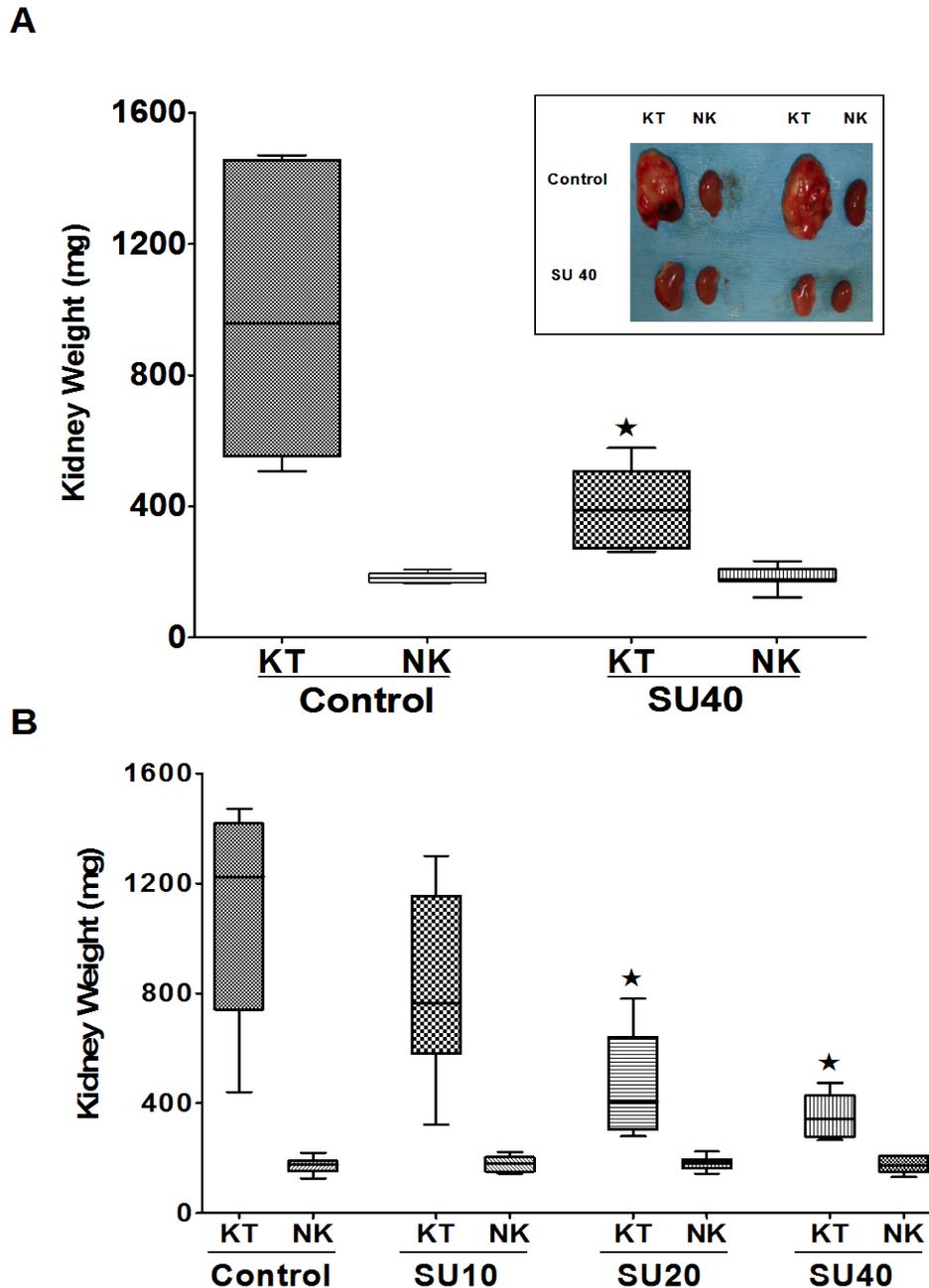
Figure 4.4. KCI-18 KT response to sunitinib. Mice bearing established KTs were treated daily with sunitinib for 18 days, then tumors were resected and weighted. (A) Response to optimal dose of sunitinib. The kidney weights and their median are reported for 10 mice per group treated with vehicle (control) or sunitinib at 40 mg/kg per day (SU40) compared with the contralateral NK weights in each experimental group. Inset contains pictures of KTs of control mice or SU40-treated mice compared with NKs. (B) Sunitinib dose-response. The kidney weights and their median are reported for eight mice per group treated with vehicle (control) or sunitinib at dosages of 40, 20, or 10mg/kg per day (SU40, SU20, or SU10, respectively) compared with the contralateral NK weights in each experimental group. *P < .05. Data presented were obtained from separate representative experiments.

4.4.4 Effect of Sunitinib on the Vasculature of KTs

For histologic studies, KT sections were stained with H&E or by immunostaining with anti-CD31 Ab for the detection of blood vessels. KTs presented as high-grade carcinomas, consisting of tumor cells with large pleomorphic nuclei, prominent nucleoli, abundant eosinophilic cytoplasm, and large cytoplasmic inclusions (Figure 4.5-A, Control) (Hillman et al., 2007). These tumors were highly vascularized with a sinusoidal vascular pattern and abnormal enlarged vessels as seen both by H&E staining and anti- CD31 staining (Figure 4.5, A and B, Control). Tumors treated with SU40 showed areas of tumor destruction and necrosis associated with hemorrhages but also remaining areas of viable tumor cells (Figure 4.5-A). The destruction of tumor vasculature was confirmed by anti-CD31 staining with disruption of the vessel walls, release of red blood cells in the tumor, and minimal staining of endothelial cells by anti-CD31 (Figure 4.5-B). KTs treated with SU20 clearly showed more regularized and thinner vessels by H&E, and staining of endothelial cells in the vessel walls by anti-CD31 (Figure 4.5, A and B) in contrast to the enlarged abnormal vessels observed in KTs from control mice. However, tumors treated with SU10 still contained enlarged abnormal vessels as confirmed by anti-CD31 staining (Figure 4.5, A and B), and some of them were comparable to those observed in control mice.

Kidney Tumor

H&E (A)   Anti-CD31 (B)
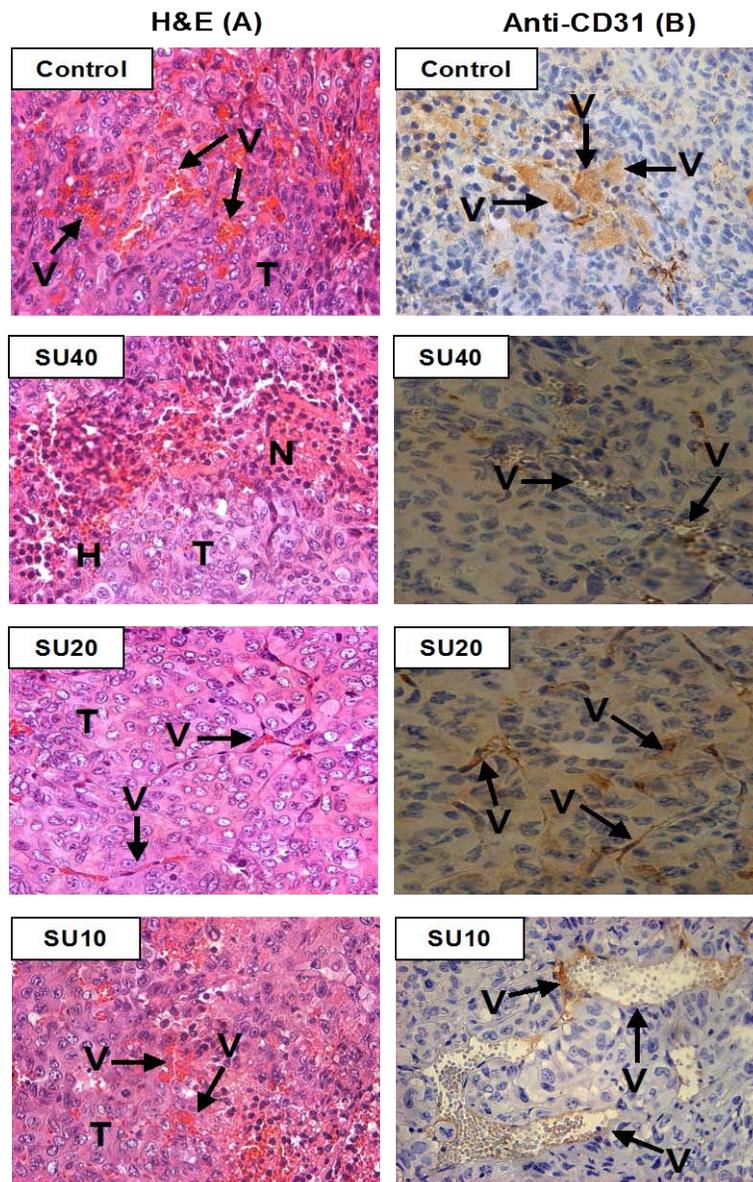
Figure 4.5. Histologic diagnosis of KCI-18 KTs treated with various dosages of sunitinib. KTs resected from mice for the experiments described in Figure 4.4 were processed for histologic diagnosis, and tumor sections were stained either with H&E (A) or with anti-CD31 immunostaining (B). H indicates hemorrhages; N, necrosis; T, tumor; V, vessels. Control untreated tumors consisted of tumor cells with large pleomorphic nuclei and were highly vascularized with a sinusoidal vascular pattern and abnormal enlarged vessels. Tumors treated with SU40 showed areas of tumor destruction and necrosis associated with hemorrhages and areas of viable tumor cells. Tumor sections stained with anti-CD31 reveal destruction of tumor vasculature and disruption of the vessel walls. KTs treated with SU20 showed more regularized and thinner vessels both by H&E and by anti-CD31 staining. SU10-treated tumors show enlarged abnormal vessels as confirmed by anti-CD31 staining with staining of areas of endothelial cells lining vessel walls. Original magnifications, ×40.

4.4.5 Effect of Sunitinib on Vasculature of NK Tissue

Histologic analysis of NKs obtained from control mice showed multiple regular and thin vessels by H&E (Figure 4.6-A) and clear structures of vessels delineated by anti-CD31 staining of endothelial cells in vessel walls (Figure 4.6-B). In contrast, NKs obtained from mice treated with the high SU40 dosage showed dilatation of blood vessels as seen by H&E (Figure 4.6-A). Some enlarged vessels showed disruption of vessel walls as observed by anti-CD31 staining (Figure 4.6-B). The effect of SU20 on normal vessels in NKs was mild and caused dilatation only in a few vessels, whereas most looked normal as seen by anti-CD31 staining, in contrast to the numerous vessels enlarged by SU40 treatment (Figure 4.6, A and B). No effect on vessels in the NK was observed with SU10; the vessels looked thin and regular and were comparable to those seen in NKs of control mice (Figure 4.6, A and B). It should be noted that although disruptions in normal vessels were observed after sunitinib therapy, the mice treated with dosages of 20 to 40 mg/kg per day showed no apparent signs of drug toxicity.

Normal Kidney
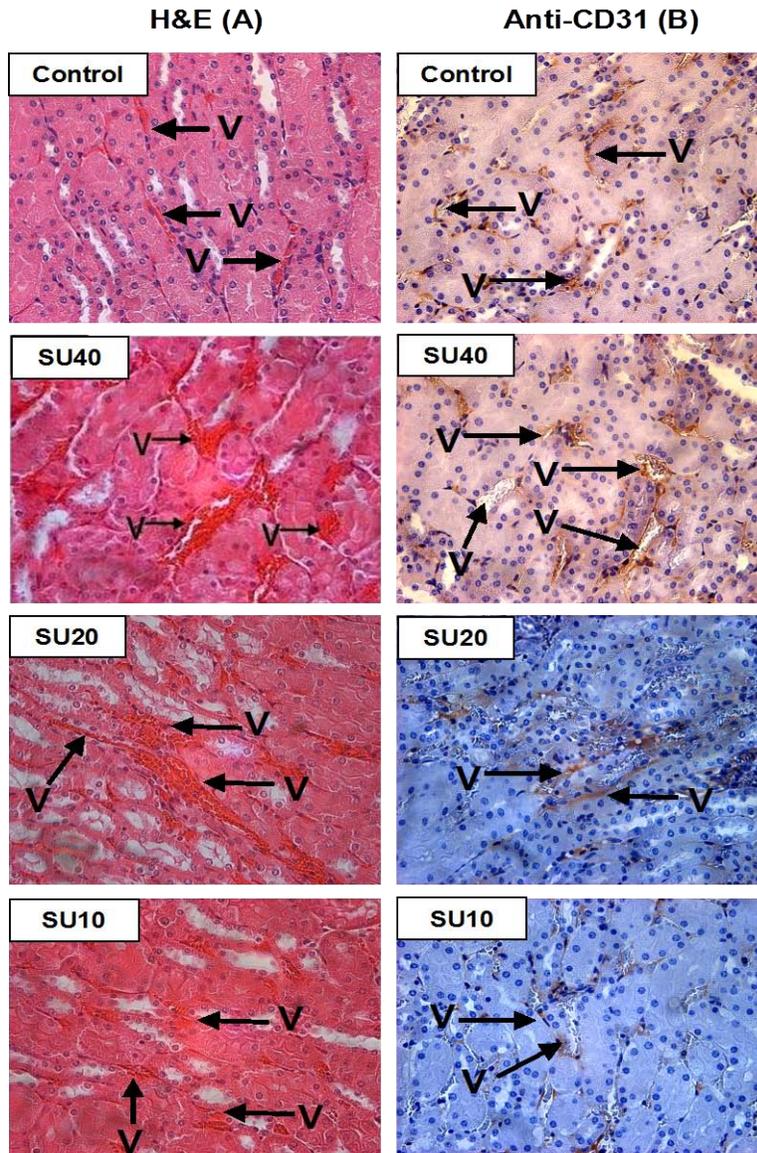
Figure 4.6. Histologic diagnosis of NKs from mice treated with various doses of sunitinib. The contralateral left NKs (not bearing a tumor) resected from mice of the experiments described in Figure 4.4 were processed for histologic diagnosis, and kidney tissue sections were stained either with H&E (A) or with anti-CD31 immunostaining (B).NKs obtained from control mice showed multiple regular and thin vessels (V) by H&E and clear structures of vessels delineated by anti-CD31 staining of endothelial cells in vessel walls. After high SU40 dosage, dilatation of blood vessels was observed as seen by H&E. Enlarged vessels sometimes showed disruption of vessel walls seen by anti-CD31 staining. The milder effect of SU20 on normal vessels in NKs caused dilatation only in a few vessels, whereas most looked normal as seen by anti-CD31 staining. No effect on vessels in the NK was observed with SU10; the vessels looked thin and regular. Original magnifications, ×40.

4.5 Discussion

To design novel targeted therapies for metastatic RCC, extensive research is ongoing to test drugs that target both the tumor cells and the tumor vasculature to inhibit processes that stimulate tumor growth in the tumor microenvironment. Antiangiogenic therapy causing excessive vascular regression could compromise the delivery of drugs or oxygen in the tumor when combined with conventional cytotoxic therapies (Jain, 2001; Jain, 2005). Using a preclinical RCC model, we have investigated, by DCE-MRI, vascular changes in KTs induced by the antiangiogenic drug sunitinib to select doses that could induce transient vessel normalization by pruning inefficient blood vessels and thereby improve tumor blood flow and subsequent drug delivery to tumor cells by chemotherapy (Browder et al., 2000; Wildiers et al., 2003; Tong et al., 2004).

A dose-dependent therapeutic efficacy of sunitinib for KCI-18 RCC tumor xenografts was demonstrated with dosages of 20 and 40 mg/kg per day, causing a significant inhibition/arrest of tumor growth and limited invasion of the kidney by tumor cells, in agreement with previous preclinical animal studies (Abrams et al., 2003; Murray et al., 2003; O'Farrell et al., 2003; Xu et al., 2005). Sunitinib exerted a direct cytotoxic effect at doses greater than 0.5 μM in KCI-18 cells in vitro. As documented in clear cell RCC and papillary RCC human tumor specimens (Lam et al., 2005; Xu et al., 2005), we found that KCI-18 cells and tumors also expressed the VEGFR-2 and PDGFR-β RTKs targets of sunitinib. Increasing doses of sunitinib caused a lower expression of these receptors on KTs, probably due to the modulation of these receptors. These findings suggest that sunitinib could inhibit KCI-18 tumor growth through targeting of RTKs signaling on tumor cells and/or on endothelial cells or stromal cells resulting in direct antitumor and antiangiogenic activities as shown in other studies. Interestingly,

modulation of RTKs receptors by sunitinib was also observed on NK tissues, confirming the effect of the drug on the vasculature of normal tissues. In agreement with our findings, recent animal studies (Ebos et al., 2007) and clinical trials of sunitinib for metastatic RCC or breast cancer reported decreased soluble VEGFRs' plasma levels (Burstein et al., 2008; Rini et al., 2008), which suggested modulation of VEGF pathway biomarkers by sunitinib. Furthermore, previous pharmacokinetic studies in mouse xenograft models demonstrated plasma levels of 50 to 100 ng/ml for 12 hours when mice were treated with the same efficacious dosages of 20 to 40 mg/kg per day of sunitinib as used in our studies, resulting in the inhibition of VEGFR-2 and PDGFR-β RTKs. Comparable plasma levels of 50 to 100 ng/ml of sunitinib were also measured in pharmacokinetic studies of patients receiving 50-mg daily doses (Britten et al., 2008).

Sunitinib also induced dose-dependent vascular changes, which were observed both in KTs and in NK tissues by DCE-MRI. In control mice, the clearance of Gd in the KT was slow compared with faster clearance in the NK, probably as a result of leakiness from the abnormal enlarged tumor vessels observed histologically. Parametric maps from control mice showed accumulation of Gd in the periphery of the tumor with no uptake in the core of the tumor, indicative of poor vascularity and perfusion in the core of the tumor as shown in other MRI studies of xenograft tumors (Checkley et al., 2003; Marzola et al., 2005). In contrast, the NK of control mice showed distribution of Gd in the entire kidney with lower uptake in the peripheral cortex and a higher uptake in the medulla probably due to greater numbers of vessels in that area and reflecting normal secretion of contrast agent. Compared with control tumors, KTs from mice treated with a low dosage of 10 mg/kg per day of sunitinib showed mild changes in Gd uptake and clearance kinetics of KTs. These SU10- treated tumors had also poor tumor perfusion in the core of the tumor and histologically showed enlarged abnormal vessels similar to findings

observed in control tumors. Likewise, SU10 caused minimal effect on NK tissue vasculature with no changes in vascular permeability or vessel morphology compared with control mice.

A therapeutic high dosage of 40 mg/kg per day induced vascular permeability changes resulting in retention of Gd in both left and right kidneys. Gd retention was greater in the KT than in the NK. This increased vascular permeability of Gd in the tumor could be due to the damaged vasculature and leakage of Gd into surrounding kidney tissue with slow kinetics of washout. Histologic studies confirmed destruction of tumor vasculature of SU40-treated KTs and disruption of the vessel walls causing hemorrhages. It should be noted that increased levels of Gd were also observed in both cortex and medulla of NKs, indicating that this high SU40 dosage alters the kinetics of uptake and contrast clearance of NK tissue. These data are supported by histologic observation of dilatation and disruption of normal vessels detected by anti-CD31 Ab staining of NK tissue. We conclude that the dosage of 40 mg/kg per day of sunitinib causes excessive vascular damage and vascular permeability in KTs and alterations of NK vessels. This in turn suggests that this dosage is not appropriate for combination chemotherapies.

After treatment with an intermediate sunitinib dosage of 20 mg/kg per day, improved Gd clearance was observed with less Gd retention than that seen with SU40 or in control mice. Interestingly, in SU20- treated mice, Gd uptake and clearance in the C(t) curves, IAUC, and CIAUC showed identical patterns in the KT compared with the NK as confirmed by the low R50 value of KTs relative to the R50 value of NKs (Figure 4.2-D). A clear shift to the left of IAUC curves of SU20- treated mice was observed compared with control mice and SU40- treated mice as shown also by the low R50 value of KTs treated with SU20 relative to the R50 value of control KTs (Figure 4.2-E). These data suggest a return to more "normal vasculature" with lower permeability (i.e., less leaky vessels) after treatment with SU20. Interestingly, a similar pattern

was observed in NKs of mice treated with sunitinib compared with those of control mice showingNR50 values lower for SU20-treated mice than for SU40-treated mice, indicating a milder effect of SU20 dosage on vasculature of NK tissue (Figure 4.2-F). Parametric maps revealed increased Gd uptake in the core of the tumor and surrounding kidney tissue in SU20-treated mice. Histologically, the vessels of KTs treated with SU20 clearly showed more regularized and thinner vessels, indicating pruning or normalization of tumor vessels compared with the enlarged vessels of control KTs. The effect of SU20 on vessels in NKs was mild and caused dilatation only in a few vessels.

To assess our results statistically, one way ANOVA was performed on the data from Figure 4.2-D to examine the differences in the normalized ratio of the mean value of the CIAUC curve (NR50) between the kidney tumor (KT) and normal kidney (NK) for all mice treated with a dose of 40, 20 or 10 mg/kg/day sunitinib or treated with vehicle only. The subject inclusion criterion for analysis is defined by the changes of R50 values for the kidney tumors relative to R50 values in the normal kidney. There were a total of 12 mice used in the final analysis, 3 per each group. With this sample size, there is only a marginally significant difference between the KT group treated with sunitinib at a dose of 20 mg/kg/day and the control group (F (12, 3) = 1.83, p = 0.058). There was no significant difference between controls and other mice treated with a sunitinib dose at either 10 or 40 mg/kg/day. Clearly an increased sample size might show more significant results. This would be necessary if we have to verify the claim that RCC treatment with an intermediate dose of 20 mg/kg/day sunitinb offers enhancement in kidney tumor perfusion with less impact in the normal kidney over a conventional treatment dose of 40 mg/kg/day sunitinb

In summary, imaging of tumor vasculature changes by DCE-MRI and histologic diagnosis indicates that a lower dosage of 20 mg/kg per day of sunitinib could cause "pruning" or normalization of the tumor vasculature allowing for better tumor perfusion and decreased leakiness of vessels. Moreover, this dosage caused only mild vascular changes in normal tissues and thus could be less toxic to normal vessels, suggesting that this dosage could be used for combination with chemotherapy or radiotherapy.

Our histologically verified studies demonstrate that the use of DCE-MRI is a useful means for monitoring vascular changes induced by sunitinib in both tumors and normal tissues. These data can be used to select the dose and schedule of sunitinib and potentially other antiangiogenic drugs causing transient normalization of tumor vasculature for combination therapies.

Chapter Five

DCE-MRI Imaging of Sunitinib-Induced Vascular Changes to Schedule Chemotherapy in Renal Cell Carcinoma Xenograft Tumors

Gilda G. Hillman[1]*, Vinita Singh-Gupta[1], Areen K. Al-Bashir[2,3], Hao Zhang[1], Christopher K. Yunker[1], Amit Patel[1], Seema Sethi[4], Judith Abrams[5], E. Mark Haacke[2,3].

[1]Department of Radiation Oncology, [2]Department of Radiology, [3]Department of Biomedical Engineering, [4]Department of Pathology and [5]Integrated Biostatistics Unit; Barbara Ann Karmanos Cancer Institute, Wayne State University School of Medicine, Detroit, MI 48201, USA.

*Corresponding Author:

Gilda G. Hillman, Ph.D.
Department of Radiation Oncology
515 Hudson-Webber Cancer Research Center
4100 John R. Road

Detroit, MI 48201, USA
Tel: (313) 576-8257
Fax: (313) 576-8265
E-mail: hillmang@karmanos.org

Running Title: Sunitinib and Gemcitabine for RCC

Keywords: DCE-MRI, imaging, sunitinib, gemcitabine, kidney cancer

64

5.1 Abstract

In an attempt to develop better therapeutic approaches for metastatic renal cell carcinoma (RCC), the combination of the anti-angiogenic drug sunitinib with gemcitabine was studied. Using dynamic contrast-enhanced magnetic resonance imaging (DCE-MRI), we have previously determined that a sunitinib dose of 20mg/kg/day increased kidney tumor perfusion and decreased vascular permeability in a pre-clinical murine RCC model. This sunitinib dose causing regularization of tumor vessels was selected to improve delivery of gemcitabine to the tumor. DCE-MRI was used to monitor regularization of vasculature with sunitinib in kidney tumors to schedule gemcitabine. We established an effective and non-toxic schedule of sunitinib combined with gemcitabine consisting of pre-treatment with sunitinib for 3 days followed by four treatments of gemcitabine at 20mg/kg given 3 days apart while continuing daily sunitinib treatment. This treatment caused significant tumor growth inhibition resulting in small residual tumor nodules exhibiting giant tumor cells with degenerative changes, which were observed both in kidney tumors and spontaneous lung metastases, suggesting a systemic anti-tumor response. The combined therapy caused a significant increase in mouse survival. DCE-MRI monitoring of vascular changes induced by sunitinib, gemcitabine and both combined showed increased tumor perfusion and decreased vascular permeability in kidney tumors. These findings, confirmed histologically by thinning of tumor blood vessels, suggest that both sunitinib and gemcitabine exert anti-angiogenic effects in addition to cytotoxic anti-tumor activity. These studies show that DCE-MRI can be used to select the dose and schedule of anti-angiogenic drugs to schedule chemotherapy and improve its efficacy.

5.2 Introduction

Recent developments in anti-angiogenic therapy have improved targeting metastatic renal cell carcinoma (RCC). The incidence of RCC has increased in recent years with approximately 54,390 new cases each year in the United States of America. The disease is responsible for an estimated 13,010 deaths each year (Jemal et al., 2008). Nearly half of the patients present with localized disease that can be treated by surgical removal (Haas and Hillman, 1996; Motzer et al., 1996). However, one third of the patients have metastatic disease at first presentation, and 20-30% of the patients treated for localized RCC subsequently develop metastatic disease which frequently involves the lungs (Haas and Hillman, 1996; Motzer et al., 1996).

The drug sunitinib (SU11248 or Sutent) is a small molecule receptor tyrosine kinase (RTK) inhibitor that has been approved by the FDA in January 2006 for RCC treatment based on significant responses in multiple metastatic sites and in primary tumors in initial clinical trials for metastatic RCC (Motzer et al., 2006). We and others have demonstrated that sunitinib targets and inhibits signaling of several RTKs including PDGFR, VEGFR, KIT and FLT3 in mouse xenograft models (Hillman et al., 2009). Sunitinib exhibits direct anti-tumor activity by inhibiting RTKs that are expressed by cancer cells and are involved in signaling for cancer cell proliferation (Abrams et al., 2003; Mendel et al., 2003; Murray et al., 2003; O'Farrell et al., 2003; Sohal et al., 2003; Hillman et al., 2009). Sunitinib also exhibits anti-angiogenic activity by inhibition of signaling through VEGFR-2 and PDGFR-β RTKs expressed on endothelial cells or stromal cells (Mendel et al., 2003; Huang et al., 2010).

In a phase III multinational study of 750 patients with metastatic RCC, randomized to sunitinib or interferon alfa (IFNα), the response rate to sunitinib was 31%, with median progression free survival (PFS) of 11.7 months and a median survival of 28 months (Motzer et

al., 2007). A recent update of this trial documented an objective response rate (ORR) of 47% with 11 months median PFS for sunitinib vs 12% ORR and 5 months PFS for IFNα (Motzer et al., 2009). Although the results with sunitinib therapy are impressive, long-term control of the disease is still not achieved. Additionally, several trials documented adverse effects of cardiotoxicity in some of the patients, probably as a result of alterations to normal vasculature (Chu et al., 2007; Kollmannsberger et al., 2007; Schmidinger et al., 2008; Telli et al., 2008). Therefore, further investigations with sunitinib dose adjustments and combination with other cytotoxic drugs are warranted to decrease the impact on vital organs such as the heart and the kidney.

The process of tumor angiogenesis involves proliferation of abnormal vessels that are enlarged, disorganized and leaky due to defective basement membrane. These structural defects of tumor vessels cause increased interstitial tissue pressure, impaired blood supply and decreased oxygen supply in tumors compromising the delivery and efficacy of cytotoxic drugs and radiotherapy (Jain, 2001; Jain, 2005). To increase the efficacy of chemotherapy, we have recently investigated various doses of sunitinib to cause only partial destruction of immature and inefficient blood vessels leading to "normalization" of tumor vasculature and improve the blood flow in tumors (Hillman et al., 2009). We used dynamic contrast-enhanced magnetic resonance imaging (DCE-MRI) to image vascular changes induced by sunitinib within the tumor, in an orthotopic KCI-18 model of human RCC xenografts in nude mice. DCE-MRI is a non-invasive approach, currently used in humans, that can detect early changes in the tumor induced by anti-angiogenic therapy as reported in human studies (Yankeelov et al., 2007; Hahn et al., 2008) and in preclinical animal models (Checkley et al., 2003; Marzola et al., 2005). This method measures a combination of tumor perfusion and vessel permeability and allows the detection of changes in

tumor vascularity, which occur at a much earlier stage in the treatment of tumors with anti-angiogenic drugs than does shrinkage of tumor mass.

By assessing vascular changes by DCE-MRI, we showed that a suboptimal daily sunitinib dose of 20mg/kg/day mildly affected normal vessels but caused better tumor perfusion and decreased vascular permeability, in agreement with histological observations of thinning and regularization of tumor vessels (Hillman et al., 2009). The goals of the current study were to determine if using sunitinib at doses which regularize the blood flow in the tumor in conjunction with the cytotoxic drug gemcitabine could improve its therapeutic efficacy for RCC. Gemcitabine is a pyrimidine analogue that inhibits DNA synthesis. The antitumor activity of gemcitabine depends on a series of sequential phosphorylations leading to accumulation of gemcitabine diphosphate and triphosphate which interfere with DNA elongation by competing with dCTP and also inhibit ribonucleotide reductase, thus reducing the pool of deoxyribonucleotide triphosphates. A few clinical trials have used gemcitabine in combination with other chemotherapy drugs including fluorouracil, thalidomide and capecitabine or with the cytokine interferon alpha for metastatic renal cell carcinoma (Desai et al., 2002; Perez-Zincer et al., 2002; Amato and Khan, 2008; Tannir et al., 2008). These trials resulted in modest clinical benefit.

Although gemcitabine is a potent anti-tumor drug, its activity may be reduced by poor access to tumor cells caused by tumor vessel leakiness and increased interstitial tissue pressure (Jain, 2001; Jain, 2005). In the current study, we have investigated whether improving blood flow by sunitinib, at doses which regularize tumor vessels, could enhance the efficacy of gemcitabine for RCC in murine xenografts kidney tumors. DCE-MRI was used to monitor vascular changes induced by pre-treatment with sunitinib in KCI-18 kidney tumors to schedule

initiation of chemotherapy. We determined the dose and schedule of the combination of anti-angiogenic therapy with sunitinib and cytotoxic therapy with gemcitabine that result in significant long lasting anti-tumor response. Vascular changes caused by gemcitabine treatment as a single modality or combined with sunitinib were evaluated by DCE-MRI.

5.3 Materials and Methods

5.3.1 Orthotopic KCI-18/IK RCC Tumor Model

The human RCC cell line designated KCI-18 was established in our laboratory from a primary renal tumor specimen obtained from a patient with papillary RCC (nuclear grade III/IV) (Hillman et al., 2004). Cells were cultured in DMEM medium with supplements (Hillman et al., 2004). Following serial passages of KCI-18 cells in the kidney of nude mice, highly tumorigenic KCI-18/IK RCC cell lines were generated (Hillman et al., 2004). KCI-18/IK cells were washed with HBSS and subcapsularly injected at a concentration of 5×10^5 cells in 30 µl HBSS in the right kidney in 5-6 week old female BALB/C *nu/nu* nude mice (Harlan, Indianapolis, IN) (Hillman et al., 2004). Mice were housed and handled under sterile conditions in facilities accredited by the American Association for the Accreditation of Laboratory Animal Care. The animal protocol was approved by Wayne State University Animal Investigation Committee.

5.3.2 Experimental Protocol

After injection of KCI-18/IK cells, a few mice were sacrificed at early time points to assess tumor growth before initiating treatment. Small tumors were detectable by day 9-10 in the kidney. On day 10, mice bearing established kidney tumors were treated with sunitinib (Pfizer Inc, New York, NY). The drug was prepared in a carboxymethyl cellulose suspension vehicle, at a dose of 20 mg/kg/day (SU20) and given orally by gavage, once a day (Hillman et al., 2009). Control mice were treated with vehicle only. After sunitinib pre-treatment for 3 days, mice were treated with various doses of gemcitabine administered 2-3 times a week by intraperitoneal (i.p.) injections. Gemcitabine (Gemzar, from Eli Lilly, Indianapolis, IN) was reconstituted in PBS and prepared at doses of 10-50mg/kg. Sunitinib treatment was continued daily for the duration of the

experiment. To assess the therapeutic response of kidney tumors to a combination of sunitinib and gemcitabine, 6-8 mice per experimental group were treated. Mice were killed by day 28 after tumor cell injection, when the tumor burden in control animals was large (greater than 1.5cm x 1cm in size compared to 0.7cm x 0.25cm for normal kidney) to compare with tumor sizes in treated groups (Hillman et al., 2009). The tumor-bearing right kidneys and the contralateral left normal kidneys were resected and weighed (Hillman et al., 2009). For survival studies, 12 mice per experimental group were treated with sunitinib at 20mg/kg/day for 3 days on day 10-12 after KCI-18 cell injection in the kidney. Then, mice received five gemcitabine treatments at 20 mg/kg given 3-4 days apart, on days 13, 16, 20, 23 and 27. Sunitinib was continued daily for five days a week, for 6 weeks, up to 50 days. Mice were monitored daily for survival and sick animals were killed and autopsied (Haacke et al., 2007). On day 50, all remaining mice were killed and tumor-bearing kidneys were resected and weighted.

5.3.3 Tissue Preparation for Histology

At completion of experiments, mice were killed and tumor-bearing kidneys, normal contralateral kidneys and the lungs were resected and processed for histology. All tissues were fixed in 10% buffered formalin, embedded in paraffin and sectioned (Hillman et al., 2009). Sections were stained with hematoxylin-eosin (H&E) (Hillman et al., 2009).

5.3.4 DCE-MRI Monitoring of Tumor Perfusion and Permeability and Tumor Size in Kidney Tumors

Based on initial experiments, early time points between 3 and 11 days after initiation of sunitinib treatment (day 14 through day 21 post tumor cell implantation) were selected for DCE-

MRI studies to avoid incorrect analysis of advanced and large necrotic tumors in control mice. Three mice from control, sunitinib and gemcitabine treated groups were imaged by DCE-MRI. Mice were anesthetized by i.p. injections of 0.35 ml pentobarbital and 0.35ml ketamine at a concentration of 52.5mg/kg then a catheter was inserted into their tail vein, which was attached to a syringe containing Gd-DTPA contrast agent (Berlex, Wayne, NJ). Mice were positioned on a cradle heated by temperature-controlled water and were given a second low dose of 15mg/kg anesthetics (in 0.1ml volume) to avoid motion problems while in the magnet (Hillman et al., 2009). A 2-cm diameter receive-only surface coil was placed over the tumor and the cradle was placed inside an 11-cm inner diameter transmit-only volume coil. DCE-MRI of mice was performed in the MR Research Facility at Wayne State University, using a Bruker Biospec AVANCE animal scanner equipped with a 4.7 –T horizontal bore magnet and actively shielded gradients. Anatomical imaging was done using a 2D T2 weighted spin echo scan (TR = 2000ms, TE = 52.4ms) to get an overview of the kidney (Hillman et al., 2009). Baseline imaging data of the kidneys were obtained using the short TR DCE scan for 30 time points (7 sec between time points). On time point 10, 100 µl of Gd-DTPA (0.125 mmole/kg) was injected into the tail vein catheter. This dose was selected based on preliminary Gd dose searching experiments to obtain appropriate contrast for image analysis (Hillman et al., 2009). Then, imaging data were acquired for 20 more time points. The imaging parameters for this multi-slice 2D gradient echo scan were: TR = 54.7ms, TE = 2.9ms, FA = 30°, FOV= 32mm x 32mm, slice thickness = 1.5mm with 0.5mm gap, matrix size = 128x128. Five slices were collected for each animal. Data were processed to determine changes in contrast agent uptake using the SPIN DCE software (Detroit, MI) (Haacke et al., 2007). For data analysis, the full kidney was selected as the region of interest (ROI) for the tumor-bearing kidney and the contralateral left normal kidney. A threshold was

selected to remove noise only pixels in the image (Hillman et al., 2009). Gd concentrations [C(t)] in the tissue were calculated for all pixels in the ROI and for each time point (Raffoul et al., 2007). Data from the C(t) curves were compiled for each pixel for 16 time points (112sec) after Gd injection to create the initial area under the curve (IAUC). The distribution of IAUC for the entire ROI is then shown as a means to visualize the effects in every pixel in a single plot. The CIAUC is the cumulative initial area under the curve of the IAUC histogram (Hillman et al., 2009). For quantitative analysis of vascular permeability, R50 (median) values are derived from CIAUC curves and correspond to the concentration of Gd at which 50% of the pixels have been included (Raffoul et al., 2007). To evaluate the uptake, wash-out and leakage of Gd into the tumor and surrounding kidney tissue, the parametric color maps are used to show the total Gd uptake (AUC) in individual structures. The parameters measured in DCE-MRI for sunitinib and or gemcitabine treated tumors were compared to those obtained for control tumors and normal kidneys.

5.3.5 Statistical Analysis

Evaluation of the shape of the frequency distribution of tumor weights indicated that a log transformation was required to meet the assumptions of normal theory tests. Linear models were used to assess the statistical significance of differences in tumor weight between experimental groups and proportional hazards models were used for survival data. In both models, indicator variables were used parameterize dose. Adjustment for multiple comparisons between treatments was made using Holm's procedure to protect against inflated type I errors. Kaplan-Meier methods were used to graphically compare survival in each of the groups. The

log-rank test was used to test differences in survival distributions between groups again using

Holm's procedure to control for type I error rate.

5.4 Results

5.4.1 Direct Cytotoxic Effect of Sunitinib Combined With Gemcitabine in KCI-18 Cells in Vitro

We have previously shown that sunitinib exerts a direct cytotoxic effect on KCI-18 RCC *in vitro*, in a dose-dependent manner (Hillman et al., 2009). We found that a dose of 1 µM sunitinib caused a significant 40% inhibition in cell survival in a clonogenic assay, as confirmed in this additional experiment (Table 5.1). This dose was selected to investigate whether this effect is enhanced by the addition of gemcitabine. Following pilot titration experiments, suboptimal doses of gemcitabine were tested alone and combined with sunitinib in a clonogenic assay. Gemcitabine at doses of 1 and 2.5 µM caused significant inhibition of KCI-18 cell survival of about 50% (p<0.001) and 70% (p<0.0001) respectively, compared to control cells treated with vehicle (Table 1). This cell growth inhibition was significantly enhanced to 80% and 90% by co-treatment of 1 µM sunitinib with 1 µM and 2.5 µM gemcitabine, compared to gemcitabine alone (p<0.01) and sunitinib alone (p<0.01) and to control cells (p<0.0001) (Table 5.1).

Treatment	Survival Fraction (Mean ± S.D.)	% Inhibition
Control	1.00	0
Gemcitabine (1 nM)	*0.52 ± 0.04	48
Gemcitabine (2.5 nM)	*0.21 ± 0.01	79
Sutent (1 µM)	*0.64 ± 0.02	36
Gemcitabine (1 nM) + Sutent (1 nM)	**0.19 ± 0.01	81
Gemcitabine (2.5 nM) + Sutent (2.5 µM)	**0.07 ± 0.02	93

Table 5.1: Inhibition of KCI-18 cell growth by sunitinib combined with gemcitabine *in vitro*. KCI 18 cells were treated with gemcitabine at 1nM and 2.5 nM or sunitinib at 1 µM, or both drugs in combination for 24 hrs, and then cells were plated in a colony formation assay for 10 days. The mean survival fraction was calculated from triplicate wells. *p<0.001;**p<0.0001.

5.4.2 Therapeutic Response of Kidney Tumors by Combined Sunitinib and Gemcitabine in Vivo

Using DCE-MRI and histological studies, we have previously demonstrated that sunitinib, given at a dose of 20mg/kg/day for 7 days, caused trimming and regularization of tumor vessels with improved tumor perfusion (Hillman et al., 2009). This dose was therefore selected for combination with chemotherapy. To schedule administration of gemcitabine mice, which had established kidney tumors [150 mm^3 (SD 7), 186 mg (SD 4)] compared to normal kidney sizes [125 mm^3 (SD 2), 148 mg (SD 12)] on day 10 after tumor implantation, were treated daily with sunitinib at 20mg/kg/day (SU20) for 3 days and then imaged by DCE-MRI (Figure 5.1 A). As observed in our previous studies, the IAUC distribution pattern of Gd uptake and clearance in control mice was different for kidney tumors than for normal kidneys (Hillman et al., 2009). Slower clearance of Gd was observed in the tumor-bearing kidney compared to faster clearance in the normal kidney and the CIAUC curve for the tumor-bearing kidney showed a pronounced shift to the right compared to normal kidney, indicative of a greater retention of Gd (Figure 5.1A). In contrast, treatment with SU20 for 3 days showed identical patterns of Gd uptake and clearance in the kidney tumor than in the normal kidney, as previously shown (Hillman et al., 2009). IAUC and CIAUC histograms of the kidney tumor overlapped those of the normal kidney and shifted to the left compared to control tumor kidneys, indicating decreased Gd retention and improved tumor perfusion (Figure 5.1A). Based on these data showing that vascular regularization is detectable by DCE-MRI after 3 days of daily treatment with SU20, we designed the treatment schedule for combination therapy with gemcitabine as presented in Figure 5.1B. Gemcitabine treatment was initiated at 3 days after pre-treatment with SU20 for established KCI-18 kidney tumors. The schedule and dose of gemcitabine treatment

were determined based on dose titration experiments. Following 3-5 injections of gemcitabine at the dose of 50mg/kg, given two days apart together with daily SU20, a complete tumor growth inhibition was observed, but this treatment was too toxic to the mice resulting in 50% death. Therefore, we tested lower doses of 10, 20 and 40 mg/kg of gemcitabine (G10, G20, G40) given twice a week, 3 days apart while SU20 was continued daily for the duration of the experiment (Figure 5.1B). In separate experimental groups of 6-8 mice per group, the response to gemcitabine treatment alone was compared to SU20 alone and both combined in a relatively short-term experiment of 28 days, to compare tumor size at a time point when control tumors are very large. The tumor-bearing right kidney and the normal left kidney were weighed and the mean tumor weights were compared between each treatment group and control group (Figure 5.1C). Following SU20 treatment alone, kidney tumors were significantly smaller by 43% compared to control mice tumors ($p= 0.001$); but these tumors were still large (Figure 5.1C), as previously reported (Hillman et al., 2009). Compared to control, treatment with G10 caused about 30% inhibition ($p=0.04$) and increased to 52.5% when combined with SU20 ($p<0.001$). The effect of G20 was even greater causing 64% tumor growth inhibition ($p<0.001$) and 74% when combined with SU20 ($p<0.001$) (Figure 5.1C). Although the difference in the mean tumor weight of G20 + SU20 was not significant compared to G20 ($p=0.33$), the tumor weight data (n=8) in the combined treatment was more consistent and less variable than with G20 only. The average weight of tumor-bearing kidneys of mice treated with SU20 + G20 was only 223mg (SD 37) and their shape and size consistently looked closer to those of normal kidneys (166 mg, SD 22) with a mean difference of only 57 mg (Figure 5.1C). This combined therapy using 20mg/kg/day of sunitinib combined with four treatments of gemcitabine at 20mg/kg given 3 days apart, for a total of 80mg/kg did not cause any signs of toxicity to the mice. However, when the

dose of gemcitabine was increased to 40mg/kg, for a total of 160 mg alone or together with SU20, it was associated with toxicity and weight loss. Treatment with G40 resulted in significant tumor growth inhibition of 71% (p<0.001) when given alone but no further increase was observed with combination with SU20 compared to G40 alone (p=0.53) (Figure 5.1C). The difference between the G20 and G40 groups was not statistically significant (p=0.51). It should be noted that the size of the normal contra-lateral kidneys was not affected by the single or combined therapy at every dose of gemcitabine tested (Figure 5.1C, inset).
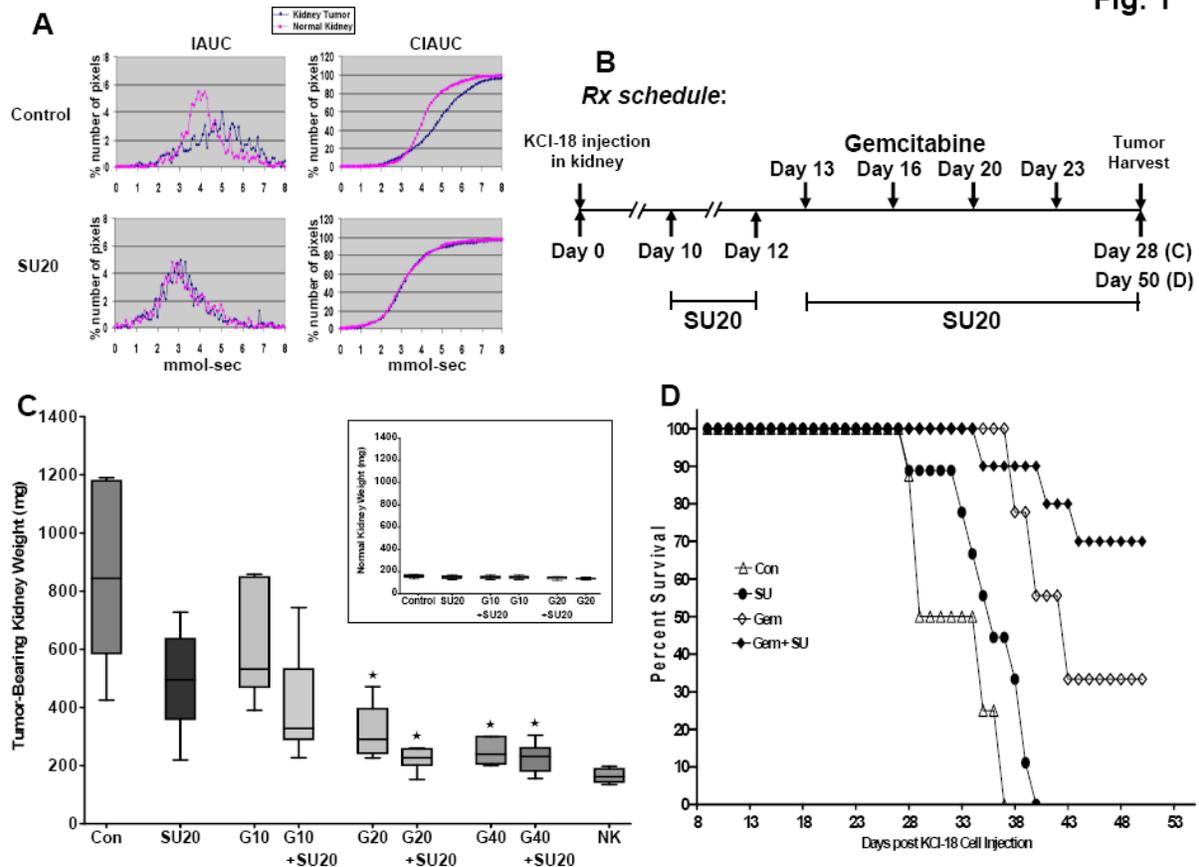
Figure 5.1: KCI-18 kidney tumor response to sunitinib combined with gemcitabine. (A) *DCE-MRI of early vascular changes induced by sunitinib.* Mice bearing established kidney tumors were treated daily with sunitinib at 20mg/kg/day (SU20) for 3 days and imaged by DCE-MRI. (B) *Treatment schedule for combination therapy.* Mice bearing established kidney tumors were pre-treated with sunitinib at 20mg/kg/day (SU20) for 3 days on day 10-12 after KCI-18 cell injection in the kidney. Then, mice received gemcitabine treatments at 10, 20 or 40 mg/kg given 3 days apart, twice a week for 2 weeks on days 13, 16, 20 and 23. Sunitinib was continued daily for up to 28 days for a short-term experiment (2C) or for 50 days for a longer-term experiment (2D). (C) *Response of tumor-bearing kidneys to single and combined therapy.* On day 28, tumor-bearing kidneys and contralateral normal kidneys were resected and weighted. The weights of the tumor-bearing kidneys and their median are reported for 6-8 mice per group treated with vehicle (control) or sunitinib at 20mg/kg/day (SU20), or gemcitabine at 10 (G10), 20 (G20) or 40 (G40) mg/kg; each drug alone and in combination compared to the normal contralateral kidney weights (NK). Inset shows weights of the normal contralateral kidneys for each treatment group. *p<0.001. (D) *Survival of KCI-18 kidney tumor-bearing mice treated with sunitinib combined with gemcitabine.* Mice bearing established kidney tumors were pre-treated with sunitinib (SU) at 20mg/kg/day for 3 days on day 10-12 after KCI-18 cell injection in the kidney. Then, mice received five gemcitabine (Gem) treatments at 20 mg/kg given 3-4 days apart, over 3 weeks on days 13, 16, 20, 23 and 27 and sunitinib was continued daily, 5 days per week, for up to 50 days as shown in Figure 5.2B. Mice were followed survival and Kaplan-Meier survival curves of mice treated with vehicle (Con for control) sunitinib (SU) or gemcitabine (Gem) or both combined (Gem+SU) were constructed.

5.4.3 Survival of Kidney Tumor-Bearing Mice Treated with Combined Sunitinib and Gemcitabine

From the experiments presented in Figure 5.1, we have determined the sequence, schedule and doses for a safe and therapeutic combination of sunitinib and gemcitabine for treating KCI-18 kidney tumor-bearing mice. We showed that a dose of sunitinib of 20mg/kg/day combined with gemcitabine at 20mg/kg/treatment for 4 treatments result in optimal and consistent tumor growth inhibition, when this effect was assessed on day 28 after tumor implantation (Figure 5.1C). These conditions were selected to evaluate the effect of single and combined therapies on mouse survival during a longer term experiment of 50 days. Mice bearing established kidney tumors were pre-treated with 20mg/kg/day sunitinib for 3 days (day 10-12) followed by four injections of gemcitabine at 20mg/kg given 3 days apart (days 13,16,20, 23) following the same schedule shown in Figure 5.1B. An additional gemcitabine injection was administred on day 23 because of the longer duration of the experiment. Sunitinib was continued daily for 5 days a week for 6 weeks, up to day 50 (Figure 5.1B). Mice were monitored on a daily basis and sick mice showing weight loss and/or limited mobility, as a result of large kidney tumors, were euthanized, necropsied and the tumor weights were measured. Survival of animals receiving sunitinib alone was not statistically different from control mice (p=0.08; median SU = 36 days; median controls = 29 days) (Figure 5.1D). In both groups, mice had large kidney tumors at necropsy, the mean tumor weights of control mice was 1157 mg (SD 426) and that of sunitinib treated mice was 675 (SD 226). Animals treated with gemcitabine alone for a total dose of 100mg/kg had median survival of 43 days, significantly longer survival than controls (p<0.001) and than the sunitinib group (p=0.009) but only 33% of the mice survived up to day 50. These mice had large tumors with mean weight of 794 mg (SD 338) when necropsied. The

combination of sunitinib and gemcitabine resulted in longer survival compared to control mice (p<0.001) and mice treated with sunitinib (p<0.001) but not significantly different from animals treated with gemcitabine alone (p=0.13) (Figure 5.1D). Nevertheless, a higher proportion of 70% of the mice (7/10) treated with the combined therapy survived by day 50 compared to 33% with gemcitabine alone and 0% with sunitinib alone. Interestingly, these mice had large tumors with a mean of 767 mg (SD 267), probably due to regrowth of kidney tumors which was not controlled by maintenance therapy with sunitinib at 20mg/kg/day.

5.4.4 In situ Effects of Sunitinib and Gemcitabine on Kidney Tumors and Lung Metastases

Tumor-bearing kidneys and normal contralateral kidneys from mice treated with sunitinib at 20mg/kg/day, gemcitabine at 20mg/kg and both combined were obtained on day 28 from experiments described in Figure 5.1B, C. These tissues were processed for histology and H&E staining. Kidney tumors from control mice presented as a high grade carcinoma, consisting of tumor cells with large pleomorphic nuclei, prominent nucleoli, abundant eosinophilic cytoplasm and large cytoplasmic inclusions (Hillman et al., 2004; Hillman et al., 2009). These tumors were highly vascularized with a sinusoidal vascular pattern consisting of abnormal enlarged vessels (Figure 5.2A). Focal extravasation of red blood cells (RBC) between tumor cells was observed probably due to leakiness of vessels and disrupted basement membrane as previously reported (Hillman et al., 2004; Hillman et al., 2009). Kidney tumors treated with sunitinib showed considerable thinning, regularization and organization of tumor vessels with endothelial cells lining the vessels (Figure 5.2A). A marked decrease in the number of tumor vessels was noted (Figure 5.2A). These findings are consistent with our previous observations (Hillman et al., 2009). Kidney tumors of mice treated with gemcitabine showed abnormal giant tumor cells

exhibiting degenerative changes in their cytoplasm and nuclei, which were indicative of cell death (Figure 5.2A). These giant cells, comprising about 70% of the tumor, contained cytoplasmic vacuoles and pink eosinophilic inclusions and showed degenerative changes in nuclei with focal karyopyknosis (Figure 5.2A). Compared to control tumors, the vascularity of these gemcitabine-treated tumors was reduced and had lower numbers of enlarged vessels. A few focal enlarged vessels were still observed along with few foci of RBC's extravasation (Figure 5.2A). Kidney tumors treated with sunitinib and gemcitabine showed a higher frequency of about 90% abnormal giant tumor cells harboring the same cytoplasmic and nucleus degenerative changes as those seen in gemcitabine alone (Figure 5.2A). The tumor vessels looked more trimmed and more organized than those seen after gemcitabine treatment alone although focal dilatation was still observed compared to sunitinib treated tumors. In lower magnifications, these tumors looked like residual small nodules mostly consisting of giant tumor cells, which were surrounded by normal epithelial renal cells (data not shown). The histology of tumors treated with 40mg/kg of gemcitabine alone or with sunitinib was comparable to that shown in Figure 5.2A for tumors treated with 20mg/kg gemcitabine.

Tissue sections from the normal contralateral left kidneys (not implanted with tumor) were also evaluated after single and combined sunitinib and gemcitabine treatments (Figure 5.2B). Normal kidneys from untreated control mice showed preserved kidney tissue architecture with intact and regular blood vessels. As observed previously, sunitinib at 20 mg/kg/day caused mild dilatation of a few vessels (Hillman et al., 2009). Interestingly, gemcitabine caused dilatation of some of the vessels and mild focal extravasation of RBCs (Figure 5.2B). Following combined sunitinib and gemcitabine treatment, focal areas of dilated vessels were seen but at a lower frequency than with gemcitabine alone (Figure 5.2B).
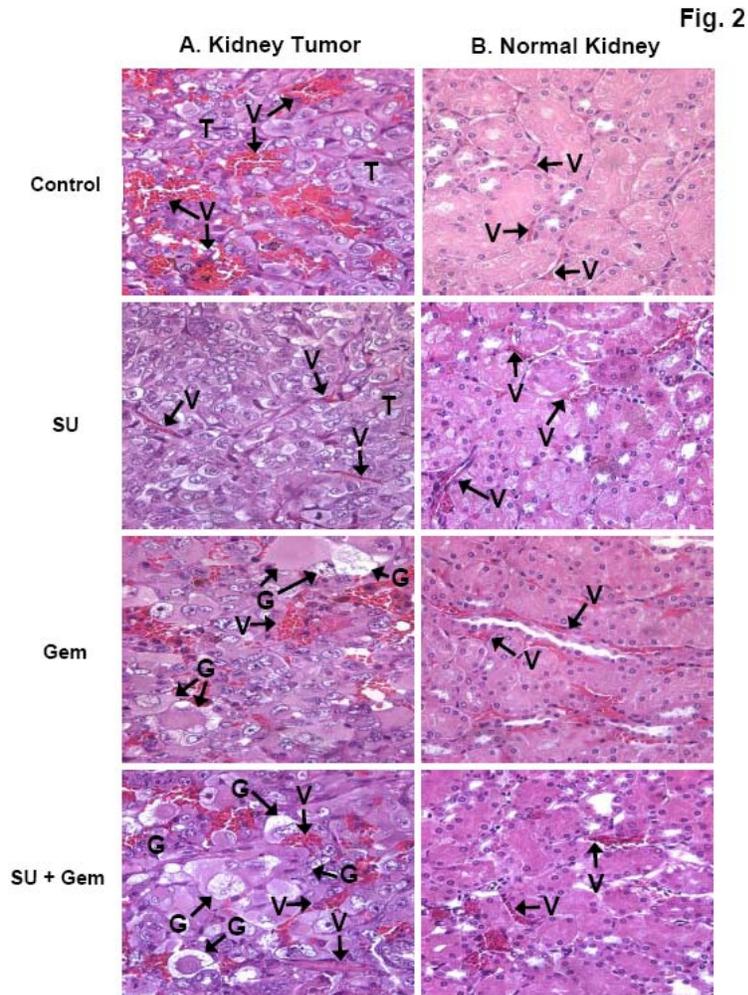
Figure 5.2: Histology of kidney tumors and normal kidneys from mice treated with sunitinib and gemcitabine. Kidney tumors and normal contralateral kidneys from mice treated with sunitinib (20mg/kg), gemcitabine (20mg/kg) and both combined, obtained on day 28 from experiments described in Figure 5.1, were processed for histology and H&E staining. The main findings were labeled on the prints with T for tumor, V for vessels, G for giant tumor cells. (A) *Kidney tumors.* Control untreated tumors consisted of tumor cells with large pleomorphic nuclei, were highly vascularized with a sinusoidal vascular pattern of abnormal enlarged dilated vessels with focal extravasation of RBCs. Sunitinib (SU) treated tumors showed thinning and organization of tumor vessels as well as a decrease in the numbers of tumor vessels. Kidney tumors of mice treated with gemcitabine (Gem) contain numerous abnormal and giant tumor cells with cytoplasmic vacuoles or eosinophilic inclusions and degenerative changes in nuclei with focal karyopyknosis. Note some of the vessels in these tumors were still enlarged with foci of RBCs extravasation; however to a lesser degree than in the untreated tumors. Tumors treated with sunitinib and gemcitabine (SU + Gem) consisted mostly of abnormal degenerating giant tumor cells. Trimming of tumor vessels was evident. (B) *Normal contralateral left kidneys.* The normal kidney from control mice showed intact, regular and thin blood vessels. Sunitinib at 20mg/kg showed a mild effect of dilatation in a few vessels. Gemcitabine caused dilatation of some of the blood vessels. This effect was milder with combined sunitinib and gemcitabine with fewer vessels dilated. All magnifications X40.

Spontaneous metastasis to the lungs from primary KCI-18 kidney tumors has been previously observed in this RCC metastatic model (Hillman et al., 2004). To assess the effect of therapy on spontaneous lung metastases, lungs were resected on day 28 from kidney tumor-bearing mice treated with sunitinib and gemcitabine and processed for H&E staining. In control kidney-tumor bearing mice, all mice presented with metastatic lung tumor nodules showing the typical morphology of KCI-18 RCC tumor cells with large pleomorphic nuclei and prominent nucleoli (Figure 5.3). Areas of dilated vessels with extravasation of RBC's were observed as seen in primary kidney tumors (Figure 5.3). The average number of lung nodules was 26 per mouse consisting of a mixture of large and small nodules. In sunitinib-treated mice, all mice had metastatic lung nodules but the majority of the nodules were very small often containing less than 10 cells per nodule and an average of 14 per mouse. The lung tumor nodules showed an overall decrease in the number of tumor cells and/or areas of tumor destruction as well as a marked decrease in vascularization (Figure 5.3). Mice treated with 20 or 40 mg of gemcitabine had a lower frequency of lung nodules detectable in 3 out of 7 mice and presenting as 1-5 small lung nodules per mouse. These lung tumor nodules exhibited giant tumor cells with cytoplasmic vacuoles, eosinophilic inclusions and degenerative nuclei identical to those observed in primary kidney tumors treated with gemcitabine (Figure 5.3). Few trimmed vessels were seen. The effect of combined sunitinib and gemcitabine on metastatic lung nodules was more drastic with large areas of hyalinization and fibrosis and few remaining giant tumor cells with degenerative changes (Figure 5.3). Lung tumor nodules were detectable only in 3 out of 11 mice treated with sunitinib combined with 20 or 40 mg/kg gemcitabine and the majority of these nodules were very small often containing less than 5 cells per nodule and large areas of fibrosis.
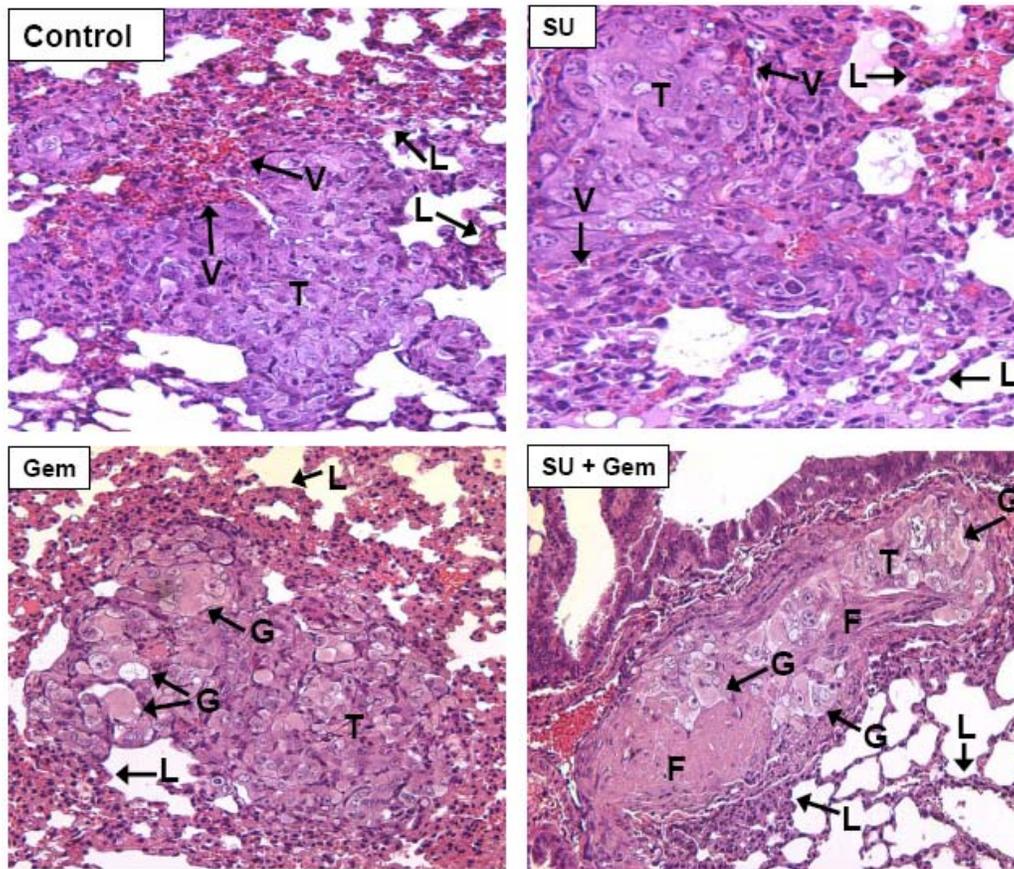
Figure 5.3: Histology of spontaneous lung metastases from mice treated with sunitinib and gemcitabine. Lungs from mice treated with sunitinib (20mg/kg), gemcitabine (20mg/kg) and both combined, obtained on day 28 from experiments described in Figure 5.1, were processed for histology and H&E staining. The main findings were labeled on the prints with T for tumor, V for vessels, G for giant tumor cells, F for fibrotic areas and L for normal lung alveoli. Metastastic lung tumor nodules from untreated mice (Control) consisted of tumor cells with pleomorphic nuclei and prominent nucleoli and contained areas of dilated vessels. Sunitinib (SU) –treated mice had decreased number of tumor cells and vessels in lung tumor nodules. Lung tumor nodules from gemcitabine (Gem) treated mice showed giant tumor cells with cytoplasmic vacuoles and eosinophilic inclusions and decreased vascularization. Gemcitabine combined with sunitinib (SU + Gem) contained large eosinophilic areas of hyalinization, fibrosis and a few giant abnormal tumor cells. Figures were enlarged to show changes in lung tumor nodules.

5.4.5 DCE-MRI Evaluation of Vascular Changes Induced by Gemcitabine Treatment in Kidney Tumors

To monitor the effect of gemcitabine treatment by DCE-MRI, mice with established kidney tumors were treated on day 13 with gemcitabine at a safe and therapeutic dose of dose of 20mg/kg, given 3-4 days apart, as determined from experiments described in Figure 5.1. Mice were then tested by DCE-MRI after 1, 3 or 4 doses of gemcitabine (day 14, 18 and 21 respectively). For data analysis, the full kidney was selected as the ROI both for the right tumor-bearing kidney and the left normal kidney (Figure 5.4A). As described above in Figure 5.1A, the IAUC and CIAUC curves for the tumor-bearing kidney in control mice, showed a pronounced shift to the right compared to normal kidney, indicative of a greater retention of Gd (Figure 5.4B, C, D). Interestingly, gemcitabine treatment caused improved clearance of Gd in the tumor bearing kidney compared to kidney tumors from control mice (Figure 5.4B). This was observed by a shift of the IAUC and CIAUC curves towards those of normal kidneys (Figure 5.4C, D). Furthermore, the patterns of Gd uptake and clearance were identical in the tumor-bearing kidney and the normal kidney with IAUC and CIAUC curves overlapping, and thus indicative of improved blood perfusion in the tumor (Figure 5.4). Gemcitabine also changed the pattern of uptake and clearance in the normal kidney compared to the normal kidney of control mice, showing a slower wash out of Gd (Figure 5.4B) and a wider IAUC distribution (Figure 5.4C). These data suggest that gemcitabine is also causing vascular changes in the normal kidney. It should be noted that vascular changes both in the kidney tumors and normal kidneys are consistently observed with 1, 3 or 4 doses of gemcitabine. These findings suggest that one dose of gemcitabine is sufficient to induce vascular changes which are reproducible with additional treatments of gemcitabine.

DCE-MRI parametric maps were derived from the C(t) curves for each pixel and represent the total Gd uptake (AUC) for the tumor and surrounding kidney tissue (Figure 5.4E). Parametric maps from control mice showed accumulation of Gd in the periphery of the tumor with no uptake in the tumor core, indicative of poor tumor perfusion (Figure 5.4E), as previously reported (Hillman et al., 2009). In the normal kidney of control mice, Gd uptake was distributed in the entire kidney with a higher uptake in the medullary central area than in the peripheral cortex, probably reflecting normal secretion of contrast agent (Figure 5.4E). Interestingly, gemcitabine caused striking changes observed by parametric maps with uptake of Gd in the core of the tumor, indicative of tumor perfusion (Figure 5.4E). The uptake of Gd in the tumor-bearing kidney was similar to that seen in the normal kidney (Figure 5.4E). These data were consistently reproduced following 1, 3 or 4 treatments of gemcitabine injections (Figure 5.4E).
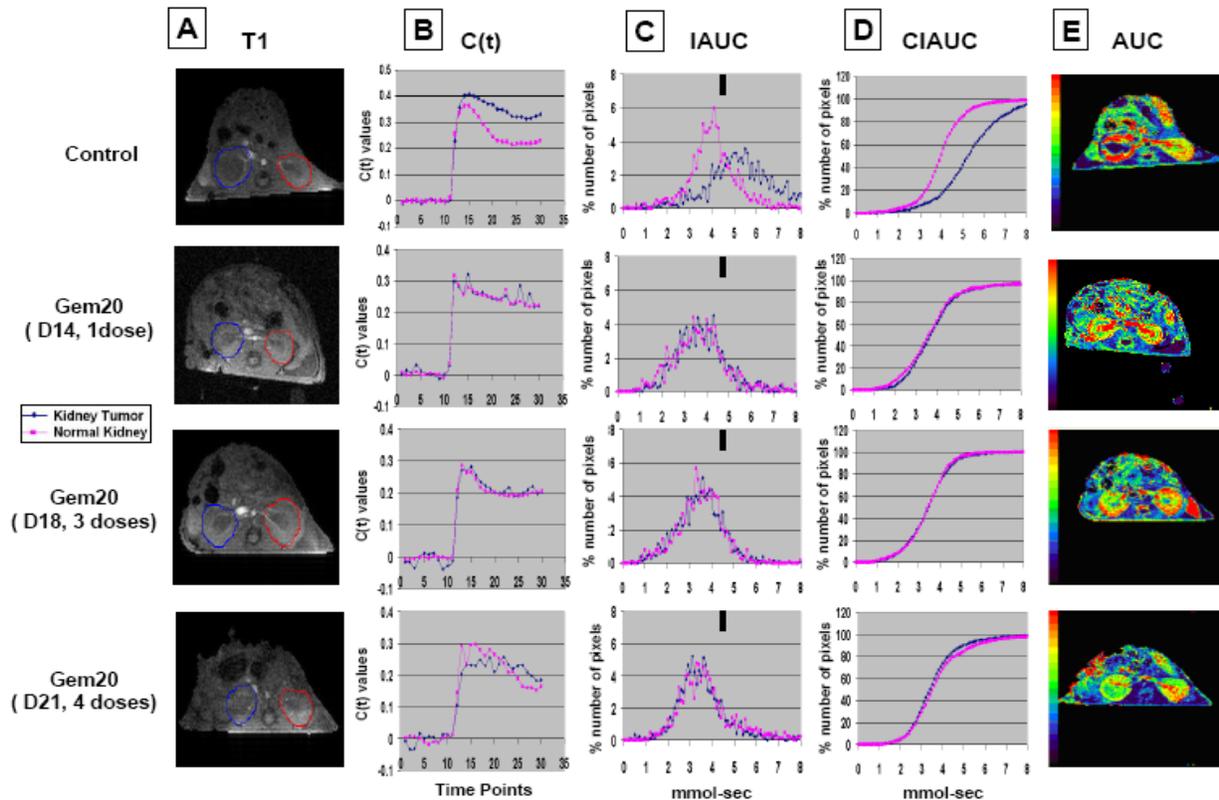
Figure 5.4: DCE-MRI imaging of vascular changes induced by gemcitabine in KCI-18 kidney tumors. In separate experiments, mice bearing established kidney tumors were treated with gemcitabine at 20mg/kg (Gem20) or with vehicle (control). Mice were imaged by DCE-MRI at 24 hrs following gemcitabine treatment after receiving either1 dose (Day 14), 3 doses (Day 18) or 4 doses (Day 21), given 3 days apart. (A) *T1 images:* Baseline images prior to Gd contrast agent injection. The full kidney was selected as the ROI for the tumor-bearing kidney (blue contour on left of T1 image) and the contralateral normal kidney (red contour on right of T1 image). (B) *C(t) kinetics of Gd contrast uptake and clearance:* The first 10 time points represent baseline data. Gd was injected at time point 10 and images were collected for 20 more time points. (C) *IAUC graphs:* Data from the C(t) curves were compiled for 16 time points (112sec) after Gd injection to draw $IAUC_{112}$. The small black bar indicates the peak position of normal kidney in control mice and can be used as a reference for curve shifting in normal kidneys and kidney tumors treated with gemcitabine. (D) *CIAUC graphs:* CIAUC curves were derived from IAUC curves. In A, B, C and D panels, blue lines are for kidney tumors and pink lines are for normal kidneys. (E) *AUC parametric map:* Parametric color maps were constructed based on uptake and concentration of Gd in the tissue, represented by the colors blue, green, yellow and red with gradual increase of Gd from lowest values (blue) to highest values (red). The tumor-bearing kidney is on the left and the normal contralateral kidney is on the right of the MR images. The color coding in the kidneys are shown for integrated AUC. Data from a representative mouse from each treatment group are presented.

5.4.6 DCE-MRI of Kidney Tumors Treated with Sunitinib and Gemcitabine

The effect of sunitinib, gemcitabine and both combined on kinetics of Gd uptake and clearance in tumors was evaluated by DCE-MRI. In this experiment, KCI-18 kidney tumor-bearing mice were pre-treated daily with sunitinib at a dose of 20 mg/kg per day (SU20), for 3 days on days 10, 11, 12 after KCI-18 cell implantation in the right kidney. On day 13, gemcitabine (GEM) was injected i.p. at 20 mg/kg, and this injection was repeated on day 15 and day 17 while continuing daily treatment with SU20. After these 3 doses of gemcitabine, on day 18, mice were imaged by DCE-MRI as previously described (Hillman et al., 2009). For data analysis, the full kidney was selected as the ROI both for the right tumor-bearing kidney and the left normal kidney (Figure 5.5A). Analysis of the kinetics of uptake and clearance of Gd showed that in control mice, the clearance of Gd in the tumor-bearing kidney was slow compared to faster clearance in the normal kidney (Figure 5.5B, C, D). Following treatment with SU20, the C(t) curves of the kidney tumors overlapped those of normal kidneys and showed similar uptake and improved Gd clearance with much less Gd retention than that of kidney tumors in control mice (Figure 5.5B). The tumor-bearing kidney IAUC curve looked more regular and shifted to the left compared to control kidney tumors indicating decreased Gd retention (Figure 5.5C). Gd uptake and clearance in the C(t) curves, IAUC and CIAUC showed identical patterns in the tumor-bearing kidney compared to the normal kidney (Figure 5.5B, C, D). These findings are consistent with our previous studies (Hillman et al., 2009) and suggest a return to more "normal vasculature" with lower permeability (i.e., less leaky vessels). Following treatment with gemcitabine, the vascular changes described in Figure 5.4 were reproduced in this experiment, including improved clearance of Gd in the tumor bearing kidney, and slower clearance of Gd in the normal kidney (Figure 5.5B, C, D). Following combined therapy of SU20 with gemcitabine,

the patterns of Gd uptake and clearance resembled those of gemcitabine alone both in kidney tumors and normal kidneys with a tendency to decreased clearance of Gd (Figure 5.5B, C, D). As observed for SU20 alone, the IAUC and CIAUC curves of kidney tumor and normal kidney overlapped and showed a pattern close to that of normal kidney in control mice (Figure 5.5C, D).

DCE-MRI parametric maps were derived from the C(t) curves for each pixel and represent the total Gd uptake (AUC) for the tumor and surrounding kidney tissue (Figure 5.5E). As described for Figure 5.4, parametric maps from control mice consistently showed accumulation of Gd in the periphery of the tumor with no uptake in the tumor core, indicative of poor tumor perfusion (Figure 5.5E). Parametric maps of SU20 treated mice showed a significant accumulation of Gd in the tumor-bearing kidney including Gd uptake in the tumor and also Gd accumulation in the normal kidney (Figure 5.5E), as shown previously (Hillman et al., 2009). Gemcitabine caused striking changes observed by parametric maps with tumor perfusion and an uptake of Gd similar to normal kidney (Figure 5.5E), as shown in separate experiments in Figure 5.4E. These findings were reproduced with the combined SU20 and gemcitabine including tumor perfusion but less Gd accumulation than that seen with SU20 alone (Figure 5.5E).
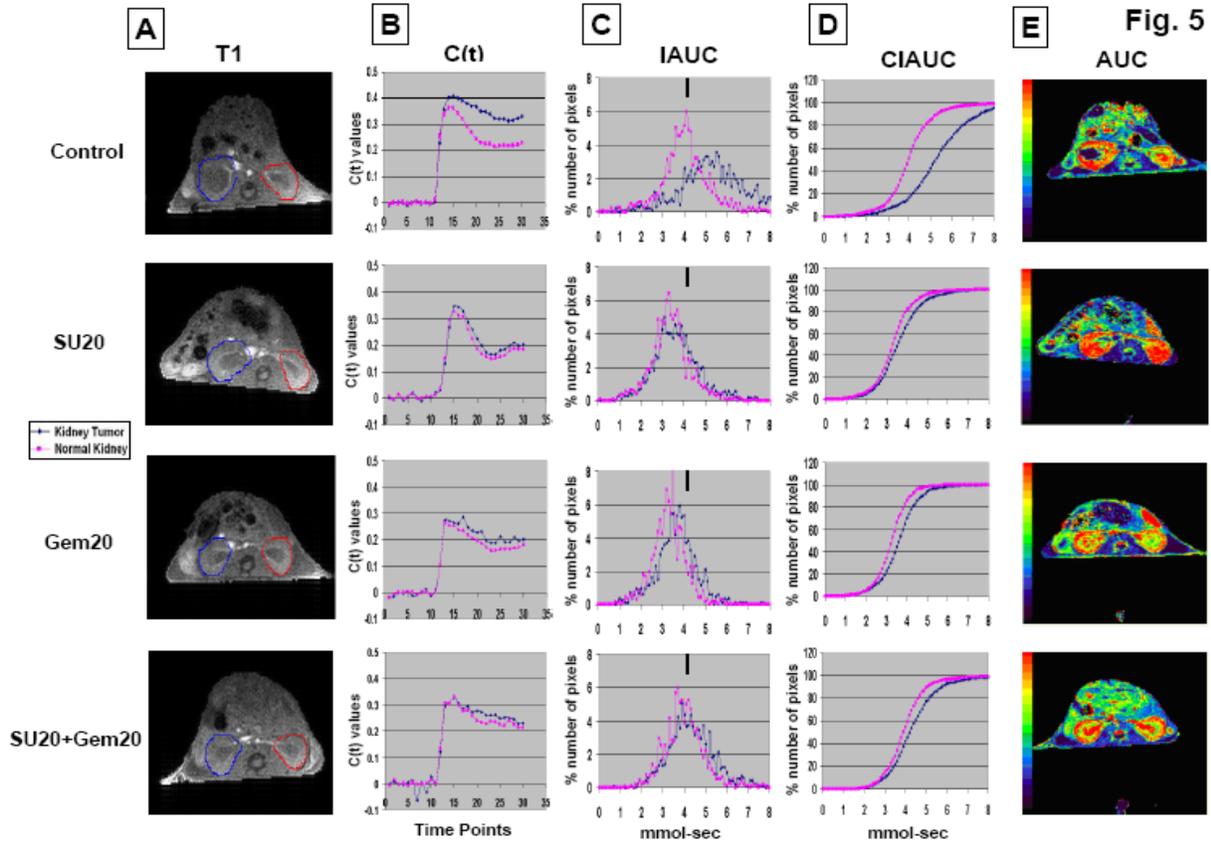
Figure 5.5: DCE-MRI imaging of vascular changes induced by gemcitabine and sunitinib in KCI-18 kidney tumors. Separate experimental groups of 3 mice per group were treated with vehicle only (control), or sunitinib only (SU20) or gemcitabine only (Gem20) or sunitinib + gemcitabine (SU20+Gem20). Mice bearing established kidney tumors were pre-treated with sunitinib at 20mg/kg/day (SU20) for 3 days on day 10-12 after KCI-18 cell injection in the kidney. Then, mice received three gemcitabine treatments at 20 mg/kg (Gem20) given on days 13, 15 and 17 while continuing daily sunitinib treatments. At 24 hrs after the last gemcitabine treatment (day 18), mice were imaged by DCE-MRI for 30 time points at 7 sec intervals. (A) *T1 images:* Baseline images prior to Gd contrast agent injection. The full kidney was selected as the ROI for the tumor-bearing kidney (blue contour on left of T1 image) and the contralateral normal kidney (red contour on right of T1 image). (B) *C(t) kinetics of Gd contrast uptake and clearance:* The first 10 time points represent baseline data. Gd was injected at time point 10 and images were collected for 20 more time points. (C) *IAUC graphs:* Data from the C(t) curves were compiled for 16 time points (112sec) after Gd injection to draw $IAUC_{112}$. The small black bar indicates the peak position of normal kidney in control mice and can be used as a reference for curve shifting in normal kidneys and kidney tumors following treatment. (D) *CIAUC graphs:* CIAUC graphs were derived from IAUC curves. In B, C and D graphs, blue lines are for kidney tumors and pink lines are for normal kidneys. Data from a representative mouse from each treatment group are presented. (E) *AUC parametric map:* Parametric color maps were constructed based on uptake and concentration of Gd in the tissue, represented by the colors blue, green, yellow and red with gradual increase of Gd from lowest values (blue) to highest values (red). The tumor-bearing kidney is on the left and the normal contralateral kidney is on the right of the MR images. The color coding in the kidneys are shown for integrated AUC.

5.4.7 DCE-MRI Quantitation of Vascular Changes of Kidney Tumors Treated with Sunitinib and Gemcitabine

To quantitate the vascular changes induced by sunitinib and gemcitabine and study the reproducibility of our findings, R50 values for 5 mice per treatment group were derived from CIAUC curves for both kidney tumors and normal kidneys (Hillman et al., 2009). The R50 (median) values correspond to the concentration of Gd at which 50% of the pixels have been included (Figure 5.6A) (Hillman et al., 2009). Lower R50 values were consistently observed in mice treated with SU20, gemcitabine and both combined compared to control mice for kidney tumors (Figure 5.6B). Compared to R50 values of normal kidneys in control mice, a trend to lower R50 was also observed for normal kidneys suggesting a mild systemic effect of both drugs affecting blood flow (Figure 5.6C). To compare the vascular changes induced by the drugs in kidney tumors to those induced in normal kidneys, R50 values of kidney tumors were normalized to the R50 values of normal contralateral kidneys for each mouse (NR50 KT v/s NK) (Figure 5.6D) (Hillman et al., 2009). These values were consistently much smaller in mice treated with each drug and both combined compared to control mice (Figure 5.6D). Normalization of R50 values of treated kidney tumors versus control kidney tumors (NR50 KT_{treat} v/s KT_{cont}) showed negative values with each drug alone and both combined (Figure 5.6E). To assess the effect of SU20 and gemcitabine on normal contralateral kidneys, R50 of normal kidneys from treated mice were normalized to normal kidneys from control mice (Figure 5.6F). These NR50 data of normal kidneys showed also negative values for mice treated with each drug separately and both combined (Figure 5.6F) but less than those of NR50 KT_{treat} v/s KT_{cont}. These data indicate a relatively mild effect by either drug alone and combined on normal

kidney vasculature (Figure 5.6F) in contrast to a more pronounced effect on vasculature of kidney tumors (Figure 5.6E).
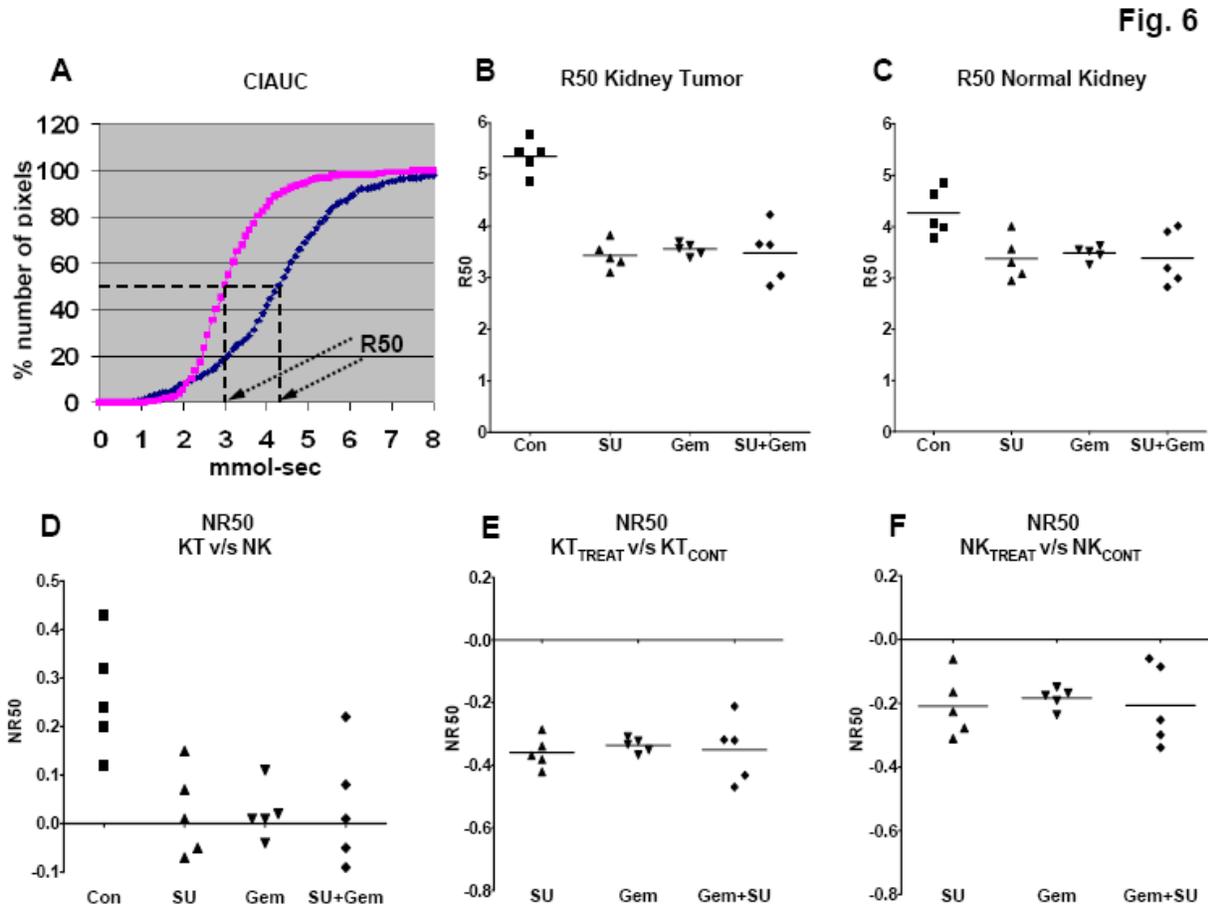
Figure 5.6: R50 quantitation of DCE-MRI data of KCI-18 kidney tumors. Mice were treated with vehicle (control, Con), sunitinib at 20mg/kg/day (SU), gemcitabine at 20 mg/kg (Gem) or both sunitinib and gemcitabine, and then imaged by DCE-MRI as described in Figure 5.5. Data obtained from MRI images were quantitated. (A) *R50 value calculation:* The R50 value is derived from CIAUC curves (as shown for control mouse) and corresponds to the Gd concentration at which 50% of the pixels have been included. (B) *Tumor-bearing kidney R50:* R50 of kidney tumors from 5 mice per treatment group. (C) *Normal kidney R50:* R50 normal contralateral kidney for each mouse shown in B. (D) *NR50 of KT vs NK:* NR50 represents normalization of R50 values of kidney tumors (KT) relative to R50 values of normal contralateral kidney (NK) calculated as $[R50_{KT} - R50_{NK}] / R50_{NK}$ for each mouse. (E) *NR50 of KT_{TREAT} vs KT_{CONT}:* Normalization of R50 values of kidney tumors from treated mice (KT_{TREAT}) relative to the mean R50 values of kidney tumors from control mice (KT_{CONT}) calculated as $[R50\,KT_{TREAT} - R50\,KT_{mean\,cont}] / R50\,KT_{mean\,cont}$ for each mouse. (F) *NR50 of NK_{TREAT} vs NK_{CONT}:* Normalization of R50 values of normal kidneys of treated mice relative to the mean R50 values of normal kidneys from control mice calculated as $[R50\,NK_{TREAT} - R50\,NK_{mean\,cont}] / R50\,NK_{mean\,cont}$ for each mouse. Data are presented for 5 mice per treatment group in each panel.

5.5 Discussion

The concept of normalization of tumor vessel via elimination of excess endothelial cells to improve the blood flow, reduce vessel leakiness, interstitial pressure and increase drug delivery to tumor cells, has shown promise for combination with anti-cancer drugs [37-39]. We have previously determined the doses and schedule of the anti-angiogenic drug sunitinib which cause thinning and regularization of tumor vessels in kidney tumors of the KCI-18 RCC orthotopic tumor model in nude mice (Hillman et al., 2009). We found that daily treatment with 20mg/kg/day of sunitinib caused better tumor perfusion and decreased vascular permeability by DCE-MRI (Hillman et al., 2009). These observations on vascular changes were in agreement with *in situ* histological studies demonstrating thinning and regularization of tumor vessels (Hillman et al., 2009). In addition, this dose caused only mild changes in vessels in normal kidney tissue and was not toxic to the mice (Hillman et al., 2009). Based on these findings, the dose of 20mg/kg/day of sunitinib was selected to regularize the blood flow in the tumor and then schedule chemotherapy with gemcitabine. The conditions for combining anti-angiogenic therapy with chemotherapy were investigated.

Dose searching studies using 10, 20 or 40 mg/kg of gemcitabine showed that a schedule of injections given 3 days apart was less toxic than every two days. Doses of 20 and 40 mg/kg gemcitabine were more effective than 10 mg/kg and caused significant kidney tumor growth inhibition. To schedule the combination of gemcitabine with sunitinib, regularization of tumor vessels was monitored by DCE-MRI of kidney-tumor bearing mice treated with sunitinib only. DCE-MRI showed that one day sunitinib treatment at a dose of 20mg/kg/day was not sufficient to induce regularization of vasculature and resulted only in minor vascular changes (Hillman, personal communications). However, DCE-MRI of mice treated for 3 days with 20mg/kg/day

sunitinib confirmed that this schedule was sufficient to induce vascular changes of decreased Gd retention and improved tumor perfusion in KCI-18 kidney tumors, indicating normalization of blood vessels. Therefore, gemcitabine treatment was initiated after 3 consecutive daily treatments of sunitinib. When gemcitabine was administered after sunitinib and given at a dose of 20 mg/kg for four treatments, while continuing daily administration of sunitinib, the effect of the combined therapy was particularly effective causing about 74% reduction in tumor weight by day 28. This schedule and dosage of sunitinib given in conjunction with gemcitabine were well tolerated by the mice and were not associated with toxicity. This combined therapy significantly inhibited the growth of the tumor in the kidney and this effect was consistent in all mice tested in contrast to greater variability from mouse to mouse with each modality alone. The size and shape of the tumor-bearing kidneys were comparable to those of the normal contralateral kidneys. In agreement with our gross observations, only small residual tumor nodules surrounded by normal kidney tissue were histologically observed. Tumors treated with gemcitabine alone or both gemcitabine and sunitinib showed a high frequency of abnormal giant tumor cells with degenerative changes in their cytoplasm and nuclei, indicative of processes of cell death. Similar effects of the single and combined modalities were also observed histologically in the spontaneous lung metastases. In lungs of sunitinib-treated mice, the tumor nodules showed a decrease in size, cellularity and vascularization, probably as a result of the anti-angiogenic activity of sunitinib. Gemcitabine treatment caused a marked increase in giant tumor cells with degenerative processes in metastatic lung nodules, which looked identical to those observed in primary kidney tumors. This effect was more pronounced in lung tumor nodules treated with the combined therapy, as visualized by few remaining giant tumor cells surrounded by fibrotic areas. The frequency and size of metastatic lung tumor nodules were drastically reduced by

gemcitabine alone or combined with sunitinib compared to control mice. These findings observed in spontaneous lung metastases suggest that sunitinib and gemcitabine act systemically affecting both the primary and metastatic tumors and therefore a combined approach of anti-angiogenic drug and chemotherapy drug could be effective for metastatic RCC disease.

Long-term survival studies, using a schedule of 3 days of 20mg/kg of sunitinib followed by five treatments of 20mg/kg of gemcitabine and continued daily administration of sunitinib resulted in a significant increase in mouse survival. Interestingly, even though sunitinib daily treatment was continued after gemcitabine therapy, kidney tumors recurred as observed by day 50. These data suggest that 20mg/kg of sunitinib was not sufficient to maintain the initial dramatic inhibition of tumor growth induced by gemcitabine and prevent regrowth of tumor vessels. It should be noted that the total dose of gemcitabine (100-120mg/kg) used in our study is much lower than that used in pancreatic cancer pre-clinical models (480mg/kg) (Bocci G et al., 2004). This low dose of gemcitabine in our RCC pre-clinical model is very effective when combined with an anti-angiogenic drug as shown in the pancreatic cancer model (Bocci G et al., 2004). These data also demonstrate that DCE-MRI is a useful means to monitor early vascular changes induced by sunitinib to assess improved blood flow and schedule initiation of chemotherapy. Recent clinical studies have successfully shown that early changes in DCE-MRI of cancer patients have the potential to predict response and guide therapy (Ah-See et al., 2008; Craciunescu et al., 2009; Galban et al., 2009).

Our previous observations of uptake and clearance of Gd in control kidney tumors monitored by DCE-MRI were confirmed in the current study (Hillman et al., 2009). These patterns included slow clearance of Gd and accumulation of Gd in the periphery of the tumor with no uptake in the tumor core, as seen in parametric maps. These findings suggested poor

tumor perfusion, probably as a result of leakiness from abnormal enlarged tumor vessels as observed by histology of tumor sections and extravasation of RBC's (Hillman et al., 2009). Imaging of kidney tumor-bearing mice treated with gemcitabine by DCE-MRI revealed that gemcitabine caused vascular changes both in the tumors and in normal kidneys. Kidney tumors treated with gemcitabine showed improved clearance of the Gd contrast agent relative to the normal contralateral kidney. Increased tumor perfusion caused by gemcitabine was also observed by parametric maps showing uptake of Gd in the core of the tumor in contrast (Hillman et al., 2009). Histologically, gemcitabine-treated tumors showed a decrease in the number of enlarged vessels compared to control tumors. These findings on improved tumor perfusion associated with trimming of the enlarged vessels of the kidney tumors suggest that gemcitabine also exerted cytotoxic activity on endothelial cells. In agreement with our findings, recent studies demonstrated that endothelial cells are indeed destroyed by gemcitabine both in vitro and in vivo in an orthotopic pre-clinical model of pancreatic cancer (Laquente et al., 2008). These studies and our findings indicate that the mode of action of gemcitabine includes both cytotoxicity to tumor cells but also an anti-angiogenic effect, thus acting as well on the tumor microenvironment as shown for sunitinib (Laquente et al., 2008).

Consistent with our previous studies, sunitinib treatment of kidney tumors with 20mg/kg showed patterns of uptake and improved Gd clearance by DCE-MRI, comparable to those of normal kidneys, suggesting a return to more "normal vasculature" with lower permeability (i.e., less leaky vessels) (Hillman et al., 2009). Histologically, kidney tumors treated with sunitinib showed considerable thinning, regularization and organization of tumor vessels, as previously reported (Hillman et al., 2009). Combination of sunitinib and gemcitabine, the patterns of Gd uptake and clearance resembled those of gemcitabine alone both in kidney tumors and normal

kidneys with a tendency to decreased clearance of Gd. Parametric maps showed increased tumor perfusion. These data were in agreement with *in situ* histological findings showing tumor vessels looking more trimmed and organized than those seen after gemcitabine treatment alone.

Quantitation of vascular changes induced by sunitinib and gemcitabine confirmed the reproducibility of our findings. Lower R50 values were consistently observed in mice treated with SU20, gemcitabine and both combined compared to control mice for kidney tumors. A trend to lower R50 values was also observed for normal kidneys in treated mice relative to control mice. These findings were corroborated by *in situ* histological observation of dilatation of some of the vessels in normal kidney tissue sections. These data indicate a relatively mild systemic effect on normal kidney vasculature mediated by either drug alone and both drugs combined. This is in contrast to a more pronounced effect of the therapy on kidney tumor vasculature resulting in increased tumor perfusion and decreased vascular permeability.

Our data suggest that both sunitinib and gemcitabine exert anti-angiogenic effects in addition to their cytotoxic anti-tumor activity. These effects on both the tumor vasculature and tumor cells were observed both in primary kidney tumors and spontaneous lung metastases indicating that a combined approach of anti-angiogenic drug and gemcitabine could be effective for metastatic RCC disease. These studies also emphasize the clinical potential of using DCE-MRI to select the dose and schedule of anti-angiogenic drugs to schedule chemotherapy and improve its efficacy.

Chapter Six

New DCE-MRI Parameters to Quantify Regional Vascular Changes Induced by Sunitinib Treatment in Renal Carcinoma Tumors: A Mean to Enhance DCE Reproducibility

Areen K. Al-Bashir[1,2], Gilda G. Hillman[3], Meng Li[2], Yashwanth Katkuri[2], Vinita Singh-Gupta[3], Yimin Shen[2], Christopher K Yunker[3], and E. Mark Haacke[1,2].

[1]Department of Biomedical Engineering, [2]Department of Radiology and [3]Department of Radiation Oncology; Wayne State University School of Medicine, Detroit, MI 48201, USA.

*Corresponding Author:

E. Mark Haacke, Ph.D.

Wayne State University

Department of Radiology

3990 John R St.

Detroit MI 48201.

Tel: 313-745-1395

Fax: 313-745-9182

E-mail: nmrimaging@aol.com

Key Words: dynamic contrast-enhanced (DCE) MRI, renal cell carcinoma, sunitinib.

6.1 Abstract:

Purpose: To develop new dynamic contrast enhanced (DCE) magnetic resonance imaging (MRI) parameters to quantify the vascular effects of different doses of the antiangiogenic drug sunitinib on renal cell carcinoma (RCC) kidney tumors in mice.

Materials and Methods: Mice bearing established RCC xenograft tumors were treated with sunitinib doses of 10, 20 or 40 mg/kg/day respectively (SU10, SU20 or SU40) or treated with vehicle only (control). New DCE parameters, including fraction of active pixels (FAP), contrast agent uptake to the peak (AUCtp), time to peak concentration (TTP), washout slope (Nslope) and full width half maximum (FWHM) were obtained from T1-weighted images. These parameters, as well as more conventional measures, were quantified for tumor-bearing kidneys and normal kidneys.

Results: Treatments with SU20 and SU40 caused increased perfusion in the tumor core compared to control and SU10. Kidney tumors treated with SU20 had an almost identical pattern of contrast agent uptake rate, peak and clearance as those observed in normal kidneys. The effect of SU20 on normal kidneys was milder than that observed with SU40. Treatment with SU40 caused increased contrast agent uptake by the cortex of the normal kidneys compared to the normal kidneys in control and SU10. FWHM also provided new information about the effect of different treatment doses and showed that kidney tumors treated with SU20 have almost the same values of FWHM as the normal kidneys in control mice. The other measures also painted a consistent picture of the treatment effect on the vascular system.

Conclusion: The new DCE parameters, including FAP, AUCtp, Nslope and FWHM have the potential to give a precise description of the treatment effect not only in the whole mouse kidney but also in different regions inside the kidney. The results of this work should enhance the reproducibility of DCE results.

6.2 Introduction:

Numerous clinical studies have used dynamic contrast enhanced (DCE) magnetic resonance imaging (MRI) as a non-invasive method to diagnose lesions of different types (Huang et al., 2004; Ng et al., 2010), to grade lesions (Asaumi et al., 2003; Ludemann et al., 2005; Bhooshan et al., 2010) and to evaluate drug effectiveness on tumor vascular characteristics (Hayes et al., 2002; Haris et al., 2008). Many of these studies have shown that DCE is a valuable tool to study tissue perfusion. DCE-MRI uses gadolinium diethylenetriamine penta-acetic acid (Gd-DTPA) as a contrast agent injected into the blood stream. Gd is assumed to be well mixed with the blood and travels through the major vessels and capillaries. The perfusion of the tissue can be assessed using dynamic T1-weighted images since Gd shortens the T1 value of the blood. Signal enhancement depends on the concentration of Gd in the blood. The kinetics of the changes in signal intensity before, during and after Gd injection, for a region of interest (ROI), indirectly provides Gd concentration in that ROI (Knopp et al., 2001). However, Gd concentration, in any selected ROI, depends on tissue hemodynamic parameters and vasculature (Tofts and Kermode, 1991; Preda et al., 2006; Yabuuchi et al., 2008). In tumors, Gd leaks from abnormal vessels into extracellular space. The number of blood vessels in tumors and the trans-endothelial permeability of the vessels are often higher than the ones in normal tissue. Hence, more signal enhancement will occur in tumors. The role of DCE-MRI is to measure these hemodynamic parameters to help differentiate between normal and malignant tissues (Preda et al., 2006; Van Cann et al., 2008).

The assessment of tissue hemodynamic characteristics can be executed by semi-quantitative or quantitative methods (Galbraith et al., 2002; Yankeelov and Gore, 2009). Semi-quantitative methods include histogram analysis of Gd uptake and washout and parametric maps.

These evaluations depend on many factors such as Gd injection, hardware settings, sequence choice and systemic changes in the blood circulation (Galbraith et al., 2002). On the other hand, quantitative methods are independent of these factors. In these methods, DCE data can be fitted to a pharmacokinetic model to estimate values for vessel wall permeability, vessel surface area, volume fraction of vascular plasma and the volume fraction of extracellular extravascular space (EES) (Murase, 2004; Yankeelov and Gore, 2009). Among other models, Toft's model is often used to produce K^{trans} (which represents the product of the capillary wall permeability and surface area per unit volume), v_e (volume of the extravascular extracellular space (EES)) and EES maps (Tofts and Kermode, 1991; Tofts et al., 1995; Guo and Reddick, 2009). Nevertheless, DCE quantification is not easy, and these quantitative methods require an accurate arterial input function (AIF) and a pharmacokinetic model for data fitting (Yang et al., 2004; Cutajar et al., 2009).

Renal cell carcinoma (RCC) develops in the kidney and metastasizes to other organs, most particularly the lungs (Whang and Godley, 2003). The vascular endothelial growth factor (VEGF) is a key growth factor in the angiogenic process, which promotes the proliferation, migration, and invasion of endothelial cells and plays a role in vascular permeability. Sunitinib is an antiangiogenic drug which has recently shown a significant therapeutic effect (van Spronsen et al., 2005; Rini, 2009). It has been found to inhibit tumor growth by selective inhibition of the VEGF receptors and platelet-derived growth factor causing apoptosis in both tumor microvessels and in the tumor cells (Patard et al., 2006; Billemont et al., 2007; Papaetis et al., 2008; Sawhney and Kabbinavar, 2008; Gan et al., 2009). This treatment can deprive the tumor cells of nutrients, and hence inhibit its growth. However, higher doses of sunitinib, which cause complete destruction of tumor blood vessels, can also affect the normal vasculature of vital

organs such as the heart, and could cause the blood vessels to leak more (Gan et al., 2009). These high doses of sunitinib could also alter blood flow and oxygen delivery to the tumor affecting the efficacy of combining this treatment with either chemotherapy or radiotherapy. In the current study, we report the development of four new DCE parameters that characterize the behavior of Gd uptake with time. The new proposed parameters were calculated from the DCE data of a preclinical model of the human RCC KCI-18 cell line implanted in the right kidney of immune deficient nude mice (Hillman et al., 2009). Mice bearing established KCL-18 kidney tumors were treated with different doses of sunitinib. Vascular changes induced by the drug were analyzed by DCE-MRI. We previously reported DCE-MRI studies in this model, in which we presented the parameters of the initial area under the curve (IAUC), the cumulative initial area under the curve (CIAUC) graphs and the R50 (median) value that represents the concentration of Gd at which 50% of the pixels have been included (Hillman et al., 2009). These DCE-MRI data were further analyzed by evaluating four new DCE parameters, including blood volume estimates, washout slope, fraction of active pixels as well as the full width at half maximum (FWHM). These parameters were compared to more conventional measures.

6.3 Materials and Methods:

6.3.1 KCI-18/IK RCC Tumor Model:

A preclinical model of RCC was established by implantation of Karmanos Cancer Institute-18 (KCI-18) human papillary RCC cell lines in the right kidney of immune deficient nude mice. Mice were housed and handled under sterile conditions in facilities accredited by the American Association for the Accreditation of Laboratory Animal Care. The animal protocol was approved by the Wayne State University Animal Investigation Committee. A few mice were killed at an early time point to assure tumor growth before initiating the treatment. By days 10 to 12, after KCI-18 cell injection, mice were treated with sunitinib (Pfizer, Inc, New York, NY). Sunitinib treatment was prepared in a carboxymethyl cellulose suspension vehicle. Mice were divided into four groups: three groups were treated with sunitinib at different doses of 10, 20, or 40 mg/kg/day (SU10, SU20, or SU40, respectively), and the fourth group was treated with vehicle only (control mice). Sunitinib treatment were given orally by gavage on a daily basis for 7 days, and then mice were imaged by DCE-MRI, as previously detailed (Hillman et al., 2009).

6.3.2 MR Imaging:

Mice were anesthetized by intraperitoneal injections of 0.35 ml pentobarbital and 0.35ml ketamine at a concentration of 52.5mg/kg. A catheter was then inserted into their tail vein, which was attached to a syringe containing Gd-DTPA contrast agent (Berlex, Wayne, NJ). Mice were positioned on a cradle heated by temperature-controlled water and were given a second low dose of anesthetics of 15mg/kg each in 0.1ml to avoid motion problems while scanning the animal in the magnet. A 2-cm diameter receive-only surface coil was placed over the tumor, and the cradle was placed inside an 11-cm inner diameter transmit-only volume coil. MR imaging was

performed in the MR Research Facility at Wayne State University, using a Bruker Biospec AVANCE animal scanner (Bruker, Karlsruhe, Germany) equipped with a 4.7-T horizontal bore magnet and actively shielded. Anatomical imaging was done using a 2D T2-weighted spin echo scan (TR = 2000ms, TE = 52.4ms) to get an overview of the kidney. The DCE-MRI images were collected at 30 time points (7 sec between time points) with the following parameters: 5 slices, TR = 54.7 ms, TE = 2.9 ms, two flip angles 5 and 30 degrees, FOV = 32mm x 32mm, slice thickness = 1.5mm with 0.5 mm gap and matrix = 128x128. The contrast agent dose was 0.1mmol/kg of body weight Gd-DTPA (Magnevist, Berlex Laboratories, Wayne, NJ) and was injected at time point 10 into the tail vein catheter. Then, images were acquired for 20 more time points. All DCE data analysis was done using our homemade software SPIN (signal processing in NMR, Detroit, MI) (Haacke et al., 2007).

6.3.3 DCE Theory:

The changes in the DCE signal with time, S(t), for a given flip angle, can be obtained from the FLASH equation

$$S_\theta(t) = \frac{\rho_0 \sin\theta (1 - e^{-TR/T1(t)})}{(1 - e^{-TR/T1(t)} \cos\theta)} \qquad [5.1]$$

where ρ_0 is the spin density, θ is the flip angle and TR is the repetition time. For a given TR, T1(t) can be calculated from the equation above. Knowing T1(t) and using a fixed T1(0) equal to 1000 ms (Haacke et al., 2007), the concentration of Gd with time can be calculated from

$$C(t) = \frac{1}{a} * \left[\frac{1}{T1(t)} - \frac{1}{T1(0)} \right] \qquad [5.2]$$

where "a" is the proportionality constant referred to as the longitudinal or T1 relaxivity with units of $(mM)^{-1}s^{-1}$, and it is a property specific to the composition of Gd.

Once C(t) is known , IAUC is calculated from

$$IAUC = \sum_{t1}^{t2} C(t)\Delta t \qquad [5.3]$$

where t_1 and t_2 are user defined time points. CIAUC (which represents the cumulative number of pixels counted within an ROI that corresponds to a given contrast agent uptake ($IAUC_i$ for ($0 \leq i \leq N$ bins) in a given ROI) and normalized to the total number of pixels), is calculated from

$$CIAUC(m) = \frac{\sum_{i=1}^{m} n(IAUC_i)}{\sum_{i=1}^{N} n(IAUC_i)} \qquad [5.4]$$

where N is the last bin or maximum IAUC and $n(IAUC_i)$ is the number of pixels with a value of the IAUC bin.

The R50 value was defined as the concentration of Gd at which CIAUC(m) = 50%, i.e., the median of the CIAUC histogram, and NR50 is defined as the normalized value of R50 as

$$NR50 = (R50_{tumor} - R50_{normal}) / R50_{normal} \qquad [5.5]$$

6.3.4 DCE Data Thresholding and Fraction of Active Pixel Determination:

The drug effectiveness in semi-quantitative DCE-MRI analysis depends on the change of Gd uptake. A tumor might be composed of either cells which are alive or dead (necrotic) (Karahaliou et al., 2010). A set of subtracted images is created by subtracting a set of DCE images of a given time point after Gd injection from a set of DCE images of a time point before Gd injection. These images can help us differentiate between active or necrotic vascular areas of the tumor. Applying a threshold to the original DCE images and to the subtracted series is used to suppress pixels that are just noise or have no signal enhancement. The threshold value was estimated from the image background noise. The pixels excluded from dynamic DCE image

thresholding represent the noise pixels whereas the pixels excluded from subtracted images represent the no signal enhancement pixels (i.e., necrotic part of the tumor). As a further measure of interest, we define the fraction of active pixels (FAP) as the number of active pixels (i.e., the remaining pixels after applying the threshold) normalized to the total number of pixels in the ROI.

6.3.5 DCE Parametric Maps: New Parameters AUCtp and TTP:

The concentration time dependence, C(t), will vary according to the tissue hemodynamic properties. Given a general rise and fall of C(t), we calculate 6 different DCE parametric maps for each pixel in the image. These include the total Gd uptake (AUC), the rate of uptake (Pslope), the peak concentration (PEAK), the uptake to the peak (AUCtp), the time to peak concentration (TTP) and the clearance or washout slope of Gd (Nslope). Figure 6.1 shows the C(t) curve and the time points (t_i, t_{peak}, t_{ns}, t_{end}) that were used to calculate the DCE parametric maps. The definitions for these measures are given by

$$\text{AUC} = \sum_{t_i}^{t_{end}} C(t) \bullet \Delta t \tag{5.6}$$

$$\text{Pslope} = (C(t_{peak}) - C(t_i))/(t_{peak} - t_i) \tag{5.7}$$

$$\text{PEAK} = C_{peak} = \text{Max}(C(t)) \tag{5.8}$$

$$\text{AUCtp} = \sum_{t_i}^{t_{peak}} C(t) \bullet \Delta t \tag{5.9}$$

$$\text{TTP} = t(C_{peak}) = t_{peak} \tag{5.10}$$

and

$$\text{Nslope} = (C(t_{ns}) - C(t_{peak}))/(t_{ns} - t_{peak}) \tag{5.11}$$

where t_i is the Gd injection time point at which $C(t_i)-C(t_{i+1}) > 2SD$, t_{peak} is the time at the concentration peaks, t_{ns} is the time point at which $(C(t_{peak})-C(t_{ns}))/(t_{peak}-t_{ns}) > (C(t_{peak})-C(t_{end}))/(t_{peak}-t_{end})$, and t_{end} is the last acquired time point. $C(t_i)$ is Gd concentration at the injection time point, $C(t_{peak})$ is Gd concentration at the peak, $C(t_{ns})$ Gd concentration at t_{ns}, and finally $C(t_{end})$ is Gd concentration at the last acquired time point (Figure 6.1). AUC is defined the same as IAUC except that it is integrated from the injection time point (t_i) to the last acquired time point (t_{end}) where IAUC is integrated to a user defined time points (t_1 and t_2).
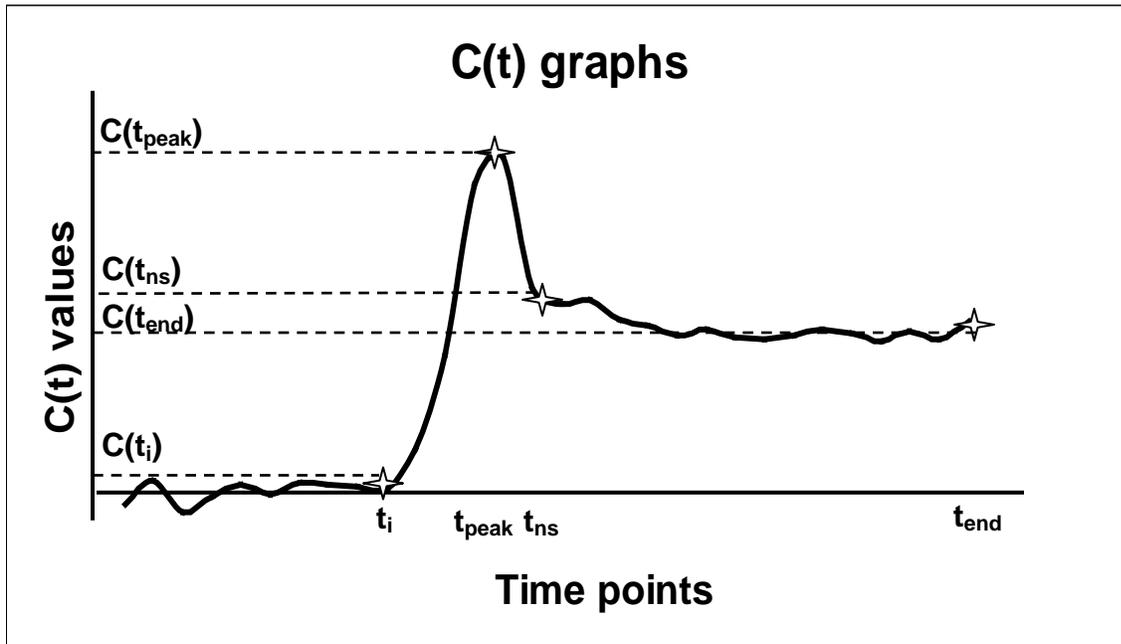
Figure 6.1: Kinetics of Gd uptake are represented in $C(t)$ curves showing Gd injected at t_i time point, peak of Gd uptake (t_{peak}), the time point at which $(C(t_{peak})-C(t_{ns}))/(t_{peak}-t_{ns}) > (C(t_{peak})-C(t_{end}))/(t_{peak}-t_{end})$ (t_{ns}) and the last time point (t_{end}) at which images were acquired. $C(t_i)$ is Gd concentration at the injection time point, $C(t_{peak})$ is Gd concentration at the peak, $C(t_{ns})$ Gd concentration at t_{ns}, and finally $C(t_{end})$ is Gd concentration at the last acquired time point. The DCE parametric maps are obtained from $C(t)$ curves.

In the case where there is no extravasation of the contrast agent prior to t_{peak}, AUCtp can be used as a measure of the blood volume fraction (λ) as follows:

$$\lambda = \frac{AUCtp_{tissue}}{AUCtp_{blood}} = \frac{\sum_{t_i}^{t_{peak}} C_{tissue}(t) \cdot \Delta t}{\sum_{t_i}^{t_{peak}} C_{blood}(t) \cdot \Delta t} \quad\quad [5.12]$$

where AUCtp for tissue has been normalized to AUCtp for blood.

6.3.6 Full Width at Half Maximum (FWHM)

Another potential characteristic measure is the full width at half maximum (FWHM), which represents how fast the contrast agent is washed out across all pixels. FWHM is thought to be more resilient to the effects of contrast agent leakage. In order to calculate the FHWM, the IAUC data should be filtered to reduce noise using a direct form transposed II digital filter. This filter contains implementation of the standard difference equation.

After filtering IAUC data, FWHM is found from the difference between the two half-maximum points:

$$FWHM = |x_2 - x_1| \quad\quad [5.13]$$

where x_2 and x_1 represent the two half maximum times at which $IAUC(x_2) = IAUC(x_1)$ as shown in Figure 6.2.
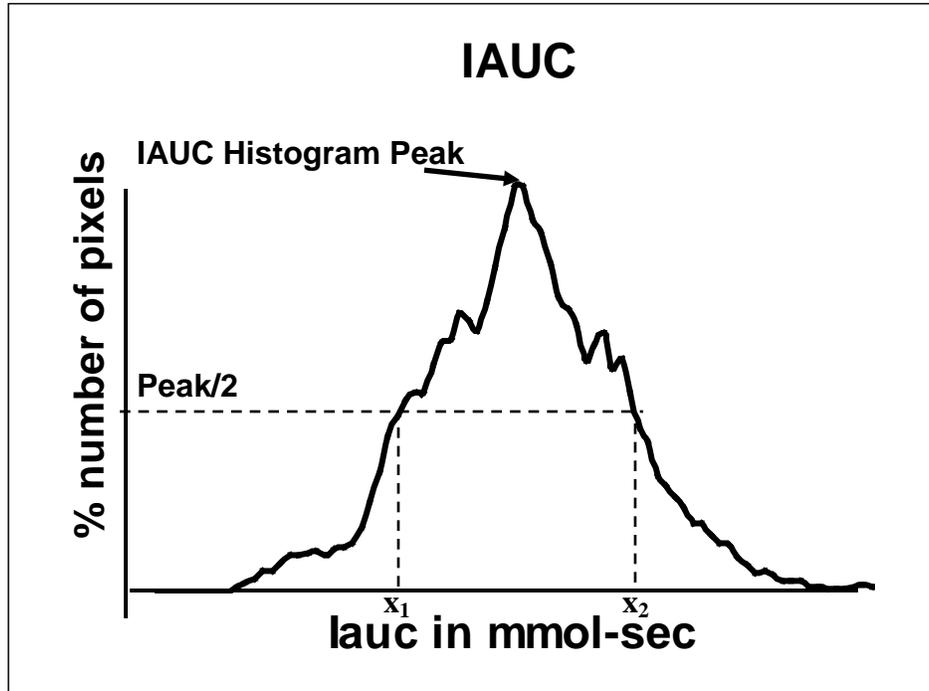
Figure 6.2: Determination of full width at half maximum (FWHM). For each mouse included in the study, IAUC data was filtered to reduce noise using an averaging filter. The maximum value of the IAUC histogram was found. FWHM is calculated from the difference between the two half-maximum points x_1 and x_2.

6.4 Results:

6.4.1 Threshold of Data Images and Assessments of FAP

The original DCE and subtracted images were used to draw two ROIs on both the right tumor-bearing kidney and the left normal kidney (Figure 6.3-a and 6.3-b). The necrotic area or poorly vascularized part of the tumor appears as a black area in the subtracted images. These pixels (i.e., necrotic part of the tumor) are thresholded out of C(t) to be processed since they shift the CIAUC curves to the left indicating less Gd uptake (Figure 6.3-d). The simplest and currently most effective means to threshold DCE images is to set the signal intensity for the pixel whose intensity falls out of a certain range to zero and exclude these pixels from further quantification. Using a fixed T1(0)= 1000ms, threshold= 20 (measured from background noise of the original DCE image), the concentration of Gd-DTPA, C(t), uptake in both kidneys was calculated over time. The IAUC and CIAUC graphs were integrated over 16 time points (112 sec) after Gd-DTPA injection. The resulting, un-thresholded IAUC has a bimodal distribution (Figure 6.3-c) and hence shifts the CIAUC curve more to the left (Figure 6.3-d). However, after applying the threshold, the IAUC is more Gaussian distributed (Figure 6.3-e), and the resulting CIAUC is shifted back to the right compared to the CIAUC curve before applying the threshold (Figure 6.3-f). This better indicates Gd uptake in active tissue. FAP values were calculated for all the cases. In general, FAP values for the normal kidneys are higher than the FAP values in the kidney tumor due to the presence of necrotic areas in the tumor (Table 6.1). R50 values after applying the threshold are larger than R50 values before applying the threshold (Figure 6.4-a and 6.4-b). However, one could notice that the changes in R50 values before and after applying the threshold follow the same trend in normal kidneys where as it varies in kidney tumors.
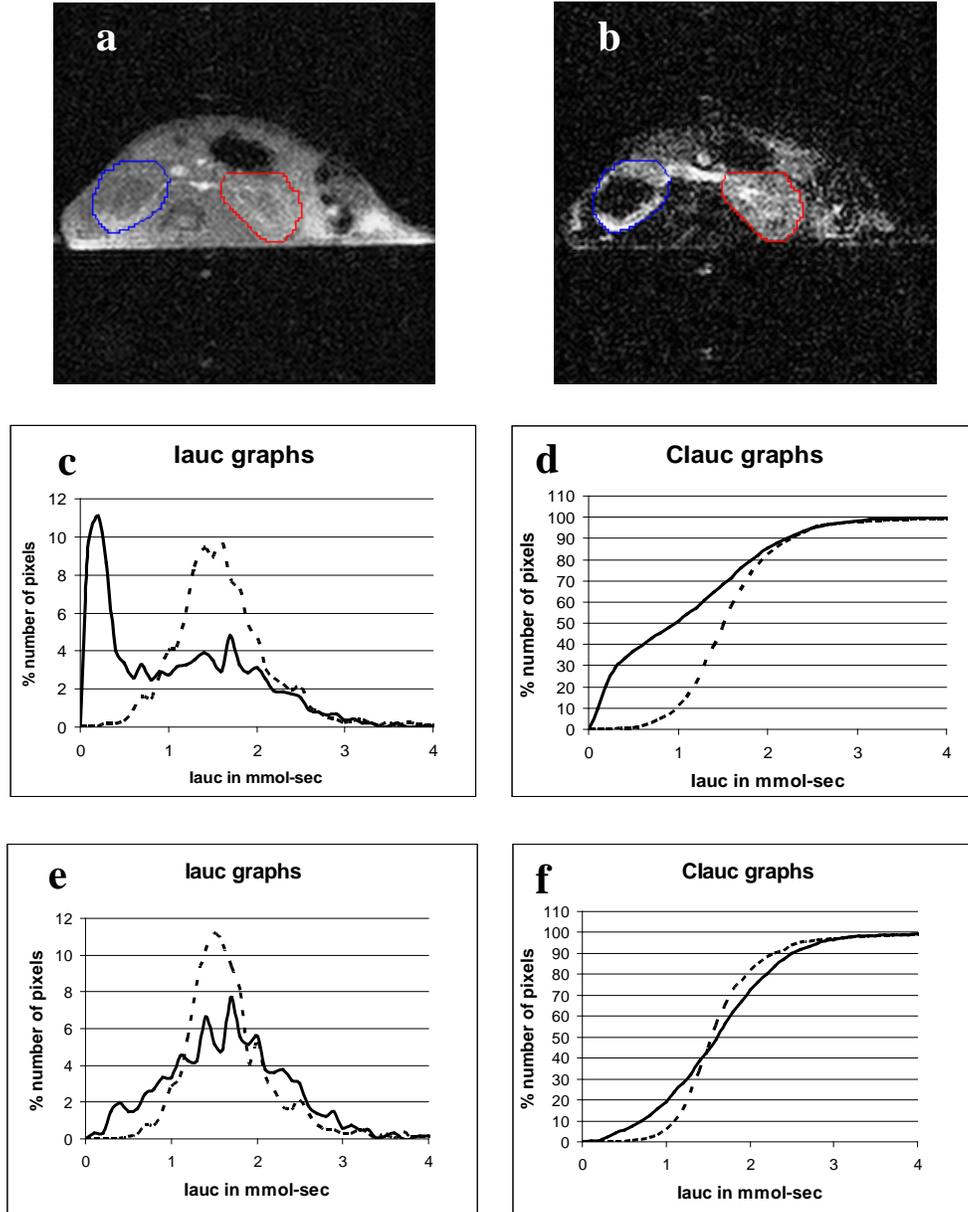
Figure 6.3: Threshold application to DCE-MRI images. Two ROI were plotted on the right tumor bearing kidney and the left normal kidney as shown in a) Dynamic DCE image, and b) Subtracted image. c) IAUC and d) CIAUC graphs before applying the threshold, IAUC graph shows a bimodal behavior resulting from noise, necrotic and active parts of the tumor (i.e., the selected ROI shown in b) leading to a false shift in the CIAUC graphs and smaller R50 values. e) IAUC and f) CIAUC graphs after applying the threshold. IAUC is more Gaussian after excluding the noise and the necrotic pixels from processing. Both necrotic and poorly vascularized parts of the tumor can be seen in the subtracted image. The solid line represents the kidney tumors and the dashed line represents the normal kidneys result.

113
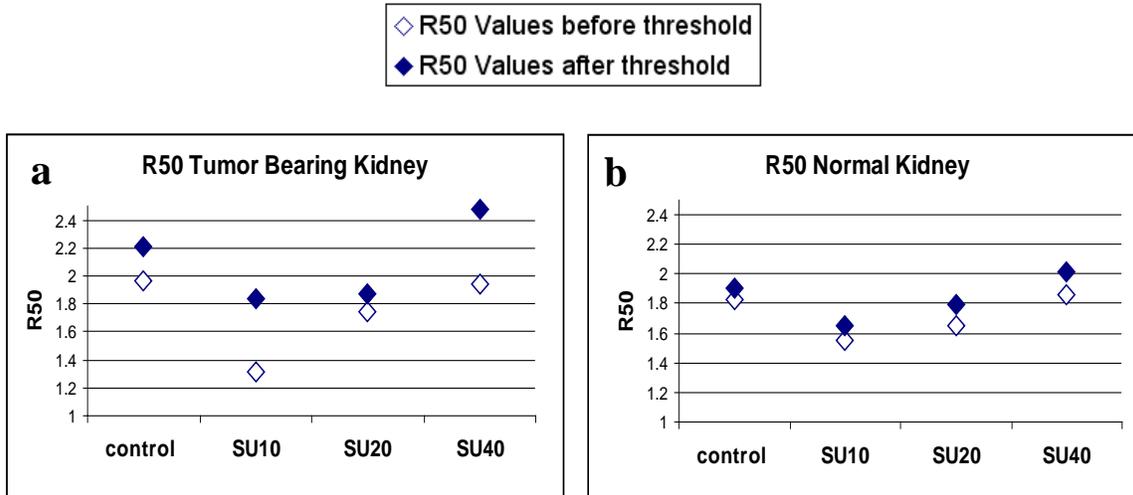
Figure 6.4: the R50 values with and without applying the threshold for a) the tumor bearing kidneys and b) the normal kidneys. The open diamonds represent the R50 values before applying threshold and the full diamonds represent the R50 values after applying threshold. Each point represents the mean of the R50 values for 3 mice per group.

FAP values	Normal Kidney	Tumor Kidney
control	0.85	0.73
SU10	0.83	0.63
SU20	0.56	0.81
SU40	0.79	0.6

Table 6.1: FAP values for the normal kidney and tumor kidney (We are showing one mouse per group).

Using the filtered DCE data, the uptake of Gd-DTPA was compared between the four different groups (SU10, SU20, SU40 and control) by evaluating the R50 and the NR50 values. We found that the contrast agent uptake by the tumor bearing kidney treated with a intermediate dose of 20 mg/kg/day was higher compared to the normal kidneys in untreated mice (control) or those treated with high and low doses of sunitinib, i.e., SU 40 and SU10 with slower kinetics of wash out (Hillman et al., 2009). However, in these mice treated with SU20, both tumor-bearing

kidneys and normal kidneys have similar kinetics of uptake and wash out of Gd-DTPA. This is

confirmed also from the NR50 values (Figure 6.5) (Hillman et al., 2009).
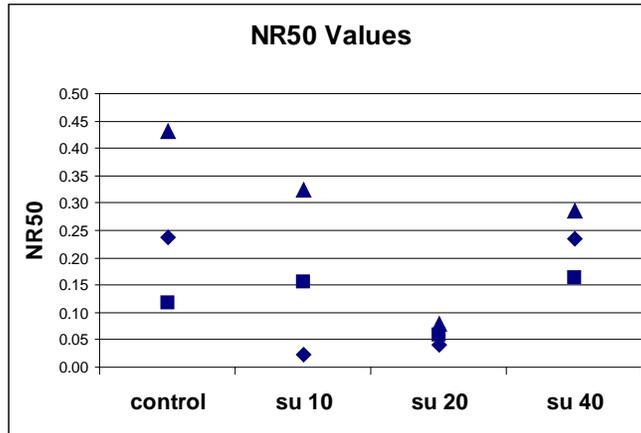
Figure 6.5: NR50 values were calculated by normalizing the tumor-bearing kidney to the normal kidneys. Note that treatment with SU 20mg/kg/day improved tumor perfusion with comparable CA uptake as the normal kidneys. However, in control and mice treated by SU40 or SU10, the tumor uptakes more CA compared to the normal kidneys (Hillman et al., 2009). The figure shows 3 mice per group.

6.4.2 Kidney Regional Analysis

DCE parametric maps were used to evaluate the vascular kinetics of different kidney

regions. Figure 6.6 shows the middle slice of the DCE parametric maps of a normal mouse (i.e.,

has no RCC injection). DCE parametric maps were color coded in order to see variation more

easily. The two kidneys appear consistence in the parametric maps. Nevertheless, the kidneys

main regions also clearly appear. Normal kidneys have 4 main regions: the cortex, the medulla,

the calyx and the pelvis. From the DCE parametric maps, we see that the calyx-pelvis region has

high AUC, Pslope, PEAK and Nslope values indicated by the red color. AUCtp has a high values

inside the pelvis region, which might indicate that the slice has cut the renal artery. TTP values are shorter in the kidneys comparing to the surrounding tissues.
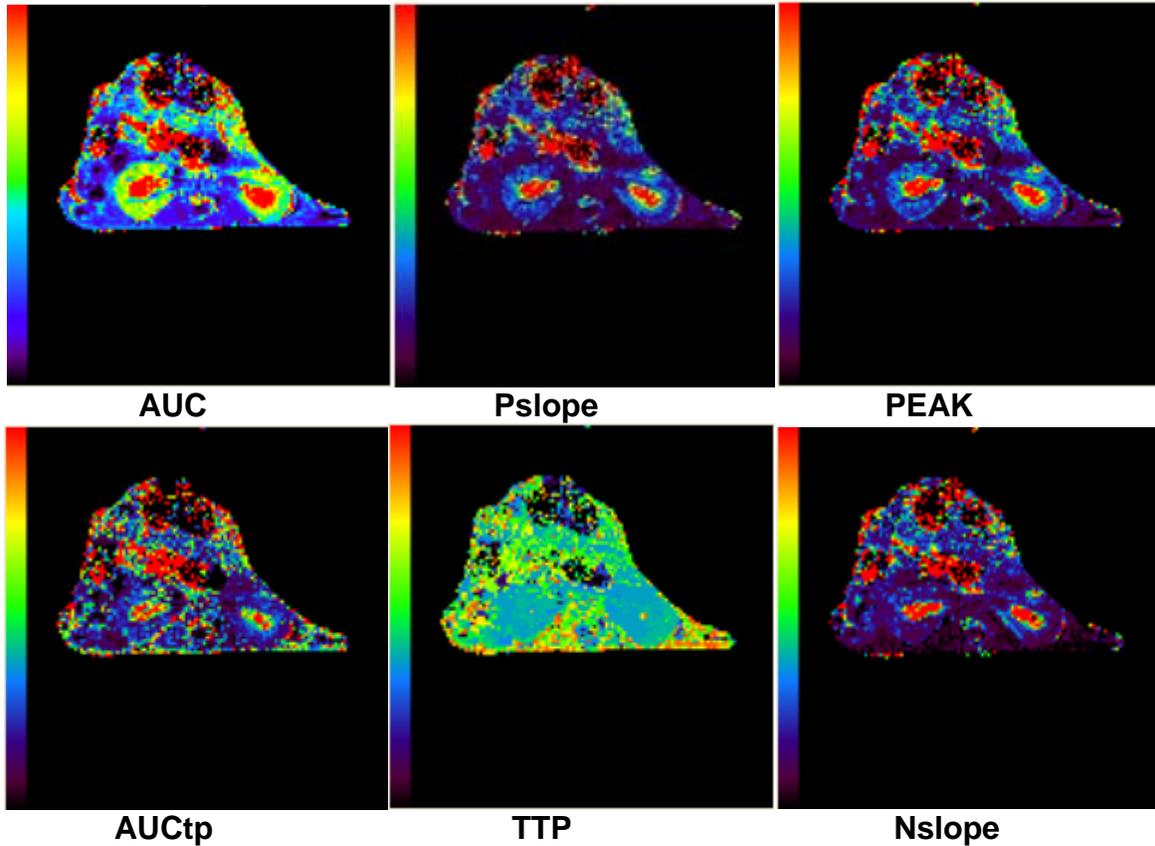
Figure 6.6: the DCE parametric maps. Mouse was imaged by DCE-MRI for 30 time points at 7-second intervals. Baseline images were collected for the first during 10 time points before Gd contrast agent injection. At time point 10, Gd was injected in the tail vein, and images were collected for 20 more time points. The DCE parametric maps are obtained from C(t) curves. The total contrast agent uptake (AUC), rate of uptake (Pslope), peak concentration (PEAK), uptake to the peak (AUCtp), time to peak (TTP) and the rate of Gd clearance (Nslope) in the kidney ROIs are shown.

Figure 6.7 shows the DCE parametric maps for a control mouse. The parametric maps succeed to differentiate the tumor core from its periphery. Tumor core (in the right kidney) has low AUC, Pslope, PEAK and Nslope values indicated by the dark blue color in the parametric

maps as well as a relatively long TTP values. This suggests that the core of the tumor has poor

blood supply. On the other hand, the periphery of the tumor has a high AUC value indicating a

high blood supply. Looking at the normal kidney results, we can see that calyx-pelvis region has

a similar AUC, Pslope and PEAK values compared to the periphery of the tumor-bearing kidney

but a higher Nslope values. This might suggest that the normal kidney is functioning normally.
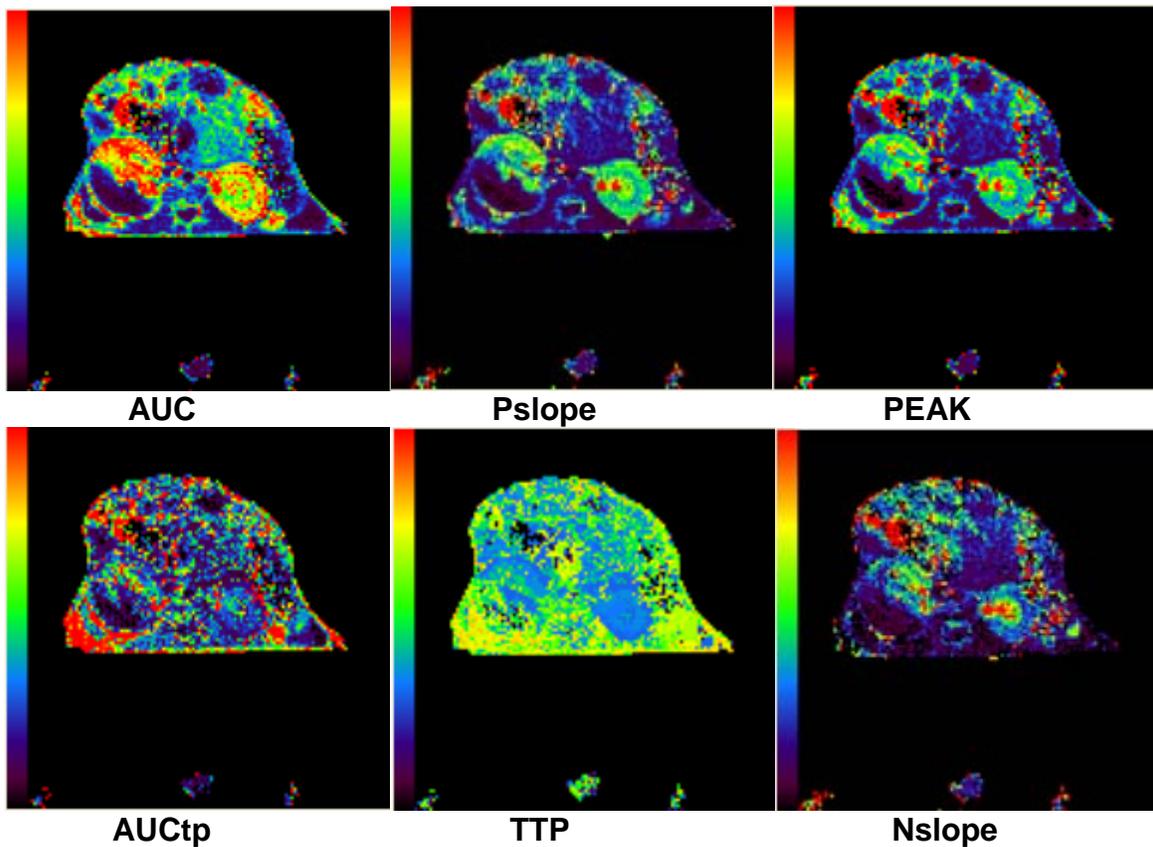
Figure 6.7: DCE-MRI of KCI-18 KTs. Mouse bearing established tumors in the right kidneys was treated every day for 7 days with vehicle only (control). Then, the mouse was imaged by DCE-MRI for 30 time points at 7-second intervals. Baseline images were collected for the first during 10 time points before Gd contrast agent injection. At time point 10, Gd was injected in the tail vein, and images were collected for 20 more time points. The DCE parametric maps are obtained from C(t) curves. The total contrast agent uptake (AUC), rate of uptake (Pslope), peak concentration (PEAK), uptake to the peak (AUCtp), time to peak (TTP) and the rate of Gd clearance (Nslope) in the kidney ROIs are shown.(control 164-march 2010)

To quantify the regional response after sunitinib treatment in mice, two ROIs representing the periphery and core of kidney tumors and two ROIs representing the cortex and medulla of normal kidneys were drawn separately on AUC, Pslope, PEAK, AUCtp, TTP and Nslope maps for each mouse. Each ROI was quantified and the results are shown as mean ± SD in Table 6.2. Looking at the values from parametric quantifications of the control mice, we notice that the Gd uptake, Pslope, PEAK, TTP, AUCtp and Nslope by the tumor periphery is higher than that value by the normal cortex. However, the tumor core have lower Gd uptake, Pslope, PEAK, AUCtp and Nslope values compared to the normal medulla. These finding agrees with the pathology of RCC.

The results were compared between the four different groups (SU10, SU20, SU40 and control). The low dose of SU10 in the kidney tumors had no effect in the core of the tumor compared to the control mice. SU20 and SU40 treatment doses were found to enhance the blood perfusion and clearance of the core and only SU40 dose was found to increase the Pslope, PEAK and Nslope in the tumor periphery (see Table 6.2-a). In the normal kidneys, mice treated with SU10 and SU20 have almost the same AUC, Pslope and PEAK compared to control mice normal kidneys. However, increasing the treatment dose to 40 mg/kg/day affects the Gd-DTPA Pslope, PEAK and Nslope in the cortex and the medulla of normal kidneys compared to the control mice normal kidneys (see Table 6.2-b). These findings from Table 6.2 were confirmed by histological observations of tissues showing that using SU40 as a treatment dose caused tumor vessel destruction associated with hemorrhages in tumor-bearing kidneys and dilatation of blood vessels in normal kidneys (Hillman et al., 2009). Mice treated with SU20 had more regularized and thinner vessels in kidney tumors and mild dilatation in a few vessels in normal kidneys. In contrast, mice treated with SU10 had enlarged abnormal vessels in tumor-bearing kidneys and

regular vessels in normal kidneys similar to the findings from control mice (Hillman et al., 2009).

a) Tumor Bearing Kidneys:

Parametric maps: Region:		AUC mmol.ms	Pslope mmol/ms	PEAK 10^{-4} mmol	TTP ms	AUCtp 10^{-3} mmol.ms	Nslope mmol/ms
Periphery	Control	0.23±0.12	26± 3	7 ± 0.4	110±10	25± 4	16±3
	SU10	0.18±0.06	21± 6	6 ± 2	132±17	31±11	9±3
	SU20	0.18±0.03	20 ± 2	5± 0.6	99±4	14±2	11±0.6
	SU40	0.22±0.04	37± 10	9 ± 3	103±11	27±10	25±9
Core	Control	0.06± 0.03	10 ± 1	2± 0.6	153±2	15±4	5±0.3
	SU10	0.05 ± 0.02	6 ± 1	2 ± 0.7	146±15	14±8	3±0.2
	SU20	0.10 ± 0.00	13± 6	3 ± 0.8	130±29	16±5	9±6
	SU40	0.10± 0.02	18 ± 10	5± 2.5	142±22	25±4	12±10

b) Normal Kidneys:

Parametric maps: Region:		AUC mmol.ms	Pslope mol/ms	PEAK 10^{-3} mmol	TTP ms	AUCtp 10^{-3} mmol.ms	Nslope mmol/ms
Cortex	Control	0.15± 0.05	22 ± 0.1	5 ± 0.2	99±4	17±3	14±0.1
	SU10	0.16± 0.08	18 ± 0.8	4 ± 0.4	112±14	18±6	9±1
	SU20	0.17 ± 0.02	19 ± 2	4 ± 0.5	100±3	14±1	11±2
	SU40	0.18 ± 0.03	33 ± 12	7 ± 3	94±6	19±8	20±11
Medulla	Control	0.17 ± 0.09	16± 0.2	5± 0.3	122±17	23±7	11±3
	SU10	0.13 ± 0.07	13 ± 0.8	3 ± 0.5	131±13	21± 8	7±1
	SU20	0.14 ± 0.01	14± 0.3	4 ± 0.3	108±8	15±3	10±2
	SU40	0.13 ± 0.01	20 ± 6	5 ± 1	102±3	16±3	13±3

Table 6.2: DCE characteristic table. a) two ROIs representing the periphery and core of kidney tumors and b) two ROIs representing the cortex and medulla of normal kidneys were drawn, separately, on AUC, Pslope, PEAK, AUCtp, TTP and Nslope maps for each mouse. Each ROI was quantified and the results are shown as mean ± SD.

Blood Volume Fraction (λ)

For some cases the renal artery was clearly seen in the DCE images. These case where used to evaluate the blood volume fraction (λ). The result showed an increase of the blood volume fraction for the control kidney tumor compared to the normal kidney. However, for mice treated with dose of 20 mg/kg/day and 10 mg/kg/day the blood volume fraction of both kidneys appear to be the same (see Table 6.3). Interestingly, for the mouse treated with SU 40, we noticed a dramatical increase in the blood volume fraction for both normal and tumor-bearing kidneys (see Table 6.3).

λ values	Tumor Kidney	Normal Kidney
control	0.80	0.50
SU10	0.52	0.49
SU20	0.57	0.59
SU40	0.98	0.94

Table 6.3: blood volume fraction (λ) values for the normal kidney and kidney tumor. The table show the result for one mouse per group where the renal artery where clear.

6.4.3 Full Width at the Half Maximum (FWHM)

We found that the tumor-bearing kidneys in control, SU40 and SU10 treated mice had a very broad IAUC as indicated by the FWHM values; it exceeds 2 mmol.sec (Figure 6.8-a). For normal kidneys, FWHM ranges between 1.5 and 2 mmol.sec for all mice groups except the SU40 treated group (Figure 6.8-b). Increasing the sunitinib treatment dosage to 40 mg/kg/day, both normal and tumor-bearing kidneys have higher FWHM values. This might be explained by the increased permeability and poor clearance of the blood vessels in the tumor bearing kidneys

compared to the control normal kidneys or other treated normal kidneys with dosages of 10 and

20 mg/kg/day of sunitinib. With SU20 mg/kg/day, the FWHM became narrower and behaved

more like normal kidneys in both control and SU10-treated mice (Figure 6.8-a & 6.8-b).
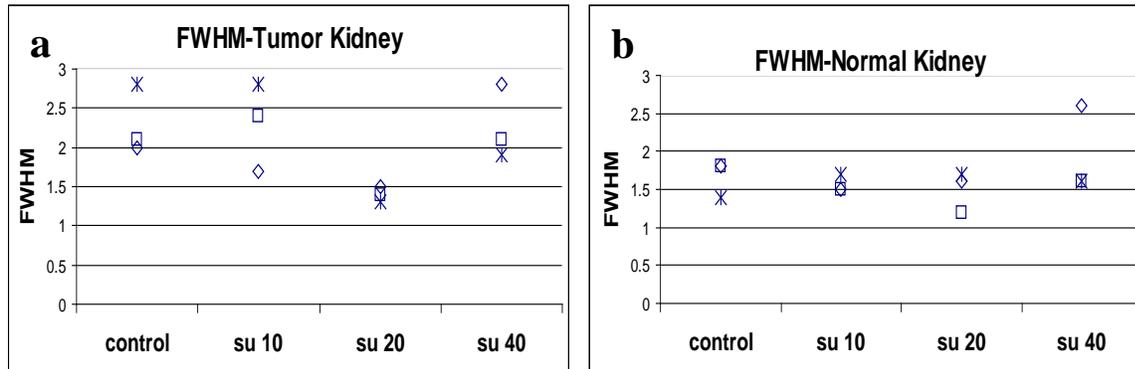
Figure 6.8: FWHM results. FWHM values for a) tumor-bearing kidneys and b) normal kidneys. Notice that higher FWHM values for control, SU40 and SU10 mice compared to the SU20 mice in kidney tumors. In normal kidneys FWHM almost stayed at the same range between different groups of treatment.

6.5 Discussion

Dynamic MRI scans with injection of GD-DTPA are considered to be a robust method used to study diseases that alter blood perfusion and tissue micro-vascular parameters of human tissue. However, tumor heterogeneity is one of the factors that lead to DCE results variation from center to another. The presence of necrotic cells in the tumor-bearing kidneys greatly affects the R50 values and shifts the CIAUC curves more to the left compared to the R50 values after applying the threshold as seen in Figure 5.3-d and Figure 5.3-f. The combined use of thresholding both the original DCE data and subtracted data proved to be a useful tool to differentiate between noise thresholded pixels from necrotic thresholded pixels. However, the noise in the subtracted images can be lowered by averaging the images acquired before Gd injection and subtracted it from a set of images after Gd injection instead of taking only one time point set of images and subtracted it from a set of images after Gd injection. FAP provided a new parameter to quantify the effect of sunitinib treatment on RCC tumors. Cases with high FAP for the normal kidneys will be more trusted than cases with low FAP. Higher FAP in the normal kidneys' region indicates that more pixels will be considered as active pixels and included in further analysis and less noisy pixels will be excluded. Hence, FAP of the tumor ROI will give an indication of the necrotic part percentage of the tumor compared to its active part. After drug treatment, the vessels may be affected in a way that changes the tissue which took up Gd and hence affect FAP values. Therefore, FAP measurement is expected to give an indication of drug effects on the tumor, where lower FAP indicates a more necrotic and less active tumor and a higher FAP, closer to 1, indicates a high percentage of active tumor cells compared to necrotic cells inside the ROI.

The newly developed DCE parametric maps are used to study the effect of sunitinib treatment on the main regions of the kidney. The main function of the kidney is to maintain homeostasis or equilibrium between internal volume and electrolyte status and that of environmental influence, diet and intake. It has two main regions: the cortex and the medulla that function to maintain the intra and extracellular fluid status at a constant rate despite the wide variety of daily fluid and electrolyte intake. Understanding the antiangiogenic treatment effects on kidney tissue might further help to better schedule treatment or better propose new treatment combinations. Our result on the pre-clinical RCC tumor model demonstrates that DCE parametric maps have the potential to assess the effect of antiangiogenic drugs on blood flow and vascular changes in tumors as well as in normal tissues by creating a characteristic table that describes the contrast agent uptake and the washout behavior of the tumor and normal tissue. From quantifying the DCE parametric maps, we noticed that SU40 had a dramatic effect on Pslope and Nslope values in both the cortex and medulla of normal kidneys compared to those values for normal kidneys in control mice. These results indicate that this high dose causes significant vascular damage. On the other hand, the SU20 data from tumor-bearing kidney showed results similar to that of a healthy normal kidney, where both Pslope and Nslope values of tumor periphery and core return to similar values as seen for the cortex and medulla of the normal kidneys in control mice. Looking at results from normal kidneys treated with SU20, we see almost no effect on the Pslope and Nslope values compared to the control mice values, indicating that this dose may be safer and regularizes the tumor vessels. We also noticed that SU40 has a greater effect on the cortex compared to the medulla of normal kidneys; this agrees with the fact there is a higher blood supply in the kidney cortex compared to the medulla.

Interestingly, from SU20 data, the AUCtp value of the tumor periphery is back in the range of AUCtp values for normal kidneys of all mice, but still lower in the tumor core. This might present more proof supporting the hypothesis that blood vessels trim the use of SU20 as a treatment dose. For control, SU10 and SU40 AUCtp values are high in the tumor periphery which agrees again with the histological finding of highly vascularized areas in control and SU10 treated mice and hemorrhage in SU40 treated mice (Hillman et al., 2009).

As we showed earlier, FWHM values for the mice treated with SU20 return to the normal range; this agrees with the histology result and supports our hypothesis regarding vessel trimming as has been shown in our previously published results (Hillman et al., 2009). FWHM measures of the IAUC curves may prove to be a useful indirect measure of vessel leakiness where it appears to be related to Gd uptake and washout (i.e., Pslope and Nslope) inside the ROI. FWHM studies the effects of drug treatment over all active pixels in the selected ROI and not only one pixel.

The new DCE parameters introduced here (i.e., FAP, AUCtp, Nslope and FWHM) provides further guidance as to what could be considered normal versus abnormal tissue response to antiangiogenic therapy. These measures are expected to help in understanding treatment effects throughout the kidney which might help anticipate problems that patients might develop after treatment and try to provide them with a suitable solution. Regional analysis using DCE parametric maps has the potential to decrease the effect of tumor heterogeneity on DCE results and hence, enhances DCE reproducibility. Another advantage for DCE parametric maps over DCE model free analysis is that model free analyses are time dependant and the results will depend on the number of the time points included for further analysis. Moreover, in model free analysis, fixed number of time points is included for processing for all the cases which might

lead to lose each case privacy especially in very functionally important areas such as the kidneys. On the other hand, the measurements derived from the DCE parametric maps can quantify the physiological vascular changes in tissue are independent from integration time points. We think that regional analysis using DCE parametric maps should be considered by other centers when testing new antiangiogenic drugs.

Estimating the blood volume fraction (λ) from the AUC_{tp} map can be considered as a step closer to a dynamic susceptibility contrast (DSC) like analysis of tissue permeability like properties.

In conclusion, this newly introduced DCE characteristic table has the potential to quantify the effect of antiangiogenic drug treatment, such as sunitinib, throughout the region of interest and should lead to a clear improvement in the ability of DCE-MRI as a quantifying method to study the tumor vasculature and other hemodynamic properties.

Chapter Seven

Conclusion and Future Directions:

Magnetic resonance imaging with an injection of gadolinium chelates is considered to be the most robust method used to study diseases that affect blood perfusion and tissue micro-vascular parameters of human tissue. Observation of contrast enhancement is typically achieved using a dynamic imaging technique where a contrast agent is injected during the acquisition of a dynamic image set and can give quantitative information about tissue hemodynamic parameters such as blood volume, blood flow and tissue permeability.

The new algorithm we introduced in this project is to use a fixed T1(0) value. This approach will provide us with more reproducible DCE results. This algorithm has also enhanced the ability of DCE-MRI as a tool to be able to decide the best treatment dose among a number of different doses of the antiangiogenic drug, sunitinb, which can be mistakenly used in a high dose for tumor treatment and can harm normal healthy tissues. Also in this project we introduced a number of new parameters including fraction of active pixels (FAP), contrast agent uptake to the peak (AUCtp), time to peak concentration (TTP), washout slope (Nslope) and full width half maximum (FWHM). These new parameters are independent of the integration time points but on the other hand can be used to estimate Toft's parameters, such as K^{trans} and K_{ep} when AIF is not available.

Scheduling for cancer treatment is one of the important tasks oncologists face. Understanding effects of antiangiogenic drugs on the tumor vasculature can help in better planning for treatment regimens. In chapter two, we discussed the tumor angiogenesis process where abnormal blood vessels start proliferation. These blood vessels are leaky and enlarged compared to normal blood vessels. The defects in tumor blood vessels might lead to

elevated interstitial tissue pressure; impaired blood supply; and decreased oxygen supply, in the tumors. These factors could lead to a decrease of the efficacy chemotherapy and radiotherapy.

As we investigated in chapter four, DCE-MRI succeeded in determining the best treatment dose for RCC tumors with less impact on healthy kidney tissues. These results opened new avenues for further investigations with the pre-selected sunitinb dose (i.e., 20 mg/kg/day) combined with other cytotoxic drugs and/or radiotherapy. From our study we found that DCE was a reliable tool to monitor vascular changes induced by various doses of suntinib in kidney tumors as well as in normal kidney tissue. We showed that a treatment of a daily sunitinb dose of 20 mg/kg/day mildly affected the normal vessels but caused better tumor perfusion of contrast agent and decreased vascular permeability in agreement with histological observations of the thinning and regularization of tumor vessels.

We have established the conditions for the combination of antiangiogenic therapy with sunitinib and cytoxic therapy with gemcitabine (a chemotherapy drug) that result in significant long-lasting anti-tumor response. We also used the idea of blood vessel normalization that is, using the antiangiogenic drug, sunitinb, and combining it with radiotherapy; we hypothesize that blood vessels trimming can enhance oxygen delivery to the tumor and hence enhance the radiotherapy treatment results (work under progress).

Moreover, our future directions are to use these DCE-parametric maps (i.e, Pslope, Peak, TTP, AUCtp and FWHM) as a different mean to represent the usual K^{trans} and K_{ep} values that is extracted from Toft's Model using a special Taylor series expansion approach. This will be very beneficial when AIF information is not available.

In conclusion, the results of this research should lead to a clear improvement in the ability of MRI as a quantifying method to quantify tumor vasculature and other hemodynamic properties.

REFERENCES

Abrams, T.J., Murray, L.J., Pesenti, E., Holway, V.W., Colombo, T., Lee, L.B., Cherrington, J.M., Pryer, N.K., 2003. Preclinical evaluation of the tyrosine kinase inhibitor SU11248 as a single agent and in combination with "standard of care" therapeutic agents for the treatment of breast cancer. Mol Cancer Ther 2(14578466), 1011-1021.

Ah-See, M.-L.W., Makris, A., Taylor, N.J., Harrison, M., Richman, P.I., Burcombe, R.J., Stirling, J.J., d'Arcy, J.A., Collins, D.J., Pittam, M.R., Ravichandran, D., Padhani, A.R., 2008. Early changes in functional dynamic magnetic resonance imaging predict for pathologic response to neoadjuvant chemotherapy in primary breast cancer. Clin Cancer Res 14(18927299), 6580-6589.

Amato, R.J., Khan, M., 2008. A phase I clinical trial of low-dose interferon-alpha-2A, thalidomide plus gemcitabine and capecitabine for patients with progressive metastatic renal cell carcinoma. Cancer Chemother Pharmacol 61(17701037), 1069-1073.

Asaumi, J., Yanagi, Y., Hisatomi, M., Matsuzaki, H., Konouchi, H., Kishi, K., 2003. The value of dynamic contrast-enhanced MRI in diagnosis of malignant lymphoma of the head and neck. Eur J Radiol 48(2), 183-187.

Ashkenazi, A., Herbst, R.S., 2008. To kill a tumor cell: the potential of proapoptotic receptor agonists. The Journal of Clinical Investigation 118(6), 12.

Barbour, A., Gotley, D.C., 2003. Current concepts of tumour metastasis. Ann Acad Med Singapore 32(2), 176-184.

Berges, R., Isaacs, J.T., 1993. Programming events in the regulation of cell proliferation and death. Clin Chem 39(2), 356-361.

Bhooshan, N., Giger, M.L., Jansen, S.A., Li, H., Lan, L., Newstead, G.M., 2010. Cancerous breast lesions on dynamic contrast-enhanced MR images: computerized characterization for image-based prognostic markers. Radiology 254(3), 680-690.

Billemont, B., Meric, J.B., Izzedine, H., Taillade, L., Sultan-Amar, V., Rixe, O., 2007. [Angiogenesis and renal cell carcinoma]. Bull Cancer 94 Spec No, S232-240.

Bocci G, Danesi R, Marangoni G, Fioravanti A, Boggi U, Esposito I, Fasciani A, Boschi E, Campani D, Bevilacqua G, Mosca F, TM, D., 2004. Antiangiogenic versus cytotoxic therapeutic approaches to human pancreas cancer: an experimental study with a vascular endothelial growth factor receptor-2 tyrosine kinase inhibitor and gemcitabine. Eur. J Pharmacol 498, 10.

Bradley, W.G. Fundamentals Of MRI: Part I.

Britten, C.D., Kabbinavar, F., Hecht, J.R., Bello, C.L., Li, J., Baum, C., Slamon, D., 2008. A phase I and pharmacokinetic study of sunitinib administered daily for 2 weeks, followed by a 1-week off period. Cancer Chemother Pharmacol 61(17505827), 515-524.

Browder, T., Butterfield, C.E., Kraling, B.M., Shi, B., Marshall, B., O'Reilly, M.S., Folkman, J., 2000. Antiangiogenic scheduling of chemotherapy improves efficacy against experimental drug-resistant cancer. Cancer Res 60(10766175), 1878-1886.

Burstein, H.J., Elias, A.D., Rugo, H.S., Cobleigh, M.A., Wolff, A.C., Eisenberg, P.D., Lehman, M., Adams, B.J., Bello, C.L., DePrimo, S.E., Baum, C.M., Miller, K.D., 2008. Phase II study of sunitinib malate, an oral multitargeted tyrosine kinase inhibitor, in patients with metastatic breast cancer previously treated with an anthracycline and a taxane. J Clin Oncol 26(18347007), 1810-1816.

Caravan, P., Ellison, J.J., McMurry, T.J., Lauffer, R.B., 1999. Gadolinium(III) Chelates as MRI Contrast Agents: Structure, Dynamics, and Applications. Chem. Rev. 99, 60.

Cavallaro, U., Christofori, G., 2000. Molecular Mechanisms of Tumor Angiogenesis and Tumor Progression. Journal of Neuro-Oncology 50, 8.

Cha, S., 2004. Perfusion MR imaging of brain tumors. Top Magn Reson Imaging 15(5), 279-289.

Checkley, D., Tessier, J.J., Kendrew, J., Waterton, J.C., Wedge, S.R., 2003. Use of dynamic contrast-enhanced MRI to evaluate acute treatment with ZD6474, a VEGF signalling inhibitor, in PC-3 prostate tumours. Br J Cancer 89(14612898), 1889-1895.

Chu, T.F., Rupnick, M.A., Kerkela, R., Dallabrida, S.M., Zurakowski, D., Nguyen, L., Woulfe, K., Pravda, E., Cassiola, F., Desai, J., George, S., Morgan, J.A., Harris, D.M., Ismail, N.S., Chen, J.-H., Schoen, F.J., Van den Abbeele, A.D., Demetri, G.D., Force, T., Chen, M.H., 2007. Cardiotoxicity associated with tyrosine kinase inhibitor sunitinib. Lancet 370(18083403), 2011-2019.

Craciunescu, O.I., Blackwell, K.L., Jones, E.L., Macfall, J.R., Yu, D., Vujaskovic, Z., Wong, T.Z., Liotcheva, V., Rosen, E.L., Prosnitz, L.R., Samulski, T.V., Dewhirst, M.W., 2009. DCE-MRI parameters have potential to predict response of locally advanced breast cancer patients to neoadjuvant chemotherapy and hyperthermia: a pilot study. Int J Hyperthermia 25(19657852), 405-415.

Cron, G.O., Santyr, G., Kelcz, F., 1999. Accurate and Rapid Quantitative Dynamic Contrast-Enhanced Breast MR Imaging Using Spoiled Gradient-Recalled Echoes and Bookend T1 Measurements. Magnetic Resonance in Medicine 42, 8.

Cutajar, M., Mendichovszky, I.A., Tofts, P.S., Gordon, I., 2009. The importance of AIF ROI selection in DCE-MRI renography: Reproducibility and variability of renal perfusion and filtration. Eur J Radiol.

Dale, B.M., Jesberger, J.A., Lewin, J.S., Hillenbrand, C.M., Duerk, J.L., 2003. Determining and optimizing the precision of quantitative measurements of perfusion from dynamic contrast enhanced MRI. J Magn Reson Imaging 18(5), 575-584.

Desai, A.A., Vogelzang, N.J., Rini, B.I., Ansari, R., Krauss, S., Stadler, W.M., 2002. A high rate of venous thromboembolism in a multi-institutional phase II trial of weekly intravenous gemcitabine with continuous infusion fluorouracil and daily thalidomide in patients with metastatic renal cell carcinoma. Cancer 95(12365009), 1629-1636.

Ebos, J.M.L., Lee, C.R., Christensen, J.G., Mutsaers, A.J., Kerbel, R.S., 2007. Multiple circulating proangiogenic factors induced by sunitinib malate are tumor-independent and correlate with antitumor efficacy. Proc Natl Acad Sci U S A 104(17942672), 17069-17074.

Faulkner, W. (1996). Basic Principles of MRI, OutSource, Inc.

Fidler, I.J., 1978. Tumor heterogeneity and the biology of cancer invasion and metastasis. Cancer Res 38(9), 2651-2660.

Fisher, E.R., Fisher, B., 1967. Recent observations on concepts of metastasis. Arch Pathol 83(4), 321-324.

Flanigan, R.C., Salmon, S.E., Blumenstein, B.A., Bearman, S.I., Roy, V., McGrath, P.C., Caton, J.R., Munshi, N., Crawford, E.D., 2001. Nephrectomy followed by interferon alfa-2b compared with interferon alfa-2b alone for metastatic renal-cell cancer. N Engl J Med 345(11759643), 1655-1659.

Folkman, J., 2006. Angiogenesis. Annu Rev Med 57, 1-18.

Furman-Haran, E., Grobgeld, D., Kelcz, F., Degani, H., 2001. Critical Role of Spatial Resolution in Dynamic Contrast-Enhanced Breast MRI. JOURNAL OF MAGNETIC RESONANCE IMAGING 13, 6.

Galban, C.J., Chenevert, T.L., Meyer, C.R., Tsien, C., Lawrence, T.S., Hamstra, D.A., Junck, L., Sundgren, P.C., Johnson, T.D., Ross, D.J., Rehemtulla, A., Ross, B.D., 2009. The parametric response map is an imaging biomarker for early cancer treatment outcome. Nat Med 15(19377487), 572-576.

Galbraith, S.M., Lodge, M.A., Taylor, N.J., Rustin, G.J., Bentzen, S., Stirling, J.J., Padhani, A.R., 2002. Reproducibility of dynamic contrast-enhanced MRI in human muscle and tumours: comparison of quantitative and semi-quantitative analysis. NMR Biomed 15(2), 132-142.

Gan, H.K., Seruga, B., Knox, J.J., 2009. Sunitinib in solid tumors. Expert Opin Investig Drugs 18(6), 821-834.

Guo, J.Y., Reddick, W.E., 2009. DCE-MRI pixel-by-pixel quantitative curve pattern analysis and its application to osteosarcoma. J Magn Reson Imaging 30(1), 177-184.

Haacke, E., Brown, R., Thompson, M., Venkatesan, R. (1999). Magnetic Resonance Imaging.

Haacke, E.M., Filleti, C.L., Gattu, R., Ciulla, C., Al-Bashir, A., Suryanarayanan, K., Li, M., Latif, Z., DelProposto, Z., Sehgal, V., Li, T., Torquato, V., Kanaparti, R., Jiang, J., Neelavalli, J., 2007. New algorithm for quantifying vascular changes in dynamic contrast-enhanced MRI independent of absolute T1 values. Magn Reson Med 58(17763352), 463-472.

Haas, G.P., Hillman, G.G., 1996. Update on the Role of Immunotherapy in the Management of Kidney Cancer. Cancer Control 3(10764514), 536-541.

Hagmar, B., Ryd, W., Erkell, L.J., 1984. Why do tumors metastasize? An overview of current research. Tumour Biol 5(3-4), 141-149.

Hahn, O.M., Yang, C., Medved, M., Karczmar, G., Kistner, E., Karrison, T., Manchen, E., Mitchell, M., Ratain, M.J., Stadler, W.M., 2008. Dynamic contrast-enhanced magnetic resonance imaging pharmacodynamic biomarker study of sorafenib in metastatic renal carcinoma. J Clin Oncol 26(18824708), 4572-4578.

Haris, M., Gupta, R.K., Husain, M., Srivastava, C., Singh, A., Singh Rathore, R.K., Saksena, S., Behari, S., Husain, N., Mohan Pandey, C., Nath Prasad, K., 2008. Assessment of therapeutic response in brain tuberculomas using serial dynamic contrast-enhanced MRI. Clin Radiol 63(5), 562-574.

Hayes, C., Padhani, A.R., Leach, M.O., 2002. Assessing changes in tumour vascular function using dynamic contrast-enhanced magnetic resonance imaging. NMR Biomed 15(2), 154-163.

Hedley, M., Yan, H., 1992. Motion artifact suppression: a review of post-processing techniques. Magn Reson Imaging 10(4), 627-635.

Henderson, E., Rutt, B.K., Lee, T.-Y., 1998. Temporal sampling requirements for the tracer kinetics modeling of breast disease. Magnetic Resonance Imaging, 16(9), 17.

Hillman, G.G., Singh-Gupta, V., Zhang, H., Al-Bashir, A.K., Katkuri, Y., Li, M., Yunker, C.K., Patel, A.D., Abrams, J., Haacke, E.M., 2009. Dynamic contrast-enhanced magnetic resonance imaging of vascular changes induced by sunitinib in papillary renal cell carcinoma xenograft tumors. Neoplasia 11(9), 910-920.

Hillman, G.G., Wang, Y., Che, M., Raffoul, J.J., Yudelev, M., Kucuk, O., Sarkar, F.H., 2007. Progression of renal cell carcinoma is inhibited by genistein and radiation in an orthotopic model. BMC Cancer 7(17212824), 4-4.

Hillman, G.G., Wang, Y., Kucuk, O., Che, M., Doerge, D.R., Yudelev, M., Joiner, M.C., Marples, B., Forman, J.D., Sarkar, F.H., 2004. Genistein potentiates inhibition of tumor growth by radiation in a prostate cancer orthotopic model. Mol Cancer Ther 3(15486194), 1271-1279.

Huang, D., Ding, Y., Li, Y., Luo, W.-M., Zhang, Z.-F., Snider, J., Vandenbeldt, K., Qian, C.-N., Teh, B.T., 2010. Sunitinib acts primarily on tumor endothelium rather than tumor cells to inhibit the growth of renal cell carcinoma. Cancer Res 70(20103629), 1053-1062.

Huang, W., Fisher, P.R., Dulaimy, K., Tudorica, L.A., O'Hea, B., Button, T.M., 2004. Detection of breast malignancy: diagnostic MR protocol for improved specificity. Radiology 232(2), 585-591.

Hulka, C.A., Smith, B.L., Sgroi, D.C., Tan, L., Edmister, W.B., Semple, J.P., Campbell, T., Kopans, D.B., Brady, T.J., Weisskoff, R.M., 1995. Benign and malignant breast lesions: differentiation with echo-planar MR imaging. Radiology 197, 6.

Jain, R.K., 2001. Normalizing tumor vasculature with anti-angiogenic therapy: a new paradigm for combination therapy. Nat Med 7(11533692), 987-989.

Jain, R.K., 2005. Normalization of tumor vasculature: an emerging concept in antiangiogenic therapy. Science 307(15637262), 58-62.

Jemal, A., Siegel, R., Ward, E., Hao, Y., Xu, J., Murray, T., Thun, M.J., 2008. Cancer statistics, 2008. CA Cancer J Clin 58(18287387), 71-96.

Karahaliou, A., Vassiou, K., Arikidis, N.S., Skiadopoulos, S., Kanavou, T., Costaridou, L., 2010. Assessing heterogeneity of lesion enhancement kinetics in dynamic contrast-enhanced MRI for breast cancer diagnosis. Br J Radiol 83(988), 296-309.

Kerbel, R., Folkman, J., 2002. Clinical translation of angiogenesis inhibitors. Nat Rev Cancer 2(12360276), 727-739.

Kirsch, M., Schackert, G., Black, P.M., 2000. Anti-angiogenic treatment strategies for malignant brain tumors. Journal of Neuro-Oncology 50, 15.

Knopp, M.V., Giesel, F.L., Marcos, H., von Tengg-Kobligk, H., Choyke, P., 2001. Dynamic contrast-enhanced magnetic resonance imaging in oncology. Top Magn Reson Imaging 12(4), 301-308.

Kollmannsberger, C., Soulieres, D., Wong, R., Scalera, A., Gaspo, R., Bjarnason, G., 2007. Sunitinib therapy for metastatic renal cell carcinoma: recommendations for management of side effects. Can Urol Assoc J 1(18542784), 41-54.

Lam, J.S., Leppert, J.T., Figlin, R.A., Belldegrun, A.S., 2005. Role of molecular markers in the diagnosis and therapy of renal cell carcinoma. Urology 66(16194700), 1-9.

Laquente, B., Lacasa, C., Ginestà, M.M., Casanovas, O., Figueras, A., Galan, M., Ribas, I.G., Germà, J.R., Capellà, G., Vinals, F., 2008. Antiangiogenic effect of gemcitabine following metronomic administration in a pancreas cancer model. Mol Cancer Ther 7(18347150), 638-647.

LAUFFER, R.E., 1987. Paramagnetic Metal Complexes as Water Proton Relaxation Agents for NMR Imaging: Theory and Design. Chem. Rev. 87, 27.

Lee, C.G., Heijn, M., di Tomaso, E., Griffon-Etienne, G., Ancukiewicz, M., Koike, C., Park, K.R., Ferrara, N., Jain, R.K., Suit, H.D., Boucher, Y., 2000. Anti-Vascular endothelial

growth factor treatment augments tumor radiation response under normoxic or hypoxic conditions. Cancer Res 60(11034104), 5565-5570.

Levin, V.A., 1998. Chemotherapy for brain tumors of astrocytic and oligodendroglial lineage: The past decade and where we are heading. Neuro-Oncology (1), 12.

Loiselle, C., Rockhill, J., 2009. Radiation, Chemotherapy, and Symptom Management in Cancerrelated Cognitive Dysfunction. Current Pain & Headache Reports 13, 6.

Ludemann, L., Grieger, W., Wurm, R., Wust, P., Zimmer, C., 2005. Quantitative measurement of leakage volume and permeability in gliomas, meningiomas and brain metastases with dynamic contrast-enhanced MRI. Magn Reson Imaging 23(8), 833-841.

Ludemann, L., Warmuth, C., Plotkin, M., Forschler, A., Gutberlet, M., Wust, P., Amthauer, H., 2009. Brain tumor perfusion: comparison of dynamic contrast enhanced magnetic resonance imaging using T1, T2, and T2* contrast, pulsed arterial spin labeling, and H2(15)O positron emission tomography. Eur J Radiol 70(3), 465-474.

Ma, J., Waxman, D.J., 2008. Combination of antiangiogenesis with chemotherapy for more effective cancer treatment. Mol Cancer Ther 7(12), 15.

Marzola, P., Degrassi, A., Calderan, L., Farace, P., Nicolato, E., Crescimanno, C., Sandri, M., Giusti, A., Pesenti, E., Terron, A., Sbarbati, A., Osculati, F., 2005. Early antiangiogenic activity of SU11248 evaluated in vivo by dynamic contrast-enhanced magnetic resonance imaging in an experimental model of colon carcinoma. Clin Cancer Res 11(16115922), 5827-5832.

McAllister, R.M., 1965. VIRUSES AND CANCER. Calif Med 102, 344-352.

Mehta, M.P., Tomé, W.A., Gustavo H. Olivera, P., 2000. Radiotherapy for Brain Tumors. Current Oncology Reports 2, 7.

Mendel, D.B., Laird, A.D., Xin, X., Louie, S.G., Christensen, J.G., Li, G., Schreck, R.E., Abrams, T.J., Ngai, T.J., Lee, L.B., Murray, L.J., Carver, J., Chan, E., Moss, K.G., Haznedar, J.O., Sukbuntherng, J., Blake, R.A., Sun, L., Tang, C., Miller, T., Shirazian, S., McMahon, G., Cherrington, J.M., 2003. In vivo antitumor activity of SU11248, a novel tyrosine kinase inhibitor targeting vascular endothelial growth factor and platelet-derived growth factor receptors: determination of a pharmacokinetic/pharmacodynamic relationship. Clin Cancer Res 9(12538485), 327-337.

Motzer, R.J., Bander, N.H., Nanus, D.M., 1996. Renal-cell carcinoma. N Engl J Med 335(8778606), 865-875.

Motzer, R.J., Hutson, T.E., Tomczak, P., Michaelson, M.D., Bukowski, R.M., Oudard, S., Negrier, S., Szczylik, C., Pili, R., Bjarnason, G.A., Garcia-del-Muro, X., Sosman, J.A., Solska, E., Wilding, G., Thompson, J.A., Kim, S.T., Chen, I., Huang, X., Figlin, R.A., 2009. Overall survival and updated results for sunitinib compared with interferon alfa in patients with metastatic renal cell carcinoma. J Clin Oncol 27(19487381), 3584-3590.

Motzer, R.J., Hutson, T.E., Tomczak, P., Michaelson, M.D., Bukowski, R.M., Rixe, O., Oudard, S., Negrier, S., Szczylik, C., Kim, S.T., Chen, I., Bycott, P.W., Baum, C.M., Figlin, R.A., 2007. Sunitinib versus interferon alfa in metastatic renal-cell carcinoma. N Engl J Med 356(17215529), 115-124.

Motzer, R.J., Michaelson, M.D., Redman, B.G., Hudes, G.R., Wilding, G., Figlin, R.A., Ginsberg, M.S., Kim, S.T., Baum, C.M., DePrimo, S.E., Li, J.Z., Bello, C.L., Theuer, C.P., George, D.J., Rini, B.I., 2006. Activity of SU11248, a multitargeted inhibitor of vascular endothelial growth factor receptor and platelet-derived growth factor receptor, in patients with metastatic renal cell carcinoma. J Clin Oncol 24(16330672), 16-24.

Murase, K., 2004. Efficient method for calculating kinetic parameters using T1-weighted dynamic contrast-enhanced magnetic resonance imaging. Magn Reson Med 51(4), 858-862.

Murray, L.J., Abrams, T.J., Long, K.R., Ngai, T.J., Olson, L.M., Hong, W., Keast, P.K., Brassard, J.A., O'Farrell, A.M., Cherrington, J.M., Pryer, N.K., 2003. SU11248 inhibits tumor growth and CSF-1R-dependent osteolysis in an experimental breast cancer bone metastasis model. Clin Exp Metastasis 20(14713109), 757-766.

Neeman, M., Gilad, A.A., Dafni, H., Cohen, B., 2007. Molecular imaging of angiogenesis. J Magn Reson Imaging 25(1), 1-12.

Ng, C.S., Raunig, D.L., Jackson, E.F., Ashton, E.A., Kelcz, F., Kim, K.B., Kurzrock, R., McShane, T.M., 2010. Reproducibility of perfusion parameters in dynamic contrast-enhanced MRI of lung and liver tumors: effect on estimates of patient sample size in clinical trials and on individual patient responses. AJR Am J Roentgenol 194(2), W134-140.

O'Farrell, A.-M., Abrams, T.J., Yuen, H.A., Ngai, T.J., Louie, S.G., Yee, K.W.H., Wong, L.M., Hong, W., Lee, L.B., Town, A., Smolich, B.D., Manning, W.C., Murray, L.J., Heinrich, M.C., Cherrington, J.M., 2003. SU11248 is a novel FLT3 tyrosine kinase inhibitor with potent activity in vitro and in vivo. Blood 101(12531805), 3597-3605.

Papaetis, G.S., Karapanagiotou, L.M., Pandha, H., Syrigos, K.N., 2008. Targeted therapy for advanced renal cell cancer: cytokines and beyond. Curr Pharm Des 14(22), 2229-2251.

Pardee, A.B., 2006. Regulatory molecular biology. Cell Cycle 5(8), 846-852.

Parker, G.J., F.Tanner, S., O.Leach, M., 1996. Pitfalls in the measurement of tissue permeability over short time-scales using multi-compartment models with a low temporal resolution

blood input function. Proceedings of the International Society of Magnetic Resonance Medicine, 1582.

Parkera, G.J.M., Bausterta, I., Tannera, S.F., Leach, M.O., 2000. Improving image quality and T1 measurements using saturation recovery turboFLASH with an approximate K-space normalisation filter. Magn Reson Imaging 18, 11.

Patard, J.J., Rioux-Leclercq, N., Fergelot, P., 2006. Understanding the importance of smart drugs in renal cell carcinoma. Eur Urol 49(4), 633-643.

Perez-Zincer, F., Olencki, T., Budd, G.T., Peereboom, D., Elson, P., Bukowski, R.M., 2002. A phase I trial of weekly gemcitabine and subcutaneous interferon alpha in patients with refractory renal cell carcinoma. Invest New Drugs 20(12211213), 305-310.

Peters, T.M., 2000. Image-guided surgery: from X-rays to virtual reality. Comput Methods Biomech Biomed Engin 4(1), 27-57.

Preda, A., van Vliet, M., Krestin, G.P., Brasch, R.C., van Dijke, C.F., 2006. Magnetic resonance macromolecular agents for monitoring tumor microvessels and angiogenesis inhibition. Invest Radiol 41(3), 325-331.

Raffoul, J.J., Banerjee, S., Singh-Gupta, V., Knoll, Z.E., Fite, A., Zhang, H., Abrams, J., Sarkar, F.H., Hillman, G.G., 2007. Down-regulation of apurinic/apyrimidinic endonuclease 1/redox factor-1 expression by soy isoflavones enhances prostate cancer radiotherapy in vitro and in vivo. Cancer Res 67(17332344), 2141-2149.

Rini, B.I., 2009. Metastatic renal cell carcinoma: many treatment options, one patient. J Clin Oncol 27(19), 3225-3234.

Rini, B.I., Michaelson, M.D., Rosenberg, J.E., Bukowski, R.M., Sosman, J.A., Stadler, W.M., Hutson, T.E., Margolin, K., Harmon, C.S., DePrimo, S.E., Kim, S.T., Chen, I., George,

D.J., 2008. Antitumor activity and biomarker analysis of sunitinib in patients with bevacizumab-refractory metastatic renal cell carcinoma. J Clin Oncol 26(18669461), 3743-3748.

Roberts, C., Issa, B., Stone, A., Jackson, A., Waterton, J.C., Parker, G.J., 2006. Comparative study into the robustness of compartmental modeling and model-free analysis in DCE-MRI studies. J Magn Reson Imaging 23(4), 554-563.

Roberts, C., Issa, B., Stone, A., Jackson, A., Waterton, J.C., Parker, G.J.M., 2006. Comparative Study into the Robustness of Compartmental Modeling and Model-Free Analysis in DCE-MRI Studies. JOURNAL OF MAGNETIC RESONANCE IMAGING 23, 10.

Roberts, T.P.L., 1997. Physiologic Measurements by ContrastlEnhanced MR Imaging: Expectations and Limitations. JOURNAL OF MAGNETIC RESONANCE IMAGING 7, 82.

Sawhney, R., Kabbinavar, F., 2008. Angiogenesis and angiogenic inhibitors in renal cell carcinoma. Curr Urol Rep 9(1), 26-33.

Schmidinger, M., Zielinski, C.C., Vogl, U.M., Bojic, A., Bojic, M., Schukro, C., Ruhsam, M., Hejna, M., Schmidinger, H., 2008. Cardiac toxicity of sunitinib and sorafenib in patients with metastatic renal cell carcinoma. J Clin Oncol 26(18838713), 5204-5212.

Sohal, J., Phan, V.T., Chan, P.V., Davis, E.M., Patel, B., Kelly, L.M., Abrams, T.J., O'Farrell, A.M., Gilliland, D.G., Le Beau, M.M., Kogan, S.C., 2003. A model of APL with FLT3 mutation is responsive to retinoic acid and a receptor tyrosine kinase inhibitor, SU11657. Blood 101(12515727), 3188-3197.

Tannir, N.M., Thall, P.F., Ng, C.S., Wang, X., Wooten, L., Siefker-Radtke, A., Mathew, P., Pagliaro, L., Wood, C., Jonasch, E., 2008. A phase II trial of gemcitabine plus

capecitabine for metastatic renal cell cancer previously treated with immunotherapy and targeted agents. J Urol 180(18635226), 867-872.

Telli, M.L., Witteles, R.M., Fisher, G.A., Srinivas, S., 2008. Cardiotoxicity associated with the cancer therapeutic agent sunitinib malate. Ann Oncol 19(18436521), 1613-1618.

Tobias, J.S., Whitehouse, J.M., 1976. Achievements of cancer chemotherapy. J R Coll Physicians Lond 11(1), 59-74.

Tofts, P.S., 1996. Optimal detection of blood-brain barrier defects with Gd-DTPA MRI—The influences of delayed imaging and optimised repetition time. Magn Reson Imaging 14(4), 8.

Tofts, P.S., Berkowitz, B., Schnall, M.D., 1995. Quantitative analysis of dynamic Gd-DTPA enhancement in breast tumors using a permeability model. Magn Reson Med 33(4), 564-568.

Tofts, P.S., Kermode, A.G., 1991. Measurement of the blood-brain barrier permeability and leakage space using dynamic MR imaging. 1. Fundamental concepts. Magn Reson Med 17(2), 357-367.

Tong, R.T., Boucher, Y., Kozin, S.V., Winkler, F., Hicklin, D.J., Jain, R.K., 2004. Vascular normalization by vascular endothelial growth factor receptor 2 blockade induces a pressure gradient across the vasculature and improves drug penetration in tumors. Cancer Res 64(15172975), 3731-3736.

Udvardy, A., 1996. The role of controlled proteolysis in cell-cycle regulation. Eur J Biochem 240(2), 307-313.

Van Cann, E.M., Rijpkema, M., Heerschap, A., van der Bilt, A., Koole, R., Stoelinga, P.J., 2008. Quantitative dynamic contrast-enhanced MRI for the assessment of mandibular invasion by squamous cell carcinoma. Oral Oncol 44(12), 1147-1154.

van Spronsen, D.J., Mulders, P.F., De Mulder, P.H., 2005. Novel treatments for metastatic renal cell carcinoma. Crit Rev Oncol Hematol 55(3), 177-191.

Weiss, C.R., Nour, S.G., Lewin, J.S., 2008. MR-Guided Biopsy: A Review of Current Techniques and Applications. Journal of Magnetic Resonance Imaging 27, 311-325.

Whang, Y.E., Godley, P.A., 2003. Renal cell carcinoma. Curr Opin Oncol 15(3), 213-216.

Wildiers, H., Guetens, G., De Boeck, G., Verbeken, E., Landuyt, B., Landuyt, W., de Bruijn, E.A., van Oosterom, A.T., 2003. Effect of antivascular endothelial growth factor treatment on the intratumoral uptake of CPT-11. Br J Cancer 88(12799646), 1979-1986.

Wolff, J.E., Gnekow, A.K., Kortmann, R.D., Pietsch, T., Urban, C., Graf, N., Kuhl, J., 2002. Preradiation chemotherapy for pediatric patients with high-grade glioma. Cancer 94(1), 264-271.

Xu, L., Tong, R., Cochran, D.M., Jain, R.K., 2005. Blocking platelet-derived growth factor-D/platelet-derived growth factor receptor beta signaling inhibits human renal cell carcinoma progression in an orthotopic mouse model. Cancer Res 65(15994946), 5711-5719.

Yabuuchi, H., Matsuo, Y., Okafuji, T., Kamitani, T., Soeda, H., Setoguchi, T., Sakai, S., Hatakenaka, M., Kubo, M., Sadanaga, N., Yamamoto, H., Honda, H., 2008. Enhanced mass on contrast-enhanced breast MR imaging: Lesion characterization using combination of dynamic contrast-enhanced and diffusion-weighted MR images. J Magn Reson Imaging 28(5), 1157-1165.

Yang, C., Karczmar, G.S., Medved, M., Stadler, W.M., 2004. Estimating the arterial input function using two reference tissues in dynamic contrast-enhanced MRI studies: fundamental concepts and simulations. Magn Reson Med 52(5), 1110-1117.

Yankeelov, T.E., Gore, J.C., 2009. Dynamic Contrast Enhanced Magnetic Resonance Imaging in Oncology: Theory, Data Acquisition, Analysis, and Examples. Curr Med Imaging Rev 3(2), 91-107.

Yankeelov, T.E., Lepage, M., Chakravarthy, A., Broome, E.E., Niermann, K.J., Kelley, M.C., Meszoely, I., Mayer, I.A., Herman, C.R., McManus, K., Price, R.R., Gore, J.C., 2007. Integration of quantitative DCE-MRI and ADC mapping to monitor treatment response in human breast cancer: initial results. Magn Reson Imaging 25(17222711), 1-13.

Zeidman, I., 1957. Metastasis: a review of recent advances. Cancer Res 17(3), 157-162.

Zeidman, I., Buss, J.M., 1952. Transpulmonary passage of tumor cell emboli. Cancer Res 12(10), 731-733.

Zhu, X.P., Li, K.L., Kamaly-Asl, I.D., Checkley, D.R., Tessier, J.J.L., Waterton, J.C., Jackson, A., 2000. Quantification of Endothelial Permeability, Leakage Space, and Blood Volume in Brain Tumors Using Combined T1 and T2* Contrast-Enhanced Dynamic MR Imaging. JOURNAL OF MAGNETIC RESONANCE IMAGING 11, 11.

Zogakis, T.G., Libutti, S.K., 2001. General aspects of anti-angiogenesis and cancer therapy. Expert opinion on biological therapy 1(2), 23.

ABSTRACT

QUANTIFICATION OF VASCULAR PARAMETRIC INDICES USING DYNAMIC CONTRAST-ENHANCED MAGNETIC RESONANCE IMAGING

by

AREEN AL-BASHIR

December 2010

Advisor: Dr. E. Mark Haacke

Major: Biomedical Engineering

Degree: Doctor of Philosophy

Dynamic contrast-enhanced magnetic resonance imaging (DCE-MRI) is a non-invasive method used to evaluate the biological activity in early clinical trials of novel drugs targeting the tumor vasculature using gadolinium-DTPA (Gd) as a contrast agent. However, it has some limitations, such as reproducibility, data acquisition times, the presence of noise, extracting contrast concentration, estimating T1 relaxation and estimating pharmacokinetic parameters.

In this work, a new approach to used fixed $T1(0)$ which provides more reproducible DCE results has been introduced. Using this new algorithm to quantify the vascular changes in DCE-MRI, a pre-clinical renal cell carcinoma (RCC) tumor model was used to demonstrate the ability of DCE-MRI to quantify the vascular changes induced by various doses of sunitinib in tumor-bearing kidneys and normal contralateral kidneys. Usually, only the first minute of data are used for processing to calculate the initial area under the curve (IAUC) and/or the median

145

value of cumulative initial area under the curve (CIAUC) in order to monitor changes between pre and post drug treatment. However, in this work, the first two minutes was used to include the effect of the washout process of the kidneys. Moreover, DCE-MRI was used to investigate the vascular changes induced by pre-treatment with sunitinib in KCL-18 kidney tumors to schedule the initiation of chemotherapy. DCE results were confirmed with the histologic studies.

In this thesis, several new measures of vascular properties have been introduced, including: the fraction of active pixels (FAP); contrast agent uptake to the peak (AUCtp); time to peak concentration (TTP); washout slope (Nslope); as well as full width half maximum (FWHM) of IAUC. The results from the pre-clinical RCC tumor model demonstrate that DCE parametric maps have the potential to assess the effect of antiangiogenic drugs on blood flow and physiological vascular changes in tumors as well as normal tissues. These new parametric maps provided further guidance as to what could be considered normal versus abnormal tissue response to antiangiogenic therapy. The results of this research should lead to a clear improvement in the ability of DCE-MRI as a quantitative method to evaluate tumor vasculature and other hemodynamic properties.

AUTOBIOGRAPHICAL STATEMENT

AREEN AL.BASHIR

The MRI Institute for Biomedical Research   Emil: **areen@wayne.edu**
440 East Ferry Street, Detroit, MI 48202   Tel: (313)-745-1388(office); (313)-408-4457(cell)

Education

- **Wayne State University, Detroit, MI, USA.**   PhD (Winter 2007- Present)
Major: Biomedical Engineering GPA: 3.70   <u>Expected day of graduation: Fall 2010</u>
- **Wayne State University, Detroit, MI, USA.**   MS (Fall 2005 – Fall 2006)
Major: Biomedical Engineering   GPA: 3.79
- **Jordan University of Science and Technology, Jordan.**   BS(Nov. 1998 – Jun. 2003)
Major: Biomedical Engineering   GPA: 82.5/100; Ranked on the top 1% of the graduates.

Publications

- New algorithm for quantifying vascular changes in dynamic contrast-enhanced MRI independent of absolute T_1 values. E. Mark Haacke, Cristina L. Filleti, Ramtilak Gattu, Carlo Ciulla, **Areen Al-Bashir** and others. MRM, 2007; 58: 463-472.

- Dynamic Contrast Enhanced Magnetic Resonance Imaging of Vascular Changes Induced by Sunitib, an Anti-Angiogentic Drug, in Murine Kidney Tumors. Gilda G. Hillman, Vinita Singh-Gupta, Hao Zhang, **Areen K. Al-Bashir**, and others. Neoplasia, 2009; 11(9): 910–920.

- DCE-MR Imaging of Sunitinib-Induced Vascular Changes to Schedule Chemotherapy in Renal Cell Carcinoma Xenograft Tumors. Gilda Hillman, Vinita Singh-Gupta, **Areen Al-Bashir**, Hao Zhang, Christopher Yunker, Judith Abrams and Mark E. Haacke. Transl onclol, 2010, in press.

- New DCE-MRI Parametric Maps to Quantify the Vascular Changes Induced by Sunitinib Treatment in Renal Carcinoma Tumors. **Areen K. Al-Bashir**, Gilda G. Hillman, Meng Li, and E. Mark Haacke Under progress.

- Gilda Hillman, Vinita Singh-Gupta, **Areen Al-Bashir**, Hao Zhang, Christopher Yunker, Judith Abrams and Mark E. Haacke. Assessment of vascular changes by DCE-MRI to study the effect of radiotherapy and soy in renal cell carcinoma. Under progress.

Summary of Work Experience

- **Jan. 2006- current: Harper University Hospital, Detroit, Michigan, USA:** Graduate Research Assistance, part time.

- **Oct. 2003- Dec. 2004 King Abed Allah Hospital, Irbid, Jordan:** Practical Training maintaining all Medical Equipment and Devices.